CHARACTERIZATION OF AN INDUCTIVELY COUPLED PLASMA PRODUCED IN ARGON AT 13.56 MHz

LIM AI NUAN

FACULTY OF SCIENCE
UNIVERSITY OF MALAYA
KUALA LUMPUR

2010

CHARACTERIZATION OF AN INDUCTIVELY COUPLED PLASMA PRODUCED IN ARGON AT 13.56 MHz

LIM AI NUAN

DISSERTATION SUBMITTED IN FULFILMENT OF THE REQUIREMENTS FOR THE DEGREE OF MASTER OF SCIENCE

FACULTY OF SCIENCE
UNIVERSITY OF MALAYA
KUALA LUMPUR

2010

ABSTRACT

The electrical and plasma characteristics of radio frequency (13.56 MHz) inductively coupled argon plasma (RF ICP) were studied in this project. On the electrical breakdown properties, the breakdown voltage has a general appearance of Paschen's curve and the minimum is achieved at 0.1 mbar. After ignition, two modes of discharge exist, namely, the *E* mode at low RF power and *H* mode at high RF power. Mode transition that occurs is accompanied by abrupt changes in both electrical and plasma characteristics. Hysteresis is observed in the mode transitions and has a minimum at 0.1 mbar. The resistance reflected into the electrical circuit due to *H* mode plasma is 9.8 times higher when compared to *E* mode (R_p= 0.10±0.01) Ω. Therefore, the impedance matching scheme used is most efficient at *E* mode where the antenna coil resistance R_a is (1.12±0.01) Ω. R_a doubles in the *H* mode. However, the transfer of power is more efficient in the *H* mode. This efficiency is reflected in the much higher electron density of n_e = (3.6–12.2)×10^{17} m^{-3} measured in the *H* mode at 0.10±0.1 mbar. Consequently, the increased electron collisions tend to lower the electron temperature T_e in the *H* mode (1.7–2.0 eV) as compared to that in *E* mode (T_e = 2.3-2.8 eV). The measured electron energy distribution function *EEDF* in *H* mode is inclined towards Maxwellian-type especially at 200 W. From the radial distribution of plasma properties, it is deduced that *E* mode discharge is relatively more uniform and diffuse.

ABSTRAK

Ciri-ciri plasma dan elektrik bagi plasma argon gandingan secara induktif dalam frekuensi radio (13.56 MHz) dikaji dalam projek ini. Berkaitan dengan ciri-ciri runtuh elektrik, voltan runtuh mempunyai bentuk am lengkung Paschen dan minima tercapai pada 0.1 mbar. Setelah bernyala, terdapat dua mod nyahcas yang wujud, yakni, mod *E* pada kuasa RF rendah dan mod *H* pada kuasa RF tinggi. Peralihan mod berlaku bersama dengan perubahan mendadak dalam ciri-ciri plasma dan elektrik. Histeresis diperhatikan dalam peralihan mod dan ia mempunyai minimum pada 0.1 mbar. Rintangan terpantul ke dalam litar elektrik kerana plasma mod *H* adalah 9.8 kali lebih tinggi apabila dibandingkan dengan mod *E* (R_p= 0.10±0.01) Ω. Maka skema padanan impedans yang digunakan adalah paling efisien pada mod *E* di mana rintangan gegelun antena R_a ialah (1.12±0.01) Ω. R_a berganda dalam mod *H*. Bagaimanapun begitu, pemindahan kuasa adalah lebih efisien dalam mod *H*. Kecekapan ini dicerminkan dalam nilai ketumpatan elektron n_e = (3.6–12.2)×10^{17} m^{-3} dalam mod *H* pada 0.10±0.1 mbar yang jauh lebih tinggi. Sebagai akibatnya, peningkatan perlanggaran elektron boleh menurunkan suhu elektron T_e dalam mod *H* (T_e=1.7–2.0 eV) jika dibandingkan dengan mod *E* (T_e= 2.3-2.8 eV). Fungsi Taburan Tenaga Elektron *EEDF* yang diukur dalam mod *H* pula bercenderongkan jenis-Maxwell terutamanya pada 200 W. Disimpulkan dari taburan jejarian bagi ciri-ciri plasma bahawa secara relatifnya nyahcas mod *E* adalah lebih seragam dan kabur.

ACKNOWLEDGEMENT

I wish to convey my innermost gratitude to my supervisor, Associate Professor Dr. Chin Oi Hoong, for her patient guidance and invaluable assistance throughout the duration of this project.

I also appreciate the support awarded by University of Malaya through the Postgraduate Scholarship (SBK) and Research Funding F-Vote No. F0207/2005B, and the Ministry of Science, Technology and Innovation through its IRPA RMK8 Grant No. 09-02-03-0223-EA223.

A special “thank you” is accorded to Mr. Jasbir Singh for his technical support in contributing to the success of this project.

Last but not least, I am very grateful to everyone in the Low Temperature Plasma Laboratory for their friendship and advice.

CONTENTS

LIST OF FIGURES

LIST OF TABLES

LIST OF SYMBOLS

V_B, U_b	=	breakdown voltage
U_{st}	=	sustaining voltage after breakdown
p	=	gas pressure
d	=	gap separation or sheath thickness as specified in text
L	=	electrode spacing / gap length
$U_{bd(DC)}$	=	DC breakdown potential
γ	=	secondary Townsend's coefficient
Λ	=	vacuum wavelength of the RF field
B_{bd}	=	breakdown RF magnetic field
R	=	radius of the chamber
β	=	probability of recombination of ions in the volume
ξ	=	power transfer efficiency
u_B	=	Bohm velocity
P_{dis}	=	power dissipated in the plasma
P_{tr}	=	transferred power
P_{net}	=	net RF input power
P_{in}	=	RF input power
P_{rfl}	=	RF reflected power
P_0	=	applied RF power without ignition of plasma
I_{rf}, I_{rf0}	=	planar coil current with and without discharge
I_{coil}, V_{coil}	=	planar coil rms current and voltage
I_{rms}, V_{rms}	=	planar coil rms current and voltage during for mode transition
I_{pc}, V_{pc}	=	primary coil rms current and voltage
I_{sc}, V_{sc}	=	secondary coil rms current and voltage
R_a	=	planar coil resistance
R_{pc},R_{sc}	=	primary coil and secondary coil resistance
n_e	=	electron density
r	=	radial distance from central axis of chamber
z	=	vertical distance from the quartz window
T_e	=	electron temperature
T_{eff}	=	effective electron temperature deduced from *EEDF*
T_i	=	average temperature of ion distribution

V_s, V_f	=	plasma potential, floating potential
V_p, I_p	=	probe potential, probe current
I_{es}, I_{is}	=	electron and ion saturation current
I_e, I_i	=	electron and ion current to the probe
n_0	=	unperturbed electron density
$\bar{v}_e$	=	electron mean velocity
A	=	probe surface area
m_i, m_e	=	mass of ion (Ar^+), mass of electron
λ_D	=	Debye length
λ_e	=	electron mean free path
ε_T	=	total energy lost per ion lost in the system
ε	=	electron energy in eV
$F_e(\varepsilon)$	=	*EEDF*
Z_p, Z_s	=	impedance of primary circuit, impedance of secondary circuit
a	=	turns ratio of step-down transformer
L_{cp},L_{c0}	=	inductance of planar coil with and without the presence of plasma
R_t	=	total resistance in the RF circuit
R_0	=	RF circuit resistance without plasma
R_p	=	resistance reflected into the RF circuit in the presence of plasma
R_g	=	internal resistance of RF source
X_t	=	total reactance in RF circuit
r_p, l_p	=	radius and length of Langmuir probe tip
σ	=	collisional cross section
R_I	=	current sensing resistance in the probe circuit
R_C	=	probe circuit resistance
R_O	=	probe driver output resistance
R_W	=	resistance of probe wire
R_{ct}	=	contact resistance in probe circuit
R_{rf}	=	resistance of RF filter in probe circuit
R_{Sw}	=	sheath resistance near chamber wall in probe circuit
R_{sf}	=	surface resistance of discharge chamber in probe circuit
E_{ind}	=	induced electric field due to oscillating magnetic field
EEDF	=	electron energy distribution function
EEPF	=	electron energy probability function

CHAPTER 1 GENERAL INTRODUCTION

1.1 INDUSTRIAL INTEREST IN PLASMA

The word "PLASMA" was coined by Irving Langmuir, an American chemist and physicist, in 1927 to describe an ionized gas. Plasmas are typically conductive and respond to external electric and magnetic fields. They can be efficient sources of radiation and charged particles of various species, existing as partially ionized low-temperature plasmas up to the highly ionized, high energy density plasmas. There are hundreds of subject areas in plasma science and technology and nearly as many applications [1].

The low-temperature plasmas have been used extensively in many industrial applications [2,3]. The wide use of low temperature plasma in material processing is due to it being a source of copious energetic particles that can be used for sputtering purposes and to activate the active species required to enhance the deposition and etching processes [4]. These plasma processes are environmentally friendly, making it one of the most promising technologies of the 21st century.

Conventional plasma-processing tools are essentially based on parallel-plate capacitively coupled RF discharges, in which a voltage is applied to electrodes to break down a gas and sustain the generated discharges. Plasmas generated in this method are usually only partially ionized and have high neutral gas pressures. Because higher ion fluxes toward substrates are generally more desirable in plasma processing to obtain smaller size structures to below 300 nm [3], high-plasma-density processing tools with

lower gas pressures are replacing the conventional plasma tools. Several different methods can be used to generate high-density plasmas for semiconductor manufacturing. Examples are the inductively coupled plasma (ICP) whereby oscillating radio frequency (RF) electric fields are used to generate and sustain high-density plasma without using steady-state magnetic fields [5,6], and the helicon plasma in which steady-state magnetic fields are used and the helicon waves are induced along the magnetic field lines [7,8]. Additionally, electron cyclotron resonance (ECR) [9] and the neutral-loop discharge (NLD) [10] in which the plasma is generated by RF fields along a closed magnetic neutral line can be used to generate high-density plasmas.

For most etching or deposition processes, it is highly desirable to control the plasma production and the substrate bias separately. This can be achieved in plasma sources like capacitively and inductively coupled RF glow discharges (usually at 13.56 MHz) as well as the ECR microwave plasma (usually at 2.45 GHz) which can produce relatively homogeneous heating zones [11]. These plasma sources are operated at low pressures of less than 1 mbar. Frequency of 13.56 MHz has gained most interest in the studies on plasma diagnostics because of the wide-spread use of this frequency in plasma processing, and in part it is the allowed frequency to radiate unlimited power by international communications authorities. In addition, there is much interest in the mechanisms which generates and sustains the RF glow discharge both for intrinsic reasons and because of their technological applications.

1.2 INDUCTIVELY COUPLED PLASMA (ICP)

In comparison to the capacitively coupled RF plasma, inductively coupled plasma offers the possibility of independent control of the plasma's charged particle

density and the voltage across the sheath in front of a potential wafer. In addition, the ICP source can produce higher plasma density of the order of 10^{12} cm^{-3} compared to that of capacitively coupled plasma at $10^{9} – 10^{10}$ cm^{-3}.

The ICP is excited by the induced RF electric field without driving an electric displacement current through the sheath in front of a wafer. The conditions are similar to that of a sheath in DC plasma, which is characterized by sheath voltages of the order of the mean energy of the electrons [12]. The advantage of the ICP lies in the simplicity of its generation, that is, no external magnetic fields are required for the plasma generation. These ICP sources are electrodeless plasma excitation design in which there is no contamination of the electrode in the plasma during material processing. There are generally two types of ICP source configurations: helical (solenoid) and spiral (planar) type [6]. The planar configuration has attracted a lot of interest due to its ability to produce uniform disk-like plasma that can be scaled up easily.

The ICP system has a simple design concept and it utilizes simple equipment. When RF power is supplied to a resonant circuit, a large RF current circulating in the coil generates a RF magnetic field within the evacuated chamber, which in turn, induces a circulating RF electron current in the plasma once the plasma is generated. This is basically transformer action, with the plasma itself acting as a single turn secondary coil.

1.3 LANGMUIR PROBE CHARACTERIZATION

One of the fundamental techniques - the first one, in fact - for measuring the properties of plasma is the use of electrostatic probe developed by Langmuir in 1924 and is called the Langmuir probe method. Basically, it is made up of a small metallic

electrode, usually a wire, immersed into the plasma. The probe is connected across a potential source to a reference electrode, which in many cases serves simultaneously as the cathode or the anode of a discharge tube. The current flowing to the probe is measured as a function of the applied voltage. The resulting current-voltage relationship is called the *I-V* or probe characteristics from which the plasma parameters can be determined [13]. The simplicity of apparatus needed for the Langmuir probe method gives it the advantage over other methods of plasma diagnostics.

Localized fundamental characteristics of plasma, namely the ion number density, electron number density, electron temperature, electron energy distribution function (*EEDF*), floating potential and plasma potential can be deduced from the probe characteristics. This is unlike spectroscopy and microwave propagation diagnostic techniques which are only capable of giving values of plasma parameters averaged over a relatively large volume. Langmuir probes are routinely used to determine the plasma parameters in diverse areas such as low pressure plasmas for materials processing, the design of ion sources and new plasma chambers and edge plasma in fusion devices. This information is used to characterize individual system and processes and also to design new systems.

However, there are some pitfalls that one should be careful about. The appropriate probe theory to be used to interpret the results must be chosen carefully based on its conditions such as probe dimension, presence of magnetic field and mean free path of the species in the plasma. In the case of RF plasma, it is well known that the RF drive frequency and its harmonics can result in distorted probe characteristics [14]. Thus, proper and correct filtering of these RF potential disturbances must be done.

1.4 OBJECTIVES OF THE PROJECT

The main objective of this project is to study the generation and sustaining of a 13.56 MHz RF inductively coupled discharge in argon. Though this ICP system has been previously used for nitriding of titanium [14a], characterization of the plasma under the two modes of operation via RF compensated Langmuir probe have not be carried out yet. Hence, this work is focused on the electrical performance of the ICP system and the characteristics of the RF ICP in argon operated in the *E* mode and *H* mode.

The electrical performance of the RF ICP system is studied in terms of the electrical properties of the coupling network, breakdown properties of the discharge, *E* mode and *H* mode discharges and their mode transition, and power coupling efficiency.

Parametric study of the characteristics of the RF ICP operated in argon is carried out via an RF compensated Langmuir probe capable of filtering off the effects up to the second harmonics of the drive frequency. The RF ICP is characterized by the electron temperature, electron density, plasma potential, and Electron Energy Distribution Function (*EEDF*) which are deduced from the measured *I-V* curve collected by the Langmuir probe. These characteristics are measured for various input RF power and the two modes of discharge operation as well as their radial distribution.

1.5 OUTLINE OF DISSERTATION

This dissertation consists of six chapters. Industrial interest in plasmas, ICP and Langmuir probe characterization are introduced in Chapter 1 leading to the objectives of the present work as well as the outline of this dissertation. Chapter 2 briefly reviews

ICPs and their characteristics and relevant diagnostics techniques. This is followed by a description of the design of the experimental setup and diagnostic techniques applied as well as interpretation of data in Chapter 3. In Chapter 4, the results on the RF breakdown characteristics and electrical properties of the RF ICP system are analyzed and discussed. The characteristics of plasma diagnosed by the Langmuir probe under various operating conditions are presented in Chapter 5. Finally, the conclusion and suggestion for further work are included in Chapter 6.

CHAPTER 2 LITERATURE REVIEW AND BACKGROUND THEORIES

2.1 RADIO FREQUENCY INDUCTIVELY COUPLED PLASMA (RF ICP)

Radio frequency inductively coupled plasma (RF ICP) sources, also known as radio frequency inductive (RFI) and transformer coupled plasma (TCP) sources, draw tremendous interests in many industrial applications. For instance, low pressure inductively coupled plasmas (ICPs) are suitable in surface modification, plasma sputtering and etching while high pressure ICPs are used in spectra-chemical analysis, plasma-aided chemical synthesis and plasma deposition [6]. The low pressure ICPs have many important industrial applications, mainly because they can provide a high density electrodeless plasma source with low ion energy and low power loss in the sheaths as compared to that of the capacitively coupled RF plasma.

RF ICP source is capable of producing steady-state plasmas, with number of electron densities in excess of $10^{12}\,\mathrm{cm}^{-3}$. At low RF power input, the plasma in an ICP system is characterized by a dim light emission from the plasma and a low electron number density. This discharge is referred as an *E* mode discharge. When the RF power input reaches a certain critical value, there is sudden rise both in the plasma luminosity and in electron number density, hence signaling a mode transition, from the *E* mode to the *H* mode.

Experimental investigations of RF ICPs have included studies on the electrical characteristics of the ICP system [15-18] inclusive of modes of discharges as well as mode transition [19-22], and the plasma characteristics [12,23,24]. There is also much work performed on the modeling of RF ICPs and comparison made with experimental data [11,25-27].

2.2 ELECTRICAL CHARACTERISTICS

Measurements of the electrical properties of inductively coupled plasma (ICP) include a wide range of operating parameters such as RF frequency and power, gas pressure and type of gas, and impedance matching network. Measurements of electrical properties include voltage, current and power on the induction coil, the RF breakdown characteristics, the *E* mode and *H* mode discharges and their mode transitions, and the power transfer efficiency.

2.2.1 RF BREAKDOWN CHARACTERISTICS

A discharge is often ignited by applying an electric field to produced sufficient ionization in a neutral gas. The ionization processes in a steady field differ noticeably from those in an alternating field especially when the applied frequency is more than 10 kHz. If the frequency is increased until the ions as well as the highly mobile electrons are not able to reach the respective electrodes, breakdown can occur even when the electrodes are placed externally, and it is known as electrodeless discharge. Here, the loss of electrons is mainly through diffusion and the breakdown mechanism is diffusion-controlled [28,29]. At the initial phase of the RF breakdown during the low

power input, a streamer-like electrostatic discharge is developed by the strong electrostatic field due mainly to the electric field component resulting from the large potential difference across the induction coil at electrical resonance. This discharge immediately after ignition experiences dominantly capacitive coupling.

Breakdown voltage, V_B, over a gap is usually given as a function of the pressure p and the gap separation d. In a uniform electric field, it can be described by Paschen law which shows no dependency on frequency, but is dependent on the gas. The Paschen law gives the DC breakdown potential $U_{bd(DC)}$ as:

$$U_{bd(DC)} = \frac{B_0 pL}{\ln[pLA_0 / \ln\{(1+\gamma)/\gamma\}]}, \tag{2.1}$$

where p is the gas pressure, L the electrode spacing, A_0 and B_0 constants dependent on gas, and γ is the secondary Townsend's coefficient. The Paschen curve is typically valid for a capacitively coupled discharge with one of the electrode connected to a high voltage and the other grounded. *Lisovskiy and Yegorenkov* [30] reported RF (13.56 MHz) breakdown in air, argon and hydrogen in pressure ranging from 10^{-2} to 20 Torr with internal planar circular electrodes of diameter and inter-electrode gaps of 6.5 to 70 mm. Here the electron loss is mainly by diffusion to the walls of the vacuum vessel. Other means of electron loss include oscillating motion of electron cloud in the RF field and recombination. Breakdown in combined RF and DC electric fields in capacitively coupled plasma was studied by *Lisovskiy and Yegorenkov* [31], and the Kihara equation [32] was used for RF gas breakdown and is given as:

$$\exp\left(\frac{B_0 p}{2E}\right) = A_1 pL\left(1 - \frac{E/B_0 p}{C_2 L/\Lambda}\right), \tag{2.2}$$

where E is the r.m.s. value of the RF electric field, p the gas pressure, L the gap length, Λ the vacuum wavelength of the RF field, A_1, B_0 and C_2 are the molecular gas constants. In argon gas, $A_1 = 9$ (cm·Torr)$^{-1}$, $B_0 = 184$ V/cm·Torr and $C_2 = 7149$.

However, in the case of inductively coupled plasma with external electrode, *Burm* [33] adapted the Paschen's relation for time-dependent magnetic field. A simple single turn induction coil that encircles the plasma chamber was assumed and the breakdown RF magnetic field B_{bd} (and, therefore, an induced electric field given as $E = \omega BR$) to be dependent on applied angular frequency $\omega = 2\pi f$, gas pressure p and its nature, radius R of the chamber (influence of wall material was ignored). The relation was given as [33]:

$$B_{bd} = \frac{C_B p}{\omega R[\ln(C_A p \pi R) - \ln\{\ln(1+\frac{1}{\beta})\}]}, \qquad (2.3)$$

where C_A and C_B are gas-dependent constants, and β is probability of recombination of ions in the volume (and at the wall). It was shown that higher breakdown magnetic field is required for smaller chamber and lower angular frequency. There exists a minimum pressure which is strongly dependent on the geometry of the chamber (larger radius makes possible ignition at lower pressure) where it is impossible to ignite the plasma. The breakdown curve has shape similar to that given by Paschen's law for static electric fields.

2.2.2 *E* MODE AND *H* MODE DISCHARGES

After ignition, at the low RF power, low-density plasma with dim light emission is usually observed. At this stage, the electrostatic field is larger than the induced

electrical field due to the potential difference of the individual turns of the induction coil. This mode is customarily referred to as *E* mode or alternatively known as capacitively coupled RF power.

With further increase of the RF powers which increases the induction coil current, a sudden jump both in the number of electron density and in the light emission occurs, indicating the beginning of a phase of the inductive RF discharge which is known as the *H* mode. This is accompanied by rapid increase of the coil loading resistance and decrease of the effective coil inductance [18]. The *H* mode discharge is sustained by the induced azimuthal RF electrical field which is produced by the oscillating magnetic field.

The sudden transition between the *E* mode and the *H* mode is usually accompanied by an enormous rise of the electron density of about one or more orders of magnitude and also visually, the plasma glow was seen to be much brighter and enclosed the entire volume of the chamber. By reducing the RF power, the inverse *H* mode to *E* mode transition is observed. These mode transitions exhibit a behaviour which is suggestive of hysteresis in the sense that the induction coil current at the *E* to *H* mode transition is not the same as the induction coil current at the *H* to *E* mode. It may also be due to the intrinsic power loss, primarily in the matching system. *Kortshagen et al.* [19], S*uzuki et al.* [34] and *Daltrini et al.* [35] have observed experimentally the properties of the *E* to *H* mode transition based on light emission and discharge behaviour, hysteresis resulting from the *E* to *H* mode transition and the inverse *H* to *E* mode transition.

2.2.3 POWER TRANSFER EFFICIENCY

The power transfer efficiency of inductively coupled plasma is determined by measurement of the power dissipated in the matching network and the inductive coupler. The transfer efficiency is the highest when the plasma-to-inductor distance is the least since the increased mutual inductance reduces the induction coil current and hence, ohmic heating of the circuit elements losses. The power transfer efficiency, ξ which is the ratio of the transferred power P_{tr} to the net RF input power into matching circuit P_{net}, can be determined using the following expression [34]:

$$\xi = \frac{P_{tr}}{P_{net}} = \frac{P_{net} - R_a I_{rf}^2}{P_{net}} = 1 - \frac{R_a I_{rf}^2}{P_{net}}, \qquad (2.4a)$$

where $P_{net} = P_{in} - P_{rfl}$, P_{in} is the RF input power and P_{rfl} is the RF reflected power with an ignited discharge. The second term represents the power loss term at the coil with R_a being the coil resistance, and I_{rf} the coil current measured by the current probe. R_a is determined from the following expression when the discharge is not ignited:

$$P_0 = R_a I_{rf0}^2, \qquad (2.4b)$$

where P_0 is the applied RF power, and I_{rf0} is the coil current with no discharge. *Suzuki et al.* [34] reported the dependence of electron density on the power transfer efficiency. In the low-density region (*E* mode), ξ was shown to decrease with increasing of electron density. In the high-density region (*H* mode), however, ξ increases with the electron density.

2.3 PLASMA CHARACTERISTICS

2.3.1 PLASMA CHARACTERISTICS IN INDUCTIVE DISCHARGES

As ICPs are commonly used in low pressure processing discharge, a good deal of characterization of these inductive discharges has been reported usually at $p \leq 0.1$ mbar. *Mahoney et al*. [36] reported electron density, n_e to lie in the range ($10^{10} – 10^{12}$) cm^{-3} in argon planar RF ICP over power range of (100 – 500) W, pressure range of (2 – 100) mTorr or approximately (0.003 – 0.133) mbar, increasing with net RF power as well as pressure. Peak plasma potential and electron density are located on axis ($r = 0$) at $z = 5$ cm from the discharge/quartz window interface or 7 cm from the planar coil, and reduce towards the boundary of discharge. The peak plasma potential ranges from 14.4 V at 100 mTorr up to 18.1 V at 10 mTorr, and corresponding peak electron densities are respectively 55×10^{10} cm^{-3} and 19×10^{10} cm^{-3}. However, average electron energy peaks off-axis at $r = 6$ cm near the quartz window where the strongest induced RF fields and currents are expected to occur and ranges from 3.1 eV at 100 mTorr up to 4.8 eV at 10 mTorr.

Similar linear increase of ion density (within range of 10^{11} to 10^{12} cm^{-3}) with RF power at fixed pressure and with pressure at fixed RF power was also observed by *Hopwood et al*. [23] for argon pressures (0.3 – 30) mTorr or (0.0004 – 0.04) mbar and RF power (100 – 1200) W. Electron temperature T_e range from 3 to 7 eV and the plasma potential V_s is within the range (15 – 30) V; both decrease with increase in pressure.

The electron energy distribution in low-pressure capacitive RF discharge was measured by *Godyak et al.* [37] for argon pressure between 0.004 mbar and 4 mbar. It

was shown that the *EEDF* favours Druyvesteyn-like at $p > 0.67$ mbar when collisional heating becomes significant. However, at lower pressures where stochastic electron heating dominates, the *EEDF* favours double Maxwellian-like distribution. They demonstrated the transition from Druyvesteyn-like at low discharge current (α-mode) to Maxwellian-like at high current (γ-mode). *Kortshagen et al.* [12] demonstrated the *EEDF* can be represented by a spatially homogeneous function of the total energy of the electrons. Their experimental results agree well with a 1-D model of the axial variation of *EEDF* based on the nonlocal approach.

Most of the plasma characteristics above were measured using the Langmuir probe technique. The technique is simple, and the probe inserted into the plasma has the ability to locally measure the electron density, electron temperature, plasma potential as well as electron energy distribution function over a wide range of experimental conditions. However, the interpretation involves careful choice of appropriate probe theory for the particular plasma environment.

2.3.2 PROBE THEORY AND CHARACTERISTICS [38,39]

In general, a majority of theories for interpreting the probe characteristics depend on the probe geometry and dimension, Debye length and assumes a Maxwellian distribution of both electrons and ions. There are three distinct probe theories, namely, the Orbital-Motion-Limited (OML) which is the original Langmuir theory, Allen-Boyd-Reynolds (ABR) and Bernstein-Rabinowitz-Laframboise (BRL). The OML is restricted to condition where the sheath radius is assumed to be infinite, hence, is applicable for low density where the sheath is much larger than the probe dimension. An absorption radius inside which ions cannot escape being collected by the probe is assumed to be

non-existent, thus, potential variation across the sheath has to be gentle. The ABR includes sheaths, the potential from probe surface is computed for distances up to $r = \infty$ by solving Poisson's equation, and ion temperature is assumed zero from the beginning so that no orbital motions exists and all ions are drawn radially into the probe. To account for both sheath formation and orbital motions, and assuming a Maxwellian ion distribution at temperature T_i, the BRL theory was developed. Choosing the most suitable theory will give more accurate ion contribution fit and, hence, more accurate n_e, T_e, and V_s can be deduced.

Considering a simple idealized plane probe, the current is measured as a function of the applied potential, as shown in Figure 2.1. Let the plasma potential be V_s and the potential applied to probe be V_p. If large positive potential is applied ($V_p > V_s$), the current drawn from the plasma to the probe saturates and no ion current is collected. The electron current is the limited by the random flux of electrons in the sheath around the probe. This sheath shields the plasma from probe and it has thickness of the order of few Debye lengths. The difference in potential between the plasma and the probe is confined within the sheath region. If no magnetic field is applied, and if the mean free path of the electrons is much larger than the thickness of the sheath and of the order of the probe radius, the electron saturation current, I_{es} can be given as [38]:

$$I_{es} = \frac{1}{4} n_0 e \bar{v}_e A = n_0 e A \sqrt{\frac{kT_e}{2\pi m_e}}, \qquad (2.5)$$

where n_0 is the electron density of the unperturbed plasma, e is the electron charge, $\bar{v}_e$ is the electron mean velocity, A is the probe surface area and Maxwellian electrons are assumed with mean velocity $\bar{v} = \sqrt{8kT_e/\pi m}$. The electron density n_e ($\cong n_0$) may be determined from Equation (2.5).

The ion saturation current, I_{is} is obtained at high negative potential ($V_p << V_s$) and is given by an expression similar to the above equation. As the electrons are much more mobile than the ions, the ratio between electron and ion saturation currents would be expected be related to their mass ratio as:

$$\frac{I_{es}}{I_{is}} \approx \sqrt{\frac{m_i}{m_e}} > 200 \text{ (in argon).} \tag{2.6}$$

Assuming that the electrons are in kinetic equilibrium, the electron density, n_e at an arbitrary distance x from the sheath edge towards the plane probe may be expressed from the Boltzmann's relation [40]:

$$n_e(x) = n_0 \exp\left(\frac{eV(x)}{kT_e}\right), \tag{2.7}$$

where $V(x)$ is the potential with respect to the plasma potential and n_0 is the unperturbed plasma density. Thus, at sheath edge where $x = 0$,

$$|V(0)| = \frac{kT_e}{2e}. \tag{2.8}$$

Therefore,

$$n_e = n_0 \exp\left(-\frac{1}{2}\right) \cong 0.61 n_0. \tag{2.9}$$

From the quasi-neutrality condition that holds in the pre-sheath, $n_i(0) \cong n_e(0)$, the ion flux at the sheath edge is expressed through:

$$n_e(0)\bar{v} = 0.61 n_0 \sqrt{\frac{kT_e}{m_e}}, \tag{2.10}$$

and therefore,

$$I_{is} = 0.61 n_0 eA \sqrt{\frac{kT_e}{m_i}}\,. \qquad (2.11)$$

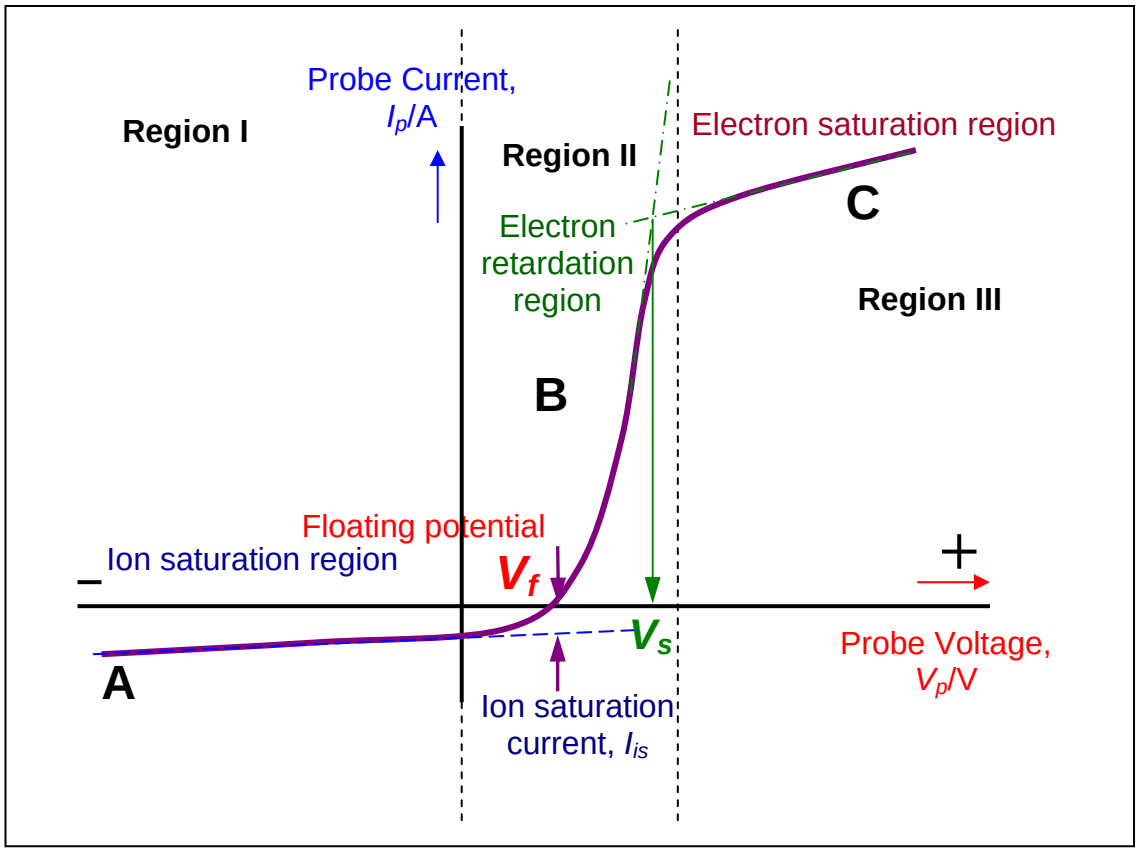

Figure 2.1: Graph of I_p against V_p for an idealized plane probe.

This ion saturation current I_{is} is collected at sufficiently large negative potential relative to the plasma potential (Region I in Figure 2.1). The electron density n_e ($\cong n_0$) may also be determined from Equation (2.11).

However, in typical of ICPs (10^{10} – 10^{12} cm^{-3}), the ion saturation current does not behave according to OML approach. The plasma density is then calculated from the expression [39] reminiscent of Child-Langmuir law:

$$n_0 = \frac{I_{i(\text{at } V_f)}}{2\pi(r_p + d)eL\alpha_0\sqrt{kT_e/m_i}}, \tag{2.12}$$

where r_p is the radius and L is the length of the cylindrical probe, $\alpha_0 \cong 0.61$ is a constant in the consideration of Bohm velocity that can be dependent on the ratio of probe radius and Debye length ($\xi = r_p / \lambda_D$). The sheath thickness d is approximated by [39]:

$$d \approx 1.0\eta_f^{3/4}\lambda_D, \tag{2.13}$$

where $\eta_f = |eV_f/kT_e|$. Densities determined through Equation (2.12) above showed good agreement with other independent measurement method (microwave interferometry) down to 2.7×10^{-3} mbar.

In the electron retardation region of Figure 2.1, the probe current rises exponentially with applied potential to the probe V_p for the Maxwellian electrons assumed. The electron current collected can be expressed by

$$I_e = \frac{1}{4}n_e(x)e\bar{v}_e A. \tag{2.14}$$

From Equations (2.5) and (2.7), Equation (2.14) can be rewritten as

$$I_e = I_{es}\exp\left(\frac{eV}{kT_e}\right), \tag{2.15}$$

and the total probe current I_p includes ion current I_i. The electron temperature can be determined from the slope of a semi-logarithmic plot of I_e against V_p in this retardation region.

The plasma potential V_s may be determined by the abscissa value of the intersection of the extrapolated electron retardation and saturation regions as shown in Figure 2.1. However, the electron saturation current may not be distinct due to sheath expansion, collisions and presence of magnetic fields. It would be easier then to determine the plasma potential at the peak of the first derivative of the electron current with respect to the probe voltage, $(dI_e/dV_p)_{\max}$, or when the second derivative is zero, $d^2I_e/dV_p^2 = 0$. Or it may be determined from the more easily measured floating potential V_f, of the probe (corresponding to zero current) through the relation:

$$V_s = V_f + \frac{kT_e}{2e}\ln\left(\frac{2m_i}{\pi m_e}\right). \tag{2.16}$$

2.3.3 ELECTRON ENERGY DISTRIBUTION FUNCTION (*EEDF*)

An additional advantage of the Langmuir probe is its ability to measure the electron energy distribution function (*EEDF*) in isotropic plasma. It has been shown by *Druyvesteyn* [41] in 1930 that the *EEDF*, $F_e(\varepsilon)$, is related to the second derivative of the probe characteristics through the expression:

$$\left[F_e(\varepsilon)\right]_{\varepsilon=eV} = \frac{4}{A_p e^2}\sqrt{\frac{m_e V}{2e}}\frac{d^2 I_e}{dV_p^2}, \tag{2.17}$$

where m_e and e are the mass and charge of electron, A_p is the probe area, I_e is the electron current in the retardation region, and $V = \left|V_p - V_s\right|$ is the probe potential with respect to the plasma potential. The electron density can be determined from [42]:

$$n_e = \int_0^\infty F_e(\varepsilon)\, d\varepsilon , \tag{2.18}$$

where ε represents the electron energy (equivalent to V) in eV. The effective electron temperature of the weakly ionized discharge can also be obtained from the *EEDF* through the integral:

$$T_{eff} = \frac{1}{n_e}\frac{2}{3}\int_0^\infty \varepsilon F_e(\varepsilon)\, d\varepsilon . \tag{2.19}$$

To determine the type of *EEDF*, the measured *EEDF* can be fitted by a function expressed as [42]:

$$F_{Type}(\varepsilon) = a\sqrt{\varepsilon}\exp\left(-b\varepsilon^x\right), \tag{2.20}$$

where a, b, and x are constants. If $x = 1$, it represents a Maxwellian distribution whereas the Druyvesteyn distribution is represented by $x = 2$.

CHAPTER 3 EXPERIMENTAL SETUP

3.1 INTRODUCTION

The experimental setup consists of two main parts, namely the radio frequency inductively coupled plasma (RF ICP) system and the Langmuir probe diagnostic circuit as shown in Figure 3.1. The RF ICP system is made up of the reactor chamber, vacuum pumps, gas handling system, RF generator and an impedance matching network. The Langmuir probe diagnostic circuit comprises an RF compensated Langmuir probe which is mounted on a linear motion drive, the probe bias voltage supply and the voltage-current monitoring system.

3.2 RF ICP SYSTEM

3.2.1 REACTOR CHAMBER

The plasma is generated in a cylindrical, stainless steel vacuum chamber shown in Figure 3.2. It has inner diameter 29.4 cm and height 30 cm (but the effective height from the surface of the dielectric to the surface of the top plate, h_{eff} is 20 cm due to the raised cylindrical portion of the bottom plate). There are 12 circular diagnostic ports (with NW50 end-flange) of internal diameter 5 cm located around the chamber in three levels protruding 7.5 cm from the wall of chamber. Two of the ports are used as observation windows, one each for gas in, rotary pump and turbo molecular pump

connection, one for the insertion of the Langmuir probe and the remaining are sealed with NW50 blank caps. The chamber is vacuum-sealed via 'O'-rings.

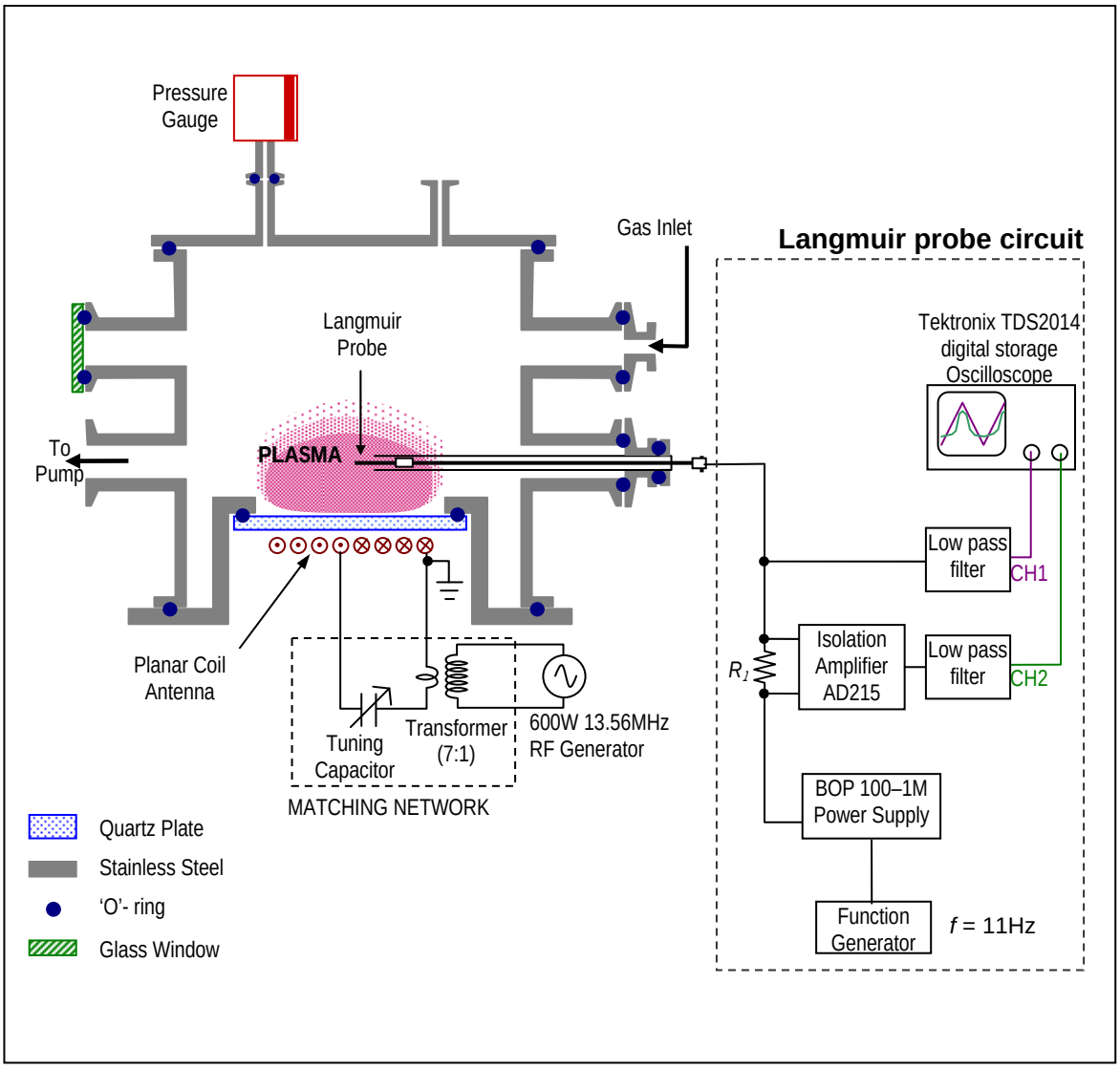

Figure 3.1: Schematic diagram of the inductively coupled RF discharge system and the Langmuir probe circuit.

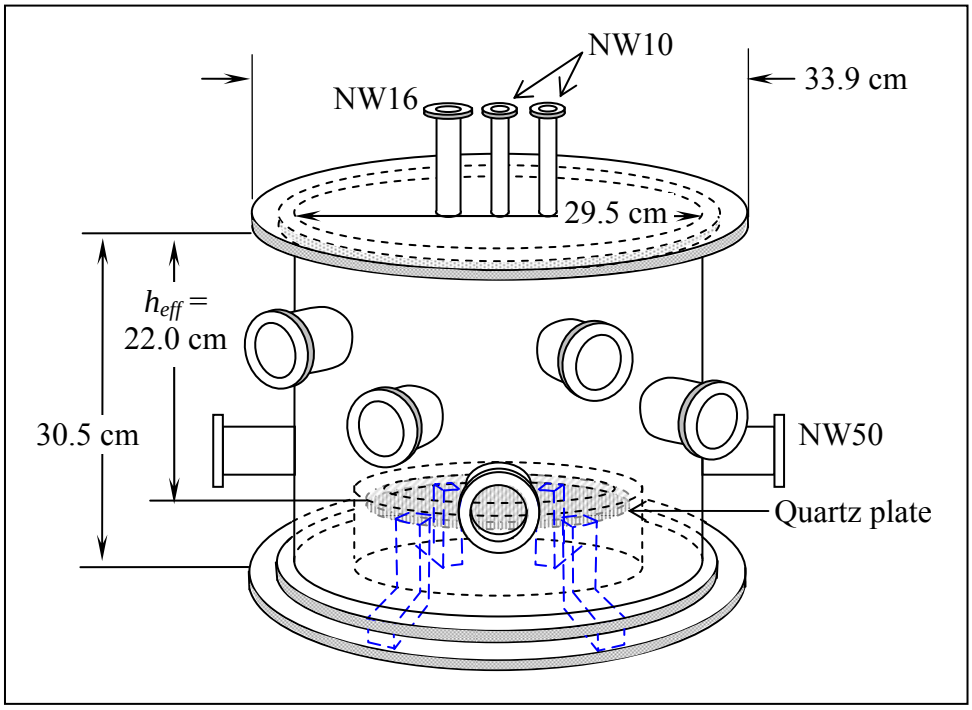

Figure 3:2: Schematic diagram of the ICP reactor chamber.

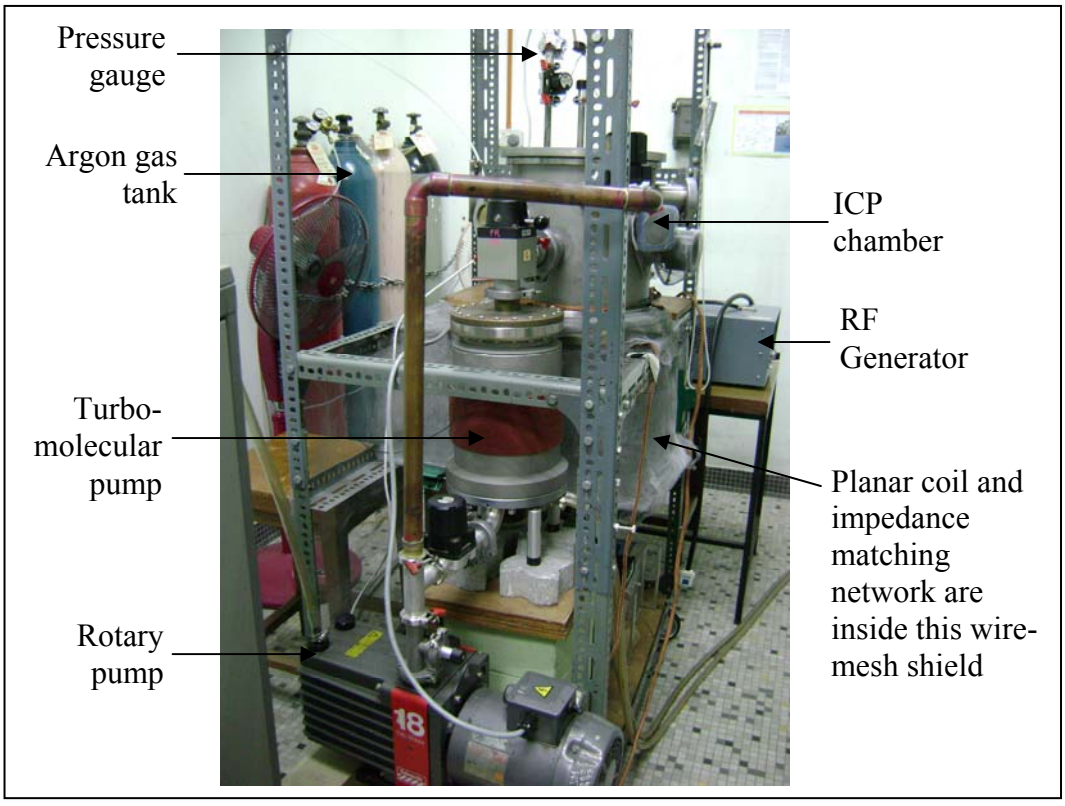

Figure 3:3: Picture of the ICP reactor chamber connected to the vacuum pumps.

The top and bottom covers are made of 1 cm thick stainless steel plate and diameter 37 cm. The bottom plate has a raised cylindrical platform, making it into a 'hat' shape structure. The raised cylindrical platform is of diameter 21.8 cm and height 9.9 cm. There is an opening of diameter 16.0 cm at the center of this platform where a quartz plate of 20.0 cm in diameter and 1.0 cm thick is held in place by four supports. The spiral planar coil (inductive element) is placed approximately 1 cm below the quartz plate. This quartz plate serves as a dielectric window to allow the RF magnetic flux to penetrate into the chamber for the generation of plasma. The top cover has three ports, one is mounted a *Pirani* pressure gauge, another a gas inlet valve (to bring the chamber to atmospheric pressure when required), and the third is covered with a blank cap.

3.2.2 VACUUM AND GAS HANDLING SYSTEM

The reactor chamber is connected to a rotary pump (Edwards 18 two-stage) via a diaphragm valve (Speedivalve) and to a turbomolecular pump (Model: KYKY) via a 90° elbow baffle valve (with manual console). The chamber pressure is measured by a capacitance manometer (Model: Leybold Barocel DM22) and its digital readout (Model: Leybold CM100). Both pressure gauges can read within the range of 10^{-3} mbar to 10^{2} mbar.

One of the diagnostic port of the ICP chamber is connected to a length of ¼ inch Teflon tubing through a NW16 diaphragm valve (Speedivalve). The tubing is then connected to a mass flow controller (Model: Dwyer GFC 2104) which allows the gas flow to be set within the range of 0 – 100 sccm. A +12V DC voltage supply was built to power and set the mass flow controller to functions of purging, valve off control, etc.

The circuit is shown in Appendix A. Another length of Teflon tubing then connects the mass flow controller to a gas regulator mounted at the head of the argon gas tank. Argon gas of 99.999% purity is used in the experiment.

The reactor chamber is first evacuated by a turbomolecular pump backed by a rotary pump to obtain a base pressure of the order of 10^{-4} mbar. When the base pressure is achieved, argon gas is filled into the chamber to flush out residues and subsequently set to the required pressure and flow rate by manually adjusting the lever of the elbow isolation valve between the chamber and the turbomolecular pump.

3.2.3 ELECTRICAL CONNECTION

The RF generator (Model: ENI ACG-5 XL) used is capable of supplying power up to a maximum of 600 W at 13.56 MHz into a 50 Ω load. The forward and reverse power can be read from the analog meters at the front panel of the RF generator. At RF frequency, a matching network is required to match the output impedance of the RF generator with the complex conjugate of the load impedance in order to gain maximum power transfer. The matching circuit as shown in Figure 3.4 consists of a step-down transformer where the secondary side is connected in series with a variable tuning vacuum capacitor C (from 56 pF to 720 pF) and the spiral planar coil antenna. The output resistance of the RF generator is 50 Ω while the load (plasma) resistance is expected to be around 1 Ω. As the difference is quite large, a step-down transformer with transformation ratio $a \approx 7$ can be used to bring their resistances to a closer match. Assuming the step-down transformer to be an ideal transformer with no loss and the coefficient of coupling k to be close to unity, the impedance of the primary circuit Z_p is related to that of the secondary circuit Z_s through the expression [43]

$$Z_p = a^2 Z_s , \qquad (3.1)$$

where the transformation ratio $a = N_p / N_s$. Substituting Z_p = 50 Ω and Z_s = 1 Ω into the equation (3.1) results in

$$a = \sqrt{\frac{Z_p}{Z_s}} = \sqrt{\frac{50}{1}} = 7.07 \cong 7 .$$

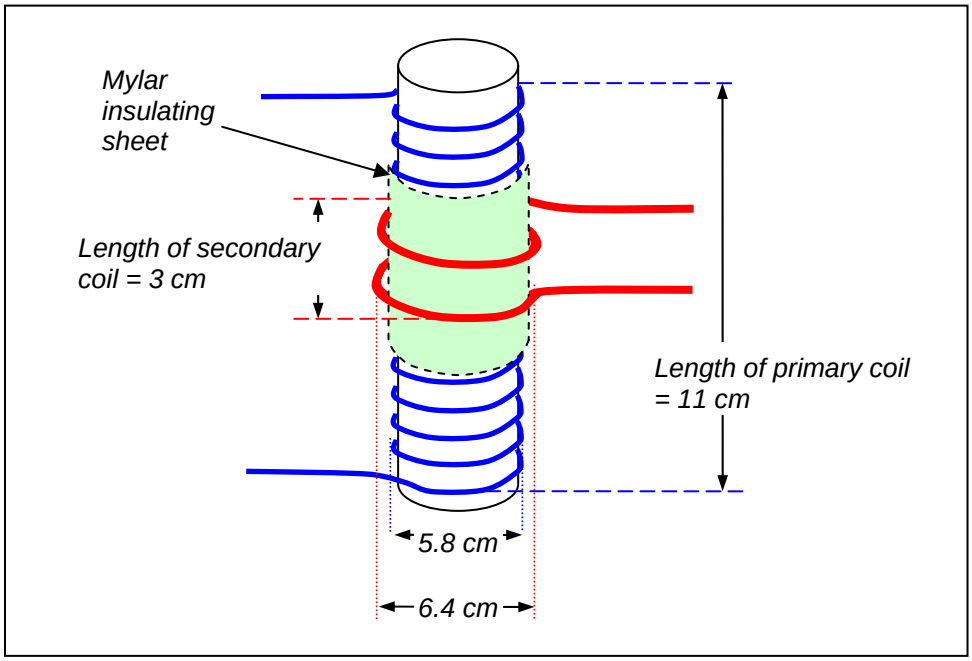

Figure 3.4: Dimensions of the step-down transformer for impedance matching.

The actual step-down transformer has turns ratio of 14:2 as shown in Figure 3.4. The primary coil is made of copper tubing (O.D. 5 mm) wound around a Perspex pipe and the average diameter of the coil is 5.8 cm. The adjacent turns are separated by air gap to prevent shorting such that the total length of the coil is approximately 11 cm. The secondary coil which encircles the primary coil is made of smaller diameter copper tubing (O.D. 3 mm) of 2 turns at average diameter 6.4 cm and length 3 cm. The measured open inductances of the primary and secondary coils are 4.24 μH and 0.76 μH

respectively. Bare copper tubing was used for more effective cooling (air cooled through a cooling fan). The primary coil is insulated from the secondary coil by inserting 3 layers of mylar sheet between them. Though the estimated coupling coefficient $k \sim 0.6$, the setup was found to perform very well in *E* mode discharge (zero reflected power) and satisfactorily in *H* mode discharge (< 3 % reflected power).

The spiral planar coil is made up of a six-turn hollow copper tube of outer diameter 3 mm, with the outermost turn having diameter 8.6 cm. The measured open inductance of the planar coil is 1.37 μH and its resistance is 5.7 mΩ. This gives a *Q*-factor, $Q = 2\pi f L_0 / R_0 \cong 20500$. Skin depth of the hollow copper tube at the frequency of 13.56 MHz is calculated to be approximately 18 μm. This inductive coil is situated 1 cm below the quartz window. The innermost turn of the coil is connected to the RF high voltage source while the outermost turn is connected to ground. To prevent the coil from overheating, a cooling fan is used during the experiment.

A schematic of the simplified coupling circuit [18] is shown in Figure 3.5. The coil inductance L_{cp} is the inductance when the plasma has been ignited and it is related to the coil inductance L_{co} in the absence of plasma through the relationship:

$$L_{cp} = L_{co} - \Delta L, \tag{3.2}$$

where ΔL is the difference between L_{cp} and L_{co}. The resistance R_t in the circuit is given by:

$$R_t = R_o + R_p\,, \tag{3.3}$$

where R_o is the circuit resistance in the absence of plasma and R_p is the additional resistance reflected into the circuit in the presence of plasma. The total reactance in the circuit is

$$X_t = 2\pi f L_{cp} - \frac{1}{2\pi f C}, \tag{3.4}$$

and the peak current is

$$I = \frac{V_0}{\sqrt{\left(R_g + R_t\right)^2 + X_t^2}}, \tag{3.5}$$

where V_o = open circuit peak input voltage. The current is at maximum when resonance occur at

$$2\pi f L_{cp} - \frac{1}{2\pi f C} = 0 \text{, or } f = \frac{1}{2\pi\sqrt{L_{cp} C}}. \tag{3.6}$$

In the *E* mode discharge at $f = 13.56\times10^6$ MHz and planar coil inductance ~1.4 μH, the tuned capacitance is expected to be 98 pF (the actual tuned value is 77 pF, which is off by 20 %).

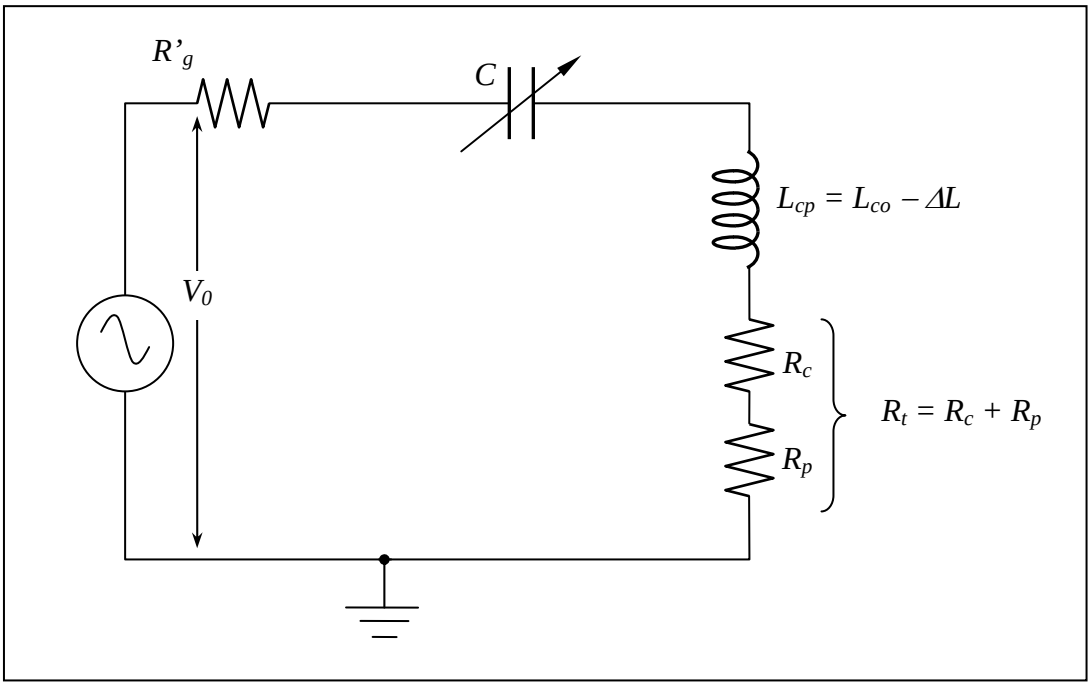

Figure 3.5: Schematic of the simplified coupling circuit.

3.3 LANGMUIR PROBE SYSTEM

The Langmuir probe is mounted onto a linear motion drive (Model: Huntington L-2111-6-SF) in order to semi-automate its movement inside the low pressure reactor chamber. This motion drive eases the radial measurements without having to shut down the generation of plasma just to adjust the position of the probe. Thus, a uniform and consistent plasma condition can be ascertained throughout the radial measurements, assuming the averaged plasma condition to be stable over time.

3.3.1 PROBE DESIGN

A cylindrical Langmuir probe used in this experiment is shown in Figure 3.6. Principally, a Langmuir probe consists of a probe tip and a RF filter which is connected to a RG402 coaxial cable with a BNC connector at the other end. The tip is immersed into the plasma.

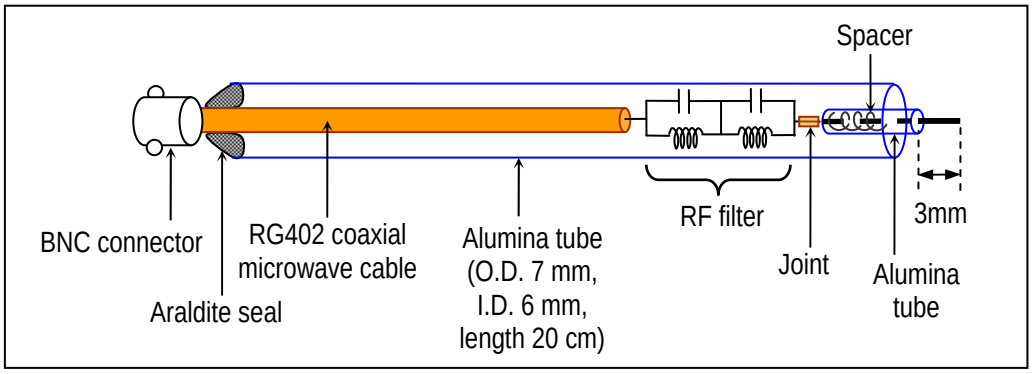

Figure 3.6: The cylindrical Langmuir probe assembly with RF filter.

Tungsten wire (purity 99.95%) is used as the probe tip due to its good resistance to chemical reaction, high melting point and high atomic number so as to ensure low

secondary electron emission caused by ions, electrons, photons and metastable bombardment which can erroneously be interpreted as ion or electron currents reaching the probe. The probe tip length should be longer than the radius of the probe tip, which in turn, should be smaller than the electron mean free path, λ_e at all gas pressures where the probe is used. The ratio of the probe tip length to radius is about 12 (l_p : r_p = 3 mm: 0.25 mm) such that the criteria, $l_p >> r_p$ and $\lambda_e >> r_p$ is satisfied at 0.1 mbar [$\lambda_e = (N\sigma)^{-1} = [2.41\times10^{15}\,\mathrm{cm}^{-3}\cdot\pi(1.82\times10^{-8})^2\,\mathrm{cm}^2]^{-1} \approx 4$ mm; N = gas number density and σ = collision cross section]. In the *E* mode discharge where $n_e \sim 10^9$ cm^{-3} and $T_e \sim$ (2–3) eV, the Debye length, λ_D is (0.03–0.04) cm, and $\xi = r_p / \lambda_D \sim 1$. In the *H* mode discharge, $n_e \sim 10^{11}$ cm^{-3} and $T_e \sim$ (1-2) eV, giving $\lambda_D \sim$ (0.002–0.003) cm and $\xi = r_p / \lambda_D \sim 10$. Under these conditions, we have $r_p[\ln(l_p / 2r_p)] = 0.045\,\mathrm{cm} << \lambda_e$ and $\lambda_D << \lambda_e$. Therefore, the assumptions of non-intrusive small probe and collisionless probe sheath are satisfied so that the Langmuir probe method and the Druyvesteyn formula for *EEDF* are valid [44].

The exposed probe tip should not be in electrical contact with any conducting coatings that may be deposited onto the insulating alumina tube. Thus, an additional thin tungsten wire of 0.05 mm in diameter is wrapped around the probe, serving as a 'spacer' to prevent the probe from touching the alumina tube. The tip and 'spacer' assembly is inserted into a thin-walled Alumina tube of length 2.5 cm (I.D. = 0.6 mm, O.D. = 0.7 mm for the tip of diameter 0.5 mm; and I.D. = 0.3 mm, O.D. = 0.6 mm for the tip of diameter 0.2 mm). Tungsten wire cannot be lead-tin soldered to a copper conductor, thus, it is inserted into a short thin close-fitting copper tube which is then flattened via a G-clamp tool to fit firmly ensuring good electrical contact. The other end flattened copper tube is soldered to the lead of the RF filter built on a mini-PCB board

as shown in Figure 3.7(a). The other end of the mini-PCB board is soldered to the inner conductor of a 50 Ω solid RG402 microwave coaxial cable. The mini-PCB board is wrapped with two layers of thin Mylar sheet (for insulation) and then an outer layer of aluminium foil which extends to contact the outer conductor of the coaxial cable. The outer conductor of the coaxial cable is grounded. The probe assembly is inserted into a 20 cm long alumina tube to shield the conducting surfaces (except the probe tip) from the plasma (Figures 3.6 and 3.7(b)). The outer alumina tube is fastened to the coaxial cable with araldite epoxy at one end. The BNC connector at the end of the coaxial cable serves as the electrical connection to the data acquisition electronics outside the chamber. The Langmuir probe is mounted on a specially designed platform fastened onto the linear motion drive. The entire probe assembly is mounted onto one of the diagnostic port of the chamber to enable the probe to be inserted into the plasma under vacuum condition.

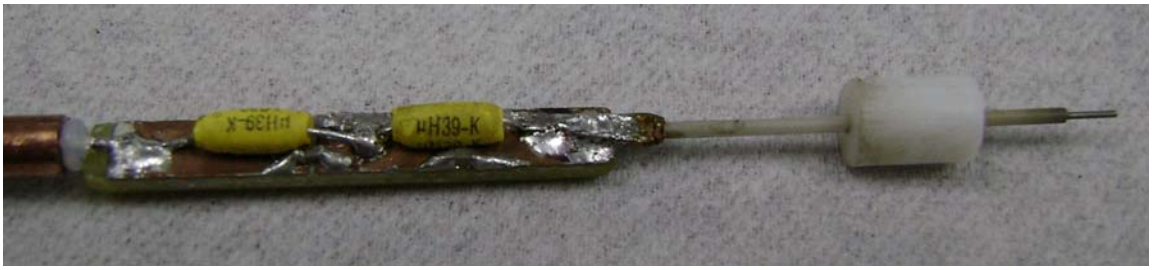

Figure 3.7(a): Probe tip and RF filter board.

Figure 3.7(b): Langmuir probe mounted onto a linear motion drive.

3.3.2 RF FILTER

A miniature RF filter at the fundamental drive frequency as well as its harmonics is connected just behind the probe tip to minimize the RF distortion caused by the RF fluctuations in the plasma potential picked-up by the probe tip. In this filter, a resonant filtering technique (tuned probe) proposed by *Gagne and Cantin* [45] for a symmetrically driven RF discharge at frequency 13.56 MHz has been used. LC filters with a self-resonance at 13.58 MHz and 27.04 MHz each have been employed to achieve the maximum filter impedance at the applied fundamental RF drive frequency and its second harmonics.

In each LC filter, a pair of surface mount capacitors with dimensions of 1 mm × 1.5 mm and an inductor (2.5 mm in diameter and 6 mm in length) is used. The surface mount capacitor is used due to its small size which reduces stray capacitance as compared to the normal size capacitor used in any electrical circuit. Two parallel capacitors of 330 pF and 22 pF each (effective capacitance of 352 pF) are connected in parallel with the 0.39 μH RF inductor to form the RF filter resonance at 13.58 MHz. To form the RF filter resonance at 27.04 MHz, two capacitors of 82 pF and 6.8 pF each (effective capacitance 88.8 pF) are connected in parallel with a 0.39 μH inductor. These two pairs of filters are soldered on a mini-PCB board. The value of capacitance and inductance chosen is subjected to the commercially available values to obtain the frequency which is nearest to 13.56 MHz and 27.12 MHz. The frequencies obtained at 13.58 MHz and 27.04 MHz differ by 0.15 % and 0.29 % from the RF drive frequency and its 2^{nd} harmonics, respectively. Hence, most of the RF fluctuations at fundamental RF drive frequency as well as its second harmonic from the plasma would almost be eliminated.

3.3.3 PROBE CIRCUIT

A Langmuir probe circuit is shown in Figure 3.1. Basically, the circuit consists of the Kepco Bipolar Operational Power Supply/Amplifier (Model: BOP 100W), 20 MHz Function Generator (Model: TG120), constructed Differential Amplifier based on the AD215 Unity Gain Isolation Amplifier, a pair of RC Low Pass Filter and an 8-bit Tektronix Four-Channel Digital Storage Oscilloscope (Model: TDS2014) with PQI 32MB compact flash card to store the data.

The RF compensated Langmuir probe is located at the central axis of the reactor chamber of about 4.6 cm above the quartz window for radial distribution measurement of the plasma properties. The bias potential to the probe is provided by the Kepco bipolar operational amplifier capable of supplying from −100 V to +100 V and maximum current of 1 A with output resistance of 2 mΩ. The time-varying biasing potential to the probe is supplied by a triangular wave generated from the function generator with the signal amplified by the Kepco bipolar operational amplifier. The probe voltage is measured by the oscilloscope. The probe current is measured as the voltage drop across the current monitoring resistor, R_I by a constructed differential amplifier using the AD215 isolation amplifier. The circuit is shown in Appendix B. The probe current is determined using the Ohm's law. The RF noise picked-up by the transmission cable is filtered by the RC low pass filter which is placed at two of the input channels of the oscilloscope. All the data are stored in the memory card which is then transferred to the computer for data analysis.

3.3.4 TEST MEASUREMENT OF THE *I-V* CHARACTERISTIC

3.3.4.1 Dependence of the Current Monitoring Resistance on the Probe Current

The current monitoring resistance, R_I, chosen for the experiment is very crucial to obtain the correct probe current. Three R_I values (10 Ω, 22 Ω, and 1 kΩ) were used to investigate the effect of the resistance on the probe voltage and current, especially at *H* mode (RF power = 80 W, Ar pressure = 0.1 mbar, gas flowrate = 30 sccm) which has increased ionization rate by two orders of magnitude and loading in the probe circuit is likely to occur. The probe voltage signals $V_p(t)$ measured at various R_I are shown in Figure 3.8. It is observed that the voltage signal is heavily distorted when R_I = 1 kΩ whereas R_I = 10 Ω produces no distortion. Figure 3.9 shows the corresponding I_p-V_p curves. Because of the loading at large R_I, the higher current end cannot be measured.

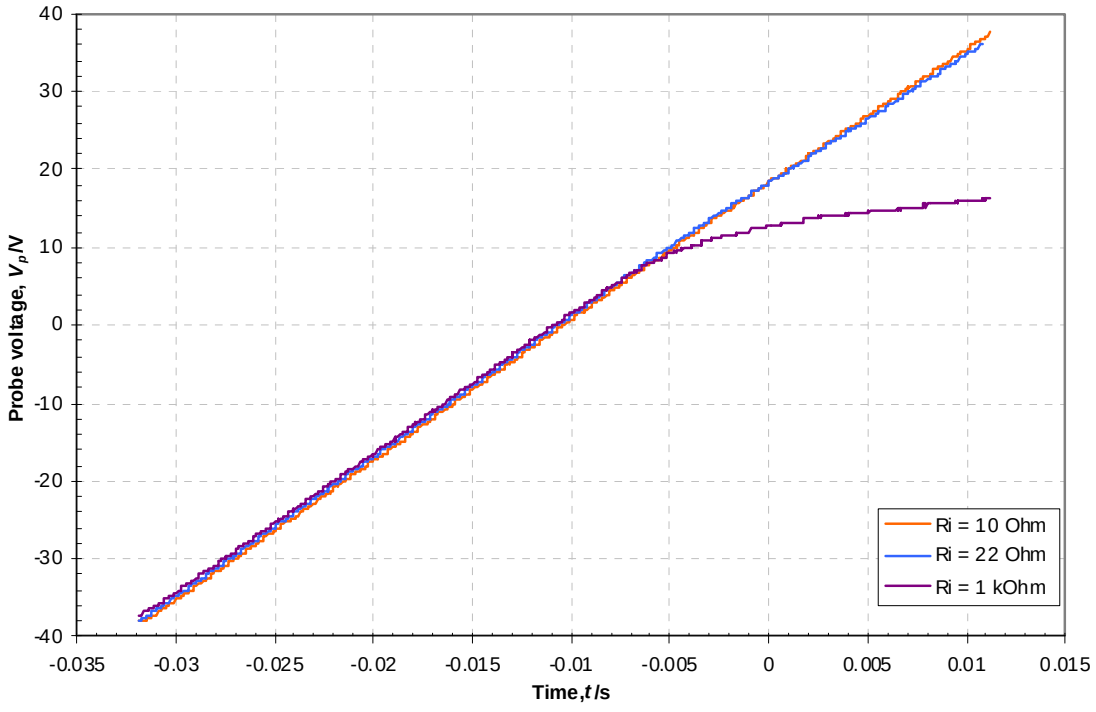

Figure 3.8: Graph of V_p against time at RF power of 80 W, argon pressure of 0.1 mbar at flowrate of 30 sccm.

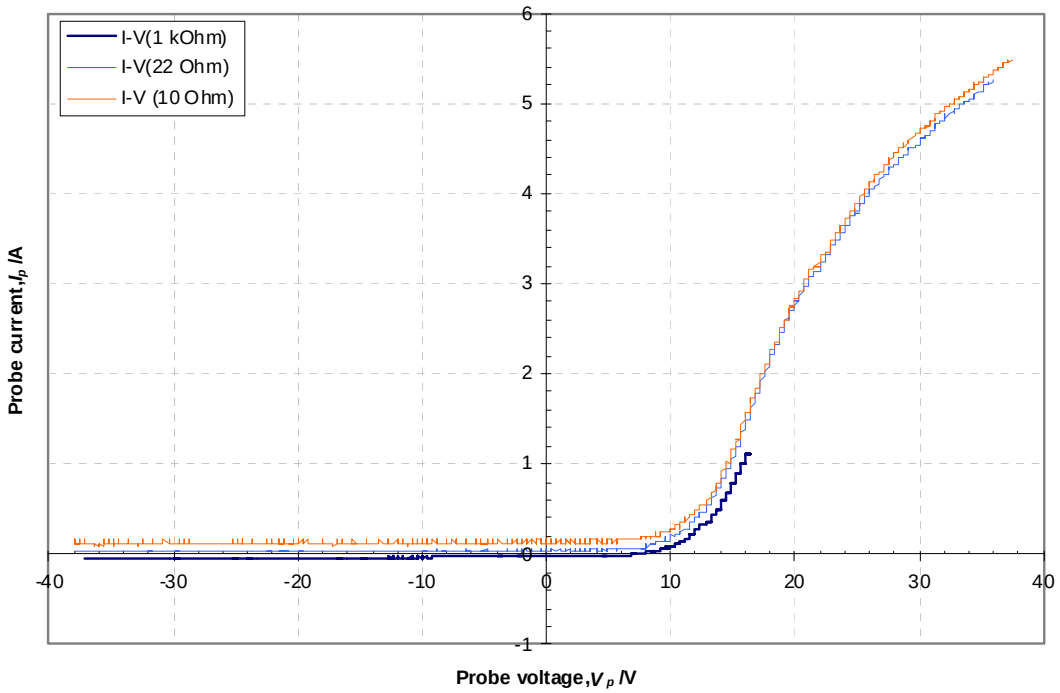

Figure 3.9: Graph of I_p against V_p at RF power of 80 W, argon pressure of 0.1 mbar at flowrate of 30 sccm.

Large R_I would dominate the probe circuit resistance R_C (includes the probe driver output resistance R_O, resistance of probe wire R_W, contact resistance R_{ct}, resistance of RF filter R_{ft}, sheath resistance near chamber wall R_{Sw}, and surface resistance of discharge chamber R_{sf}) [44]. This results in a voltage reduction $\Delta V = I_p R_C$ across the probe sheath, bringing major effect near the plasma potential where I_p and ΔV are large. A relatively small distortion in the *I-V* characteristic will manifest itself in the flattening of the second differentiation of probe current d^2I_p/dV_p^2, hence, enormously depleting the low-energy electrons in the measured *EEDF*. This is likely to smooth out the 'knee' near the plasma potential of the *I-V* curve, which is observed for the *E* mode discharge where $R_I = 1\ \mathrm{k}\Omega$ is used in order to obtain a measurable value of the very small probe current. In the *H* mode discharge, $R_I = 10\ \Omega$ is used as large probe current is collected and to prevent loading so that the probe bias potential remains stiff.

3.3.4.2 Dependence of the Hysteresis in the *I-V* Characteristic of the Probe on the Frequency of the Bias Voltage to the Probe

The Langmuir probe is tested in the absence of plasma with argon pressure of less than 0.001 mbar to determine the dependence of the Lissajous figure of the *I-V* plot on the frequency of the probe bias voltage. This is to ensure that the *I-V* characteristic would not be affected by stray capacitances of the probe circuit. The frequency of the probe bias voltage is varied between 10 Hz and 1.05 kHz at fixed argon flowrate of 30 sccm. The current monitoring resistor of 1 kΩ is used to determine the probe current.

The probe voltage, V_p, and current, I_p, measured are plotted as a function of time, as shown in Figures 3.10 (on the left side). Plotting I_p against V_p gives the Lissajous figures for f = 1.05 kHz, 100 Hz, 40 Hz and 11 Hz shown respectively in Figures 3.10 (a) – (d). The hysteresis phenomenon in the Langmuir probe circuit is represented by the Lissajous diagram which resembles a parallellogram. It is observed that larger hysteresis occurred at higher frequency of the probe voltage. Minimum phase shift occurs at 11 Hz and almost no hysteresis is observed, hence, this frequency is chosen to sweep the bias voltage to the probe. Lower frequency could not be used due to the limitation of the function generator. This linear background current $I_{p(background)}$ in the absence of plasma which is due to the circuit parameters has to be subtracted from the probe current I_p collected when the plasma is present.

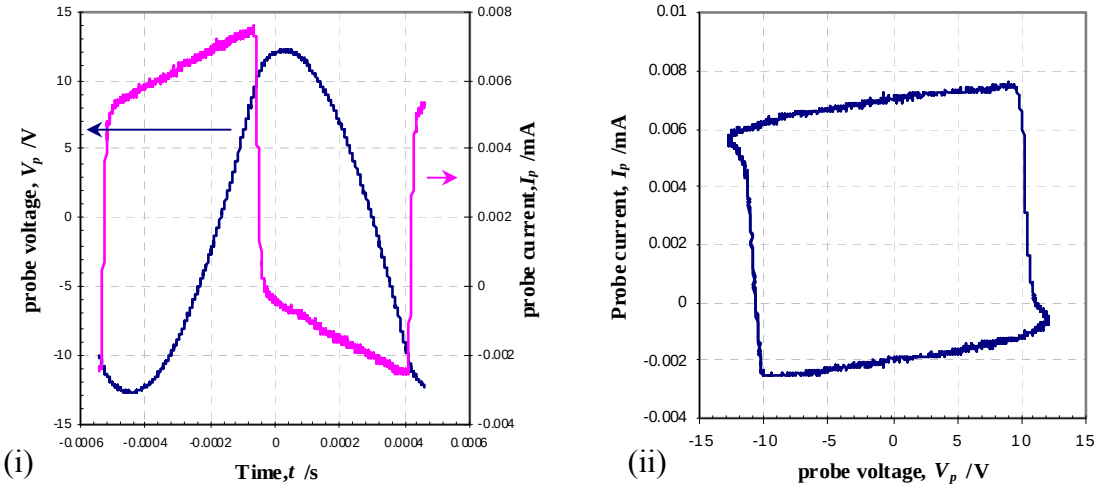

(i) (ii)

Figure 3.10(a): (i) Graph of I_p and V_p against time, (ii) Lissajous figure of I_p – V_p over one full cycle at 1.05 kHz.

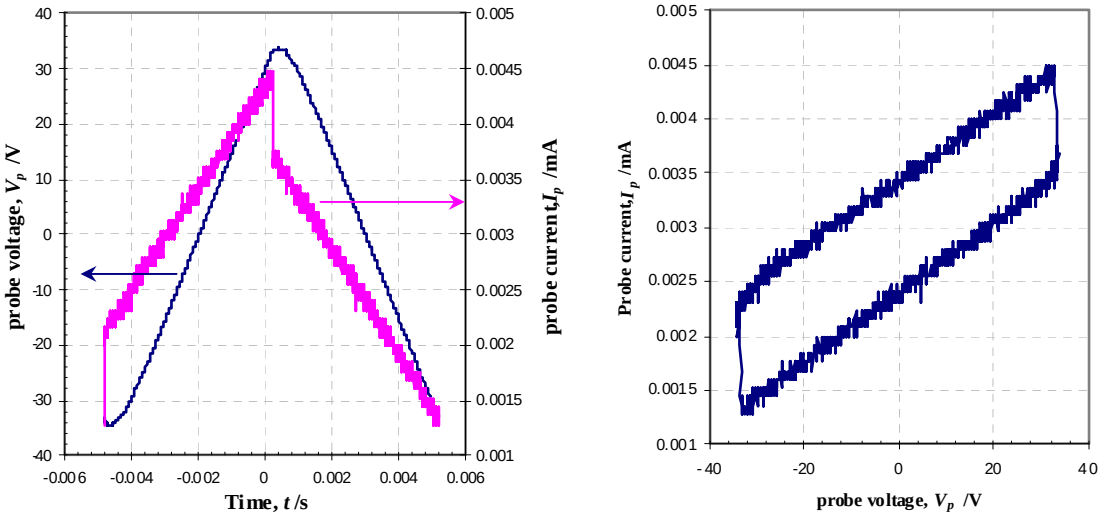

(i) (ii)

Figure 3.10(b): (i) Graph of I_p and V_p against time, (ii) Lissajous figure of I_p – V_p over one full cycle at 100 Hz.

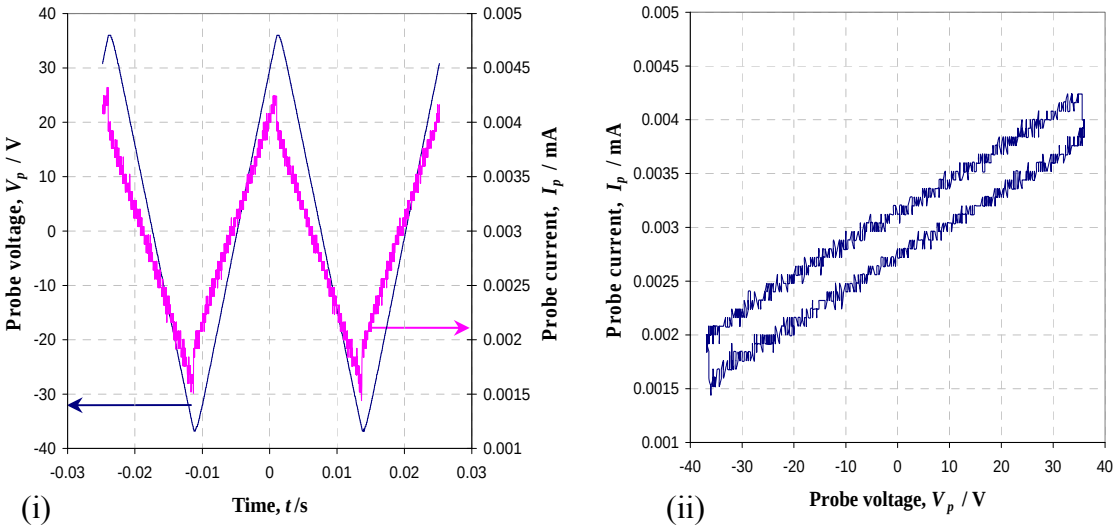

Figure 3.10(c): (i) Graph of I_p and V_p against time, (ii) Lissajous figure of I_p – V_p over one full cycle at 40 Hz.

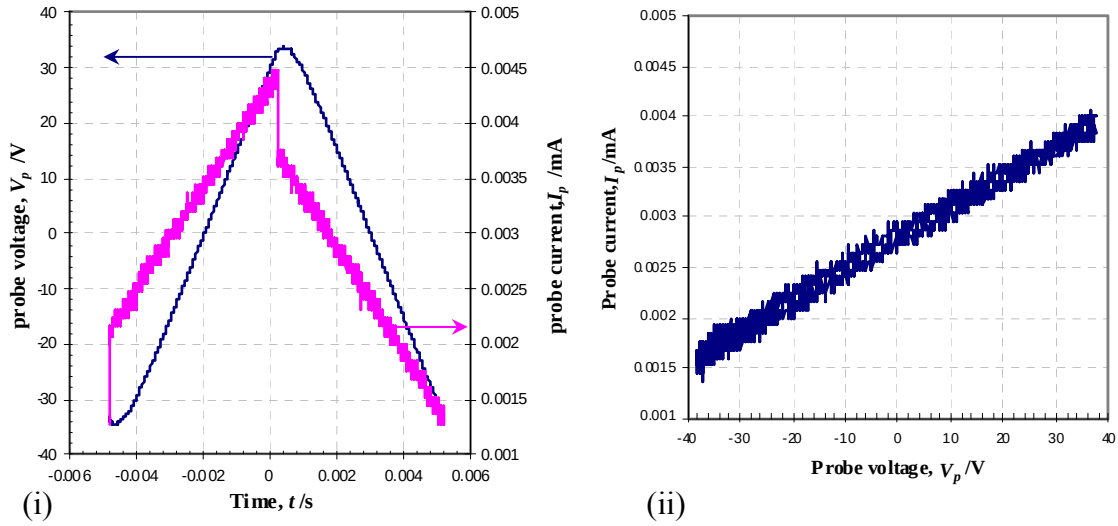

Figure 3.10(d): (i) Graph of I_p and V_p against time, (ii) Lissajous figure of I_p – V_p over one full cycle at 11 Hz.

3.3.4.3 Typical *I-V* Characteristics of the Probe

The idealized *I-V* characteristic of the Langmuir probe was shown in Figure 2.1 and the interpretation of the plasma parameters has been described in Section 2.3. A typical *I-V* curve for the *E* mode discharge is shown in Figure 3.11(a) and the corresponding semi-log plot of the electron current, I_e versus V_p, in Figure 3.11(b). A straight line is drawn through the ion saturation region and extrapolated to the electron retardation and saturation regions. The electron current is obtained by subtracting the ion current (from the straight line) from the collected probe current.

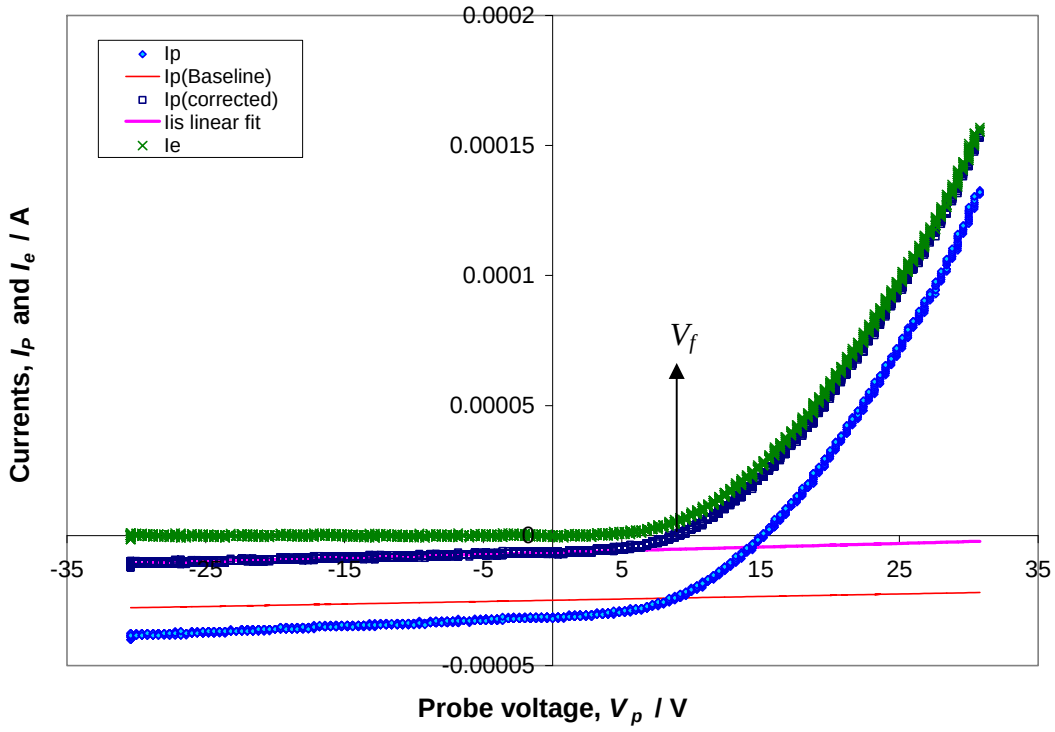

Figure 3.11(a): Plot of I_p and I_e versus V_p plot for *E* mode discharge at input RF power 10 W (0 W reflected) and pressure 0.1 mbar.

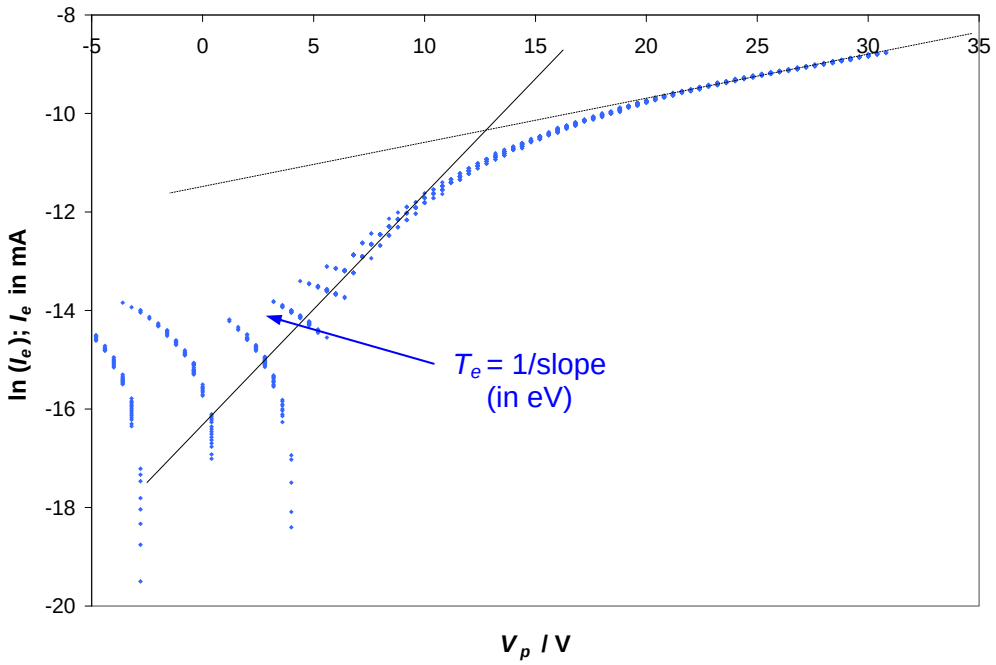

Figure 3.11(b): Corresponding plot of ln(I_e) versus V_p.

Figure 3.11(a) does not exhibit the classical shape as the 'knee' is not distinct at all and is usually the case at very low densities. However, electron temperature could still be determined from the slope of ln(I_e)-V_p plot shown in Figure 3.11(b). The time-averaged plasma potential V_s is calculated using Equation 2.16 with known floating potential V_f. On the consideration of the appropriate theory for the ion saturation current, plots of (ion current at saturation region, I_{is})^x versus V_p are shown in Figures 3.11(c) and (d) for x = 2 (OML approach) and x = 4/3 (Child-Langmuir (CL) consideration) respectively in comparison to x = 1. The raw data points have a spread of 13 % due to the resolution limit of the 8-bit oscilloscope (even after averaging over 16 scans). By reading the fitted I_{is} at V_f (at I_p = 0), the OML consideration resulted in I_{is} having a magnitude 13 % lower than that of x = 1 fitting, while the CL consideration yields 6 % lower. As both OML (applicable when $r_p/\lambda_D << 1$) and CL (applicable in moderate densities as in ICPs [39]) gives lower I_{is} by (6 – 13) %, this is within the

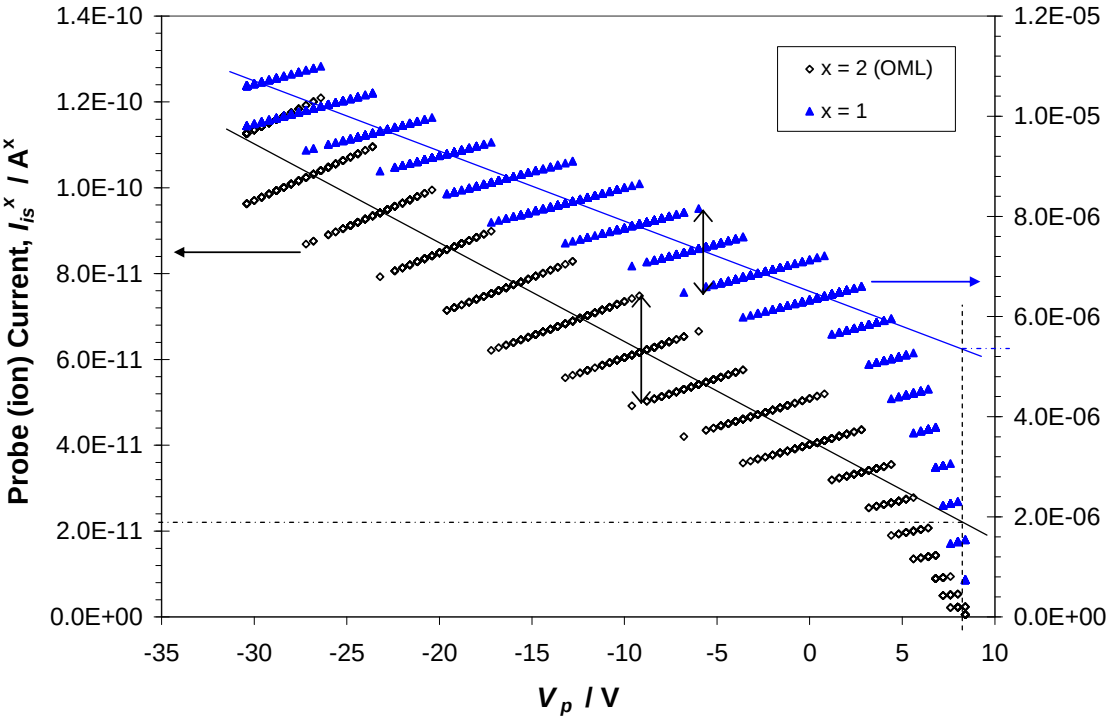

Figure 3.11(c): Plot of I_{is}^{x} versus V_p for the same E mode discharge. $x = 2$ and $x = 1$.

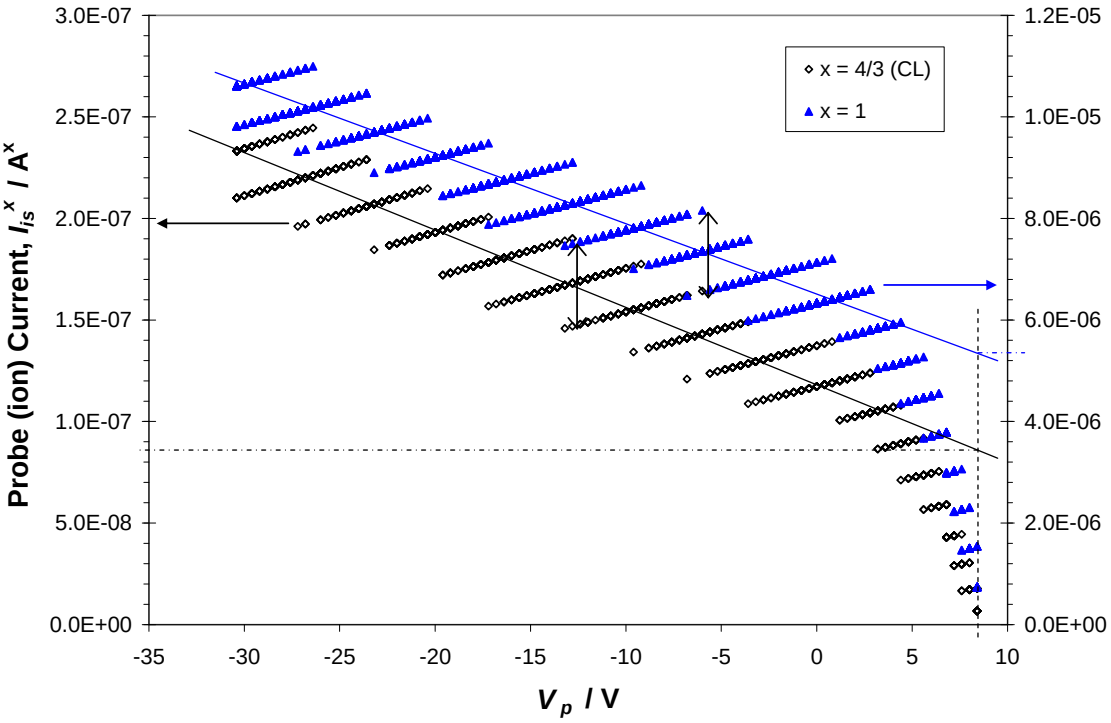

Figure 3.11(d): Plot of I_{is}^{x} versus V_p for the same E mode discharge. $x = 4/3$ and $x = 1$.

resolution spread of the data points. As such, a linear fit of I_{is} using $x = 1$ will be used. The electron density will then be deduced from the I_{is} at floating potential using Equation 2.12.

For the the *H* mode discharge at 100 W RF input power (5 W reflected) and 0.1 mbar argon pressure, a typical set of *I*-*V* curves is shown in Figures 3.12(a) – (c). No correction for the probe current was required as the baseline voltage monitored across $R_I = 10\ \Omega$ is zero. Due to the poor resolution in the raw data points at the ion saturation region (Figure 3.12(c)), the ion saturation current is fitted to a flat line as shown in Figure 3.12(a). Electron current I_e is extracted after subtracting this I_{is} from I_p.

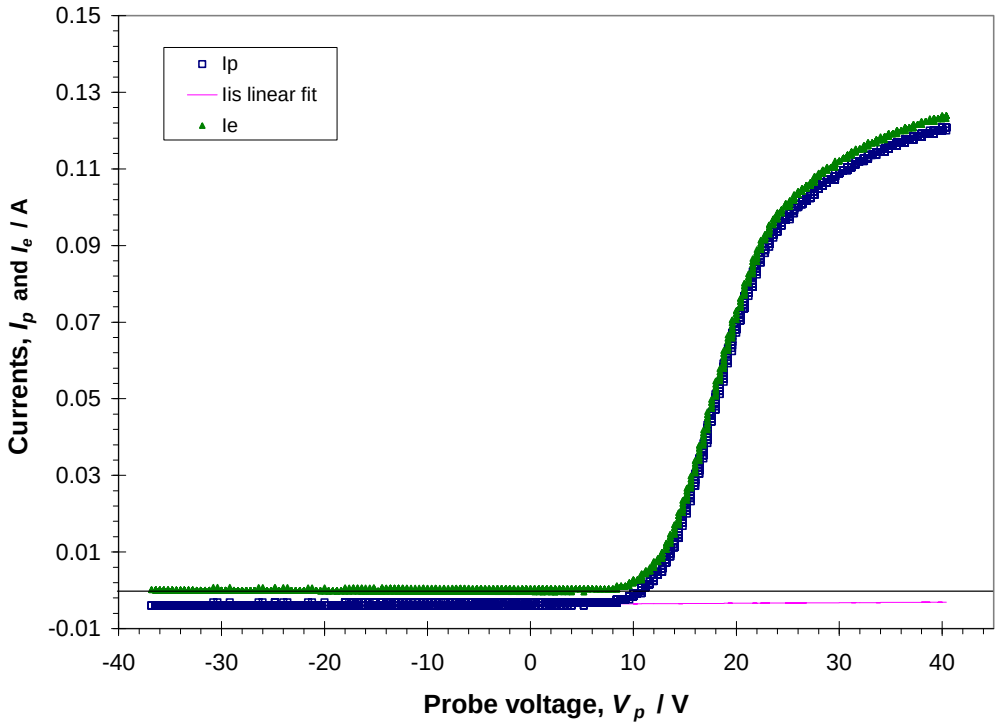

Figure 3.12(a): Plot of I_p and I_e versus V_p plot for *H* mode discharge at input RF power 100 W (5 W reflected) and pressure 0.1 mbar.

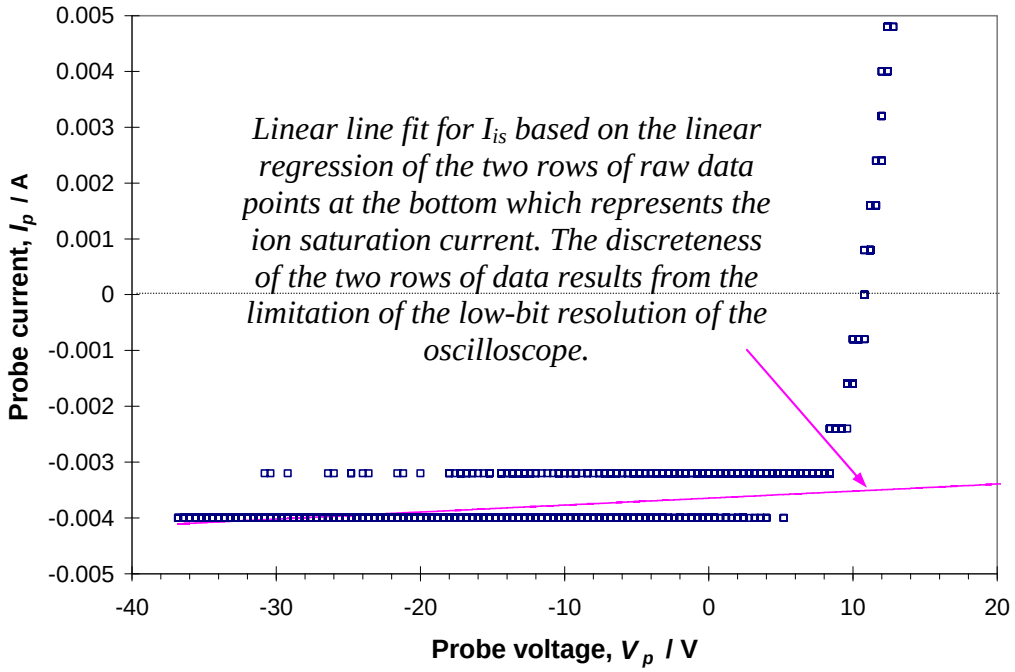

Figure 3.12(b): Expanded ion saturation region of Figure 3.12(a).

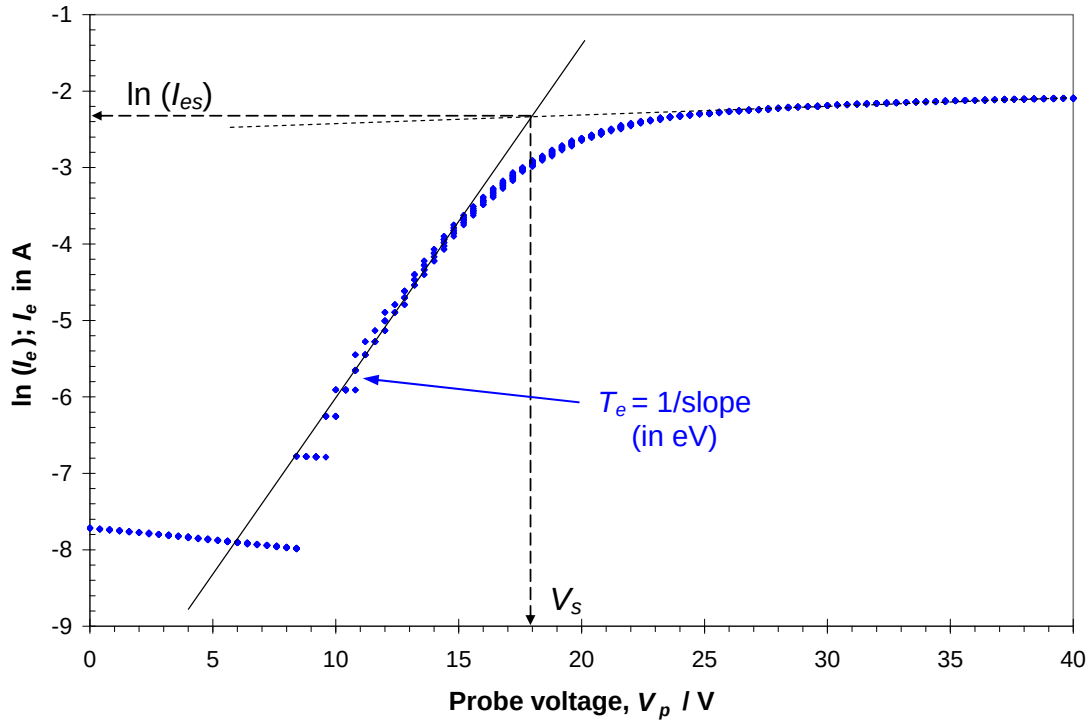

Figure 3.12(c): Corresponding plot of ln(I_e) versus V_p.

Since the 'knee' and the electron saturation region are now distinct, the plasma potential V_s can now be determined from the abscissa value of the intersection between the extrapolated tangent lines from portions of electron collection currents at regions $V_p < V_s$ and $V_p > V_s$ in the $\ln(I_e) - V_p$ plot. The corresponding I_e value at this intersection point is taken to be the electron saturation current I_{es}. The slope of the linear electron retardation region in the same plot gives the electron temperature. The electron density n_e is then deduced from the electron saturation current through Equation 2.5.

3.3.5 ELECTRON ENERGY DISTRIBUTION FUNCTION (*EEDF*)

The Druyvesteyn formula given in Equation 2.16 is applicable if the distribution function is assumed to be isotropic. The plot of the second derivative $(d^2I_e/dV_p^2)V^{½}$ against V can give a representation of the *EEDF*. However, a smoothing process is first performed on the digitized raw data points in order to extract reasonably smoothed second derivative of the electron current. This smoothing process is done digitally via the method reported by *Fujita and Yamazaki* [46]. It is based on the method advocated by *Savitsky and Golay* [47] in which the least squares principle is employed to fit the experimental data to a polynomial curve, and then differentiated to second order by convolution with weighting functions. A computer program written in C++ to perform the digital smoothing differentiation is given in Appendix C.

The degree of smoothing depends on the integer fitting width, m. Too small a width will result in large oscillations, especially in the second derivative at the low current end (high electron energy). This is due to poor resolution limited by the 8-bit digitizing storage oscilloscope. The 256 points (8-bit) on the vertical scale allows maximum resolution of only 3.1% of Full Scale. On the other hand, too large a fitting

width will lower and broaden the peak of the *EEDF*, as well as showing a higher plasma potential. For the set of data obtained under operating conditions of RF power 200 W, Ar pressure 0.10 mbar, and flowrate 20 sccm, various fitting widths are used and shown in Figure 3.13. It is deduced that the best compromise is fitting width, $m = 140$.

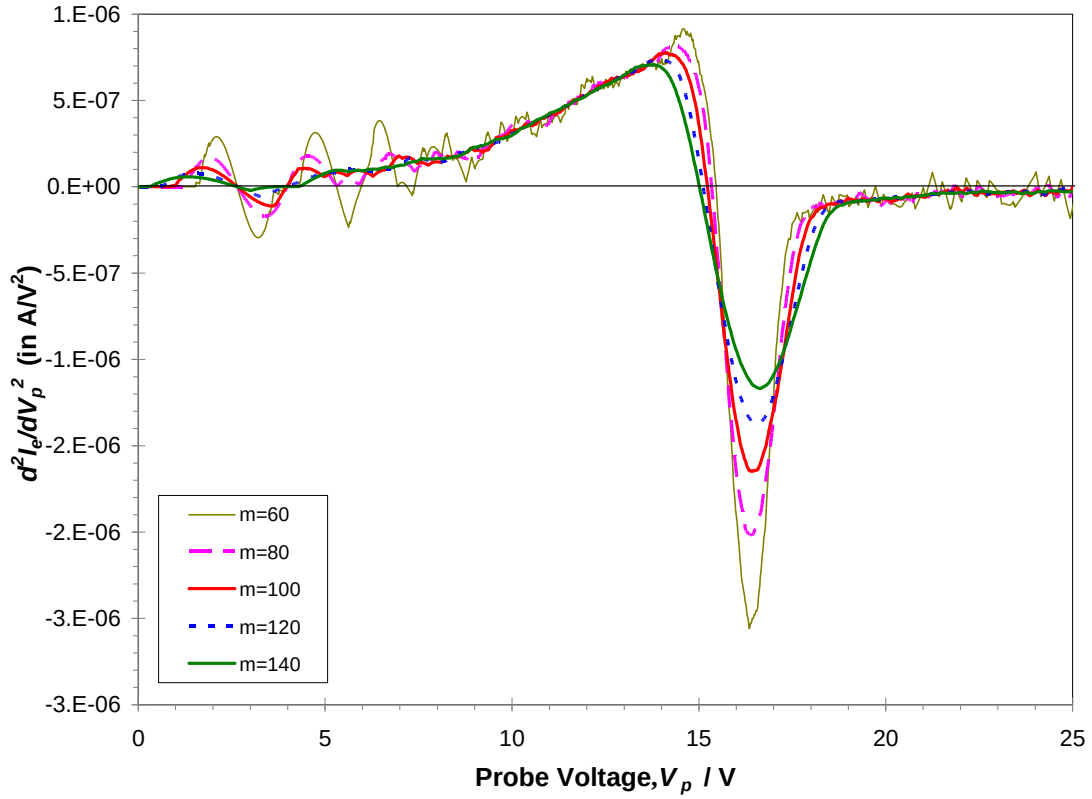

Figure 3.13: The second derivative d^2I_e/dV_p^2 at five different fitting widths: $m = 60$, 80, 100, 120 and 140.

A sample plot of the raw *I-V* characteristic (at RF power 200 W, Ar pressure 0.10 mbar, and flowrate 20 sccm) and its corresponding smoothed first and second derivatives is shown in Figure 3.14 and the computed electron probability function defined as $EEPF = \sqrt{V}\,\frac{d^2 I_e}{dV_p^2}$ is shown in Figure 3.15.

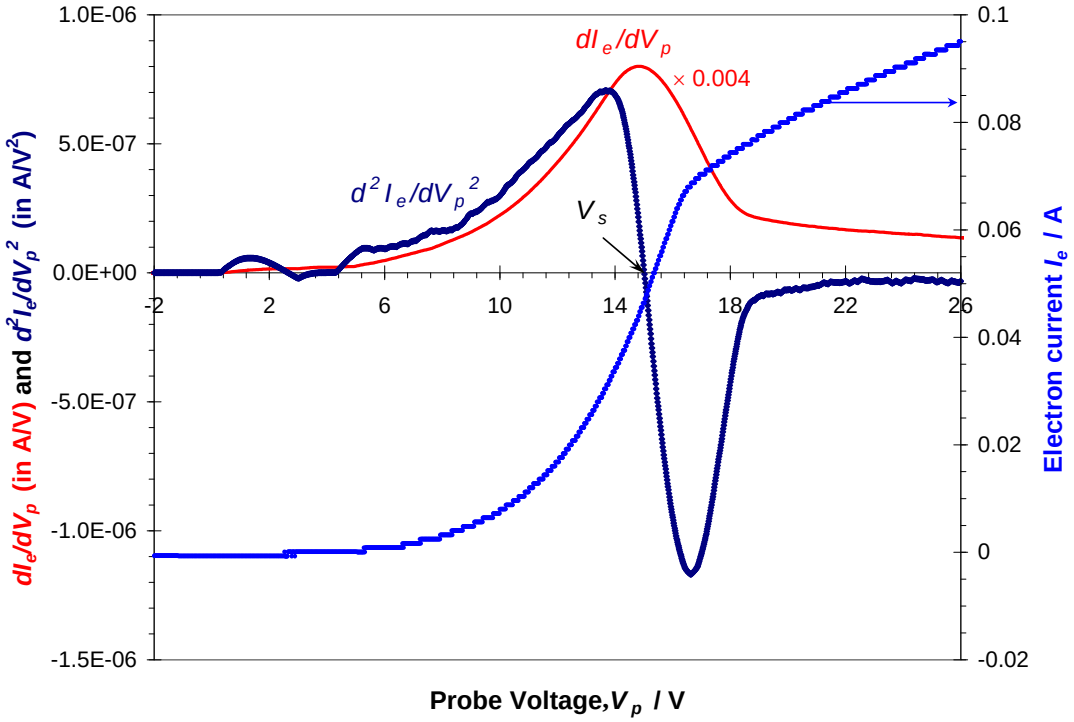

Figure 3.14: Raw *I-V* curve and its smoothed first and second derivatives at 200 W, 0.10 mbar, 20 sccm with $m = 140$.

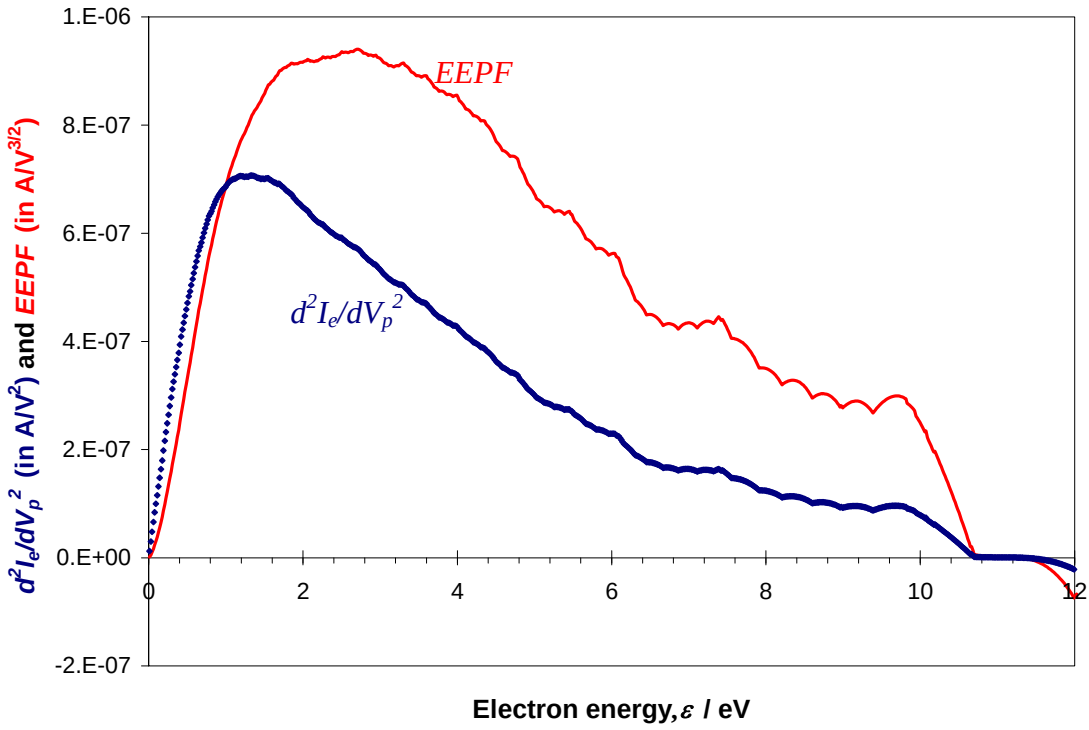

Figure 3.15: 2nd derivative and *EEPF* at 200 W, 0.10 mbar, 20 sccm with $m = 140$.

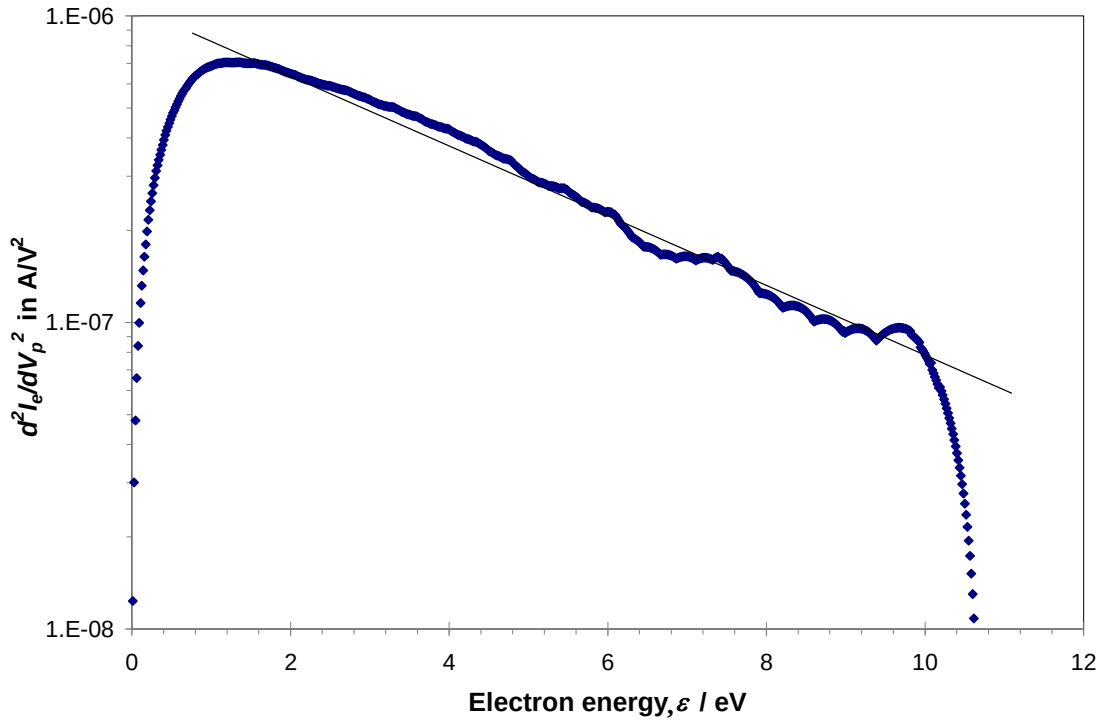

Figure 3.16(a): Semi logarithmic plot of d^2I_e/dV_p^2 against ε shows linear dependence confirming a Maxwellian-like distribution.

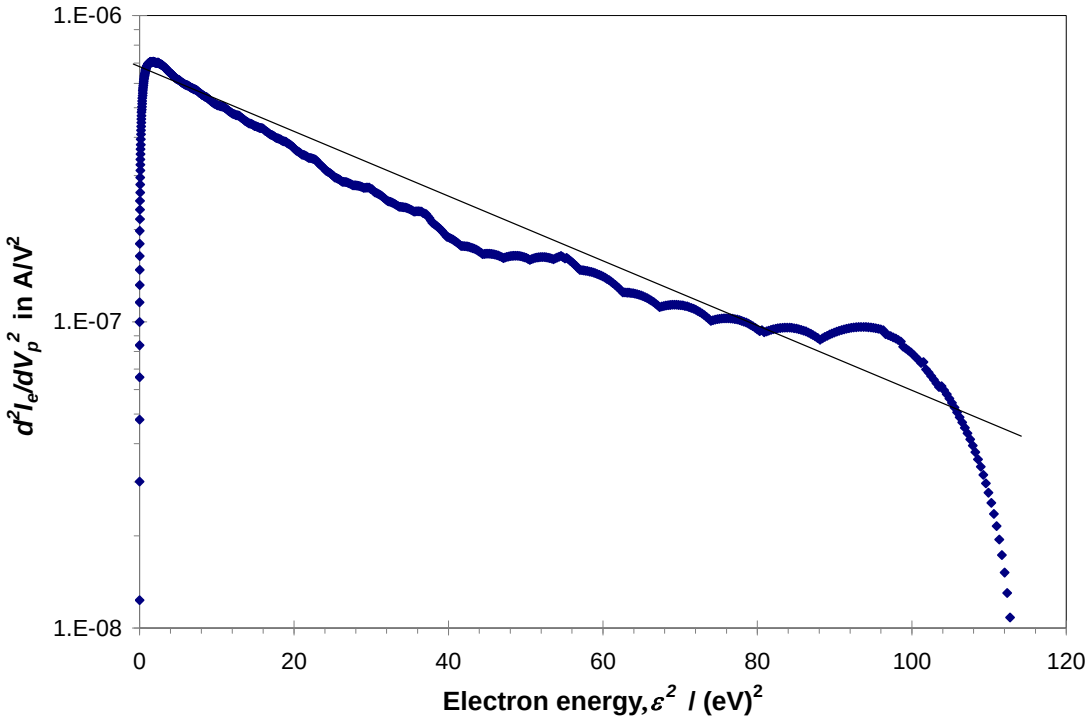

Figure 3.16(b): Semi logarithmic plot of d^2I_e/dV_p^2 against ε^2 does not show linear dependence confirming a non-Druyvesteyn-like distribution.

To determine the type of electron energy distribution, semi-log plots of (d^2I_e/dV_p^2) against ε and ε^2 are plotted in Figures 3.16(a) and (b). It can be seen that the sample set obtained at 200 W RF input power under *H* mode, 0.10 mbar argon and 20 sccm flowrate, the electron energy distribution is Maxwellian-like.

In the case of *E* mode, the second derivative of the electron current with respect to the probe voltage extracted is heavily distorted especially near the 'knee' region of the electron saturation current. These will be shown in Section 5.2.5.

3.4 ELECTRICAL MEASUREMENT

The electrical properties of the ICP system such as RF breakdown characteristics, *E*-*H* mode transition and power coupling efficiency are determined by measuring the electrical variables of the inductive coil that excites the discharge. The coil voltage, V_{coil} is monitored using a high voltage probe (Model: Tektronix P6015A) with attenuation factor 1000× and the coil current, I_{coil} is measured by a current probe (Model: Pearson 105) with sensitivity 0.5V/A. The signals are displayed in an 8-bit digital storage oscilloscope (Model: Tektronix 2014). The stored data are transferred to the computer for processing using Microsoft EXCEL spreadsheet.

In addition, the electrical characteristics at the primary and secondary sides of the step-down transformer are also investigated in the consideration of impedance matching parameters. The high voltage probe is then connected directly across the primary or the secondary coils for the relevant measurements. The current probe is placed near the grounded end of the current path of the relevant primary and secondary loops. The points at which measurements are made are shown in Figure 3.17. The RF

input power and reflected power are read from the analog power display at the front panel of the ENI ACG-5 XL RF generator.

For the breakdown characteristics, the RF power is very slowly increased from zero until a discharge is just visible. The voltage of the planar coil measured just before the ignition (where the coil voltage drops very slightly immediately after ignition), and the corresponding current are noted.

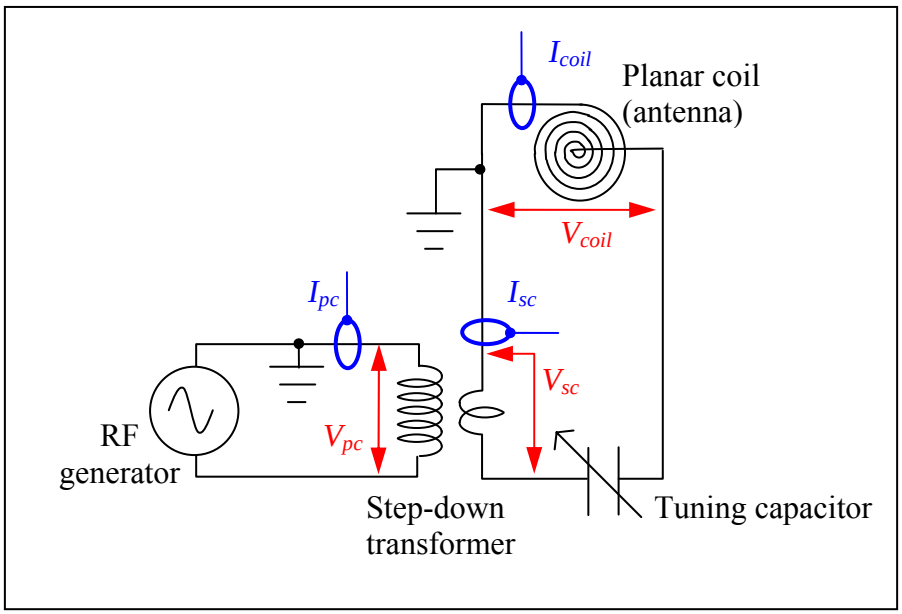

Figure 3.17: Points at which the voltage and current measurements are taken.

[Note: The respective sets of current and voltage measurement of (I_{pc}, V_{pc}), (I_{sc}, V_{sc}) and (I_{coil}, V_{coil}) are measured independently as only one set of voltage and current probes are available. I_{sc} and I_{coil} are actually the same current in the secondary circuit though they were monitored at different points in the circuit for convenience.]

CHAPTER 4 RADIO FREQUENCY BREAKDOWN AND ELECTRICAL PROPERTIES

4.1 RADIO FREQUENCY (RF) BREAKDOWN

The RF breakdown voltage, U_b, (monitored at the powered end of the planar coil) is the highest voltage registered just before the ignition of the discharge. Immediately after ignition, the discharge is sustained at a slightly lower voltage, U_{st}, though the RF power did not change.

The effect of argon pressure on the RF breakdown voltage, U_b at various flowrates of 10, 20, and 30 sccm is shown in Figure 4.1 for the range of argon pressures from 0.01 to 2.1 mbar. The pressure could not be brought to lower values when the flowrate is high. There is slight dependence of U_b on the flowrate, registering higher voltages at higher flowrates. The amplitude of the RF breakdown voltage, $U_b(p\text{-}p)$, varies within the range of 540 V to 3060 V for the pressure range investigated. A minimum U_b is observed at $p \cong 0.1$ mbar. To the right of this minimum, U_b rises slowly with p, increasing from 540 V to 1650 V. At lower pressure side ($p < 0.1$ mbar), U_b increases rapidly with decrease in p.

The variation of the RF breakdown voltage against pressure shows trend similar to Paschen curve for DC breakdown. When compared to the breakdown curves reported in argon capacitively coupled configuration of electrode (stainless steel) gap 2.3 cm by *Lisovskiy et al.* [31], the observed minimum point occurs at slight lower p (compared to

1.4 mbar in Reference [31]) though their breakdown potential $U_{b(peak)}$ is about 6 times lower at 45 V. The turning point reported by *Lisovskiy et al.* is not observed in Figure 4.1. In a later report by the same authors [30], the minimum shifted to higher pressure and breakdown potential when the electrode gap is reduced (0.67 mbar and 70 V at 1.3 cm gap; 4 mbar and 85 V at 0.65 cm gap).

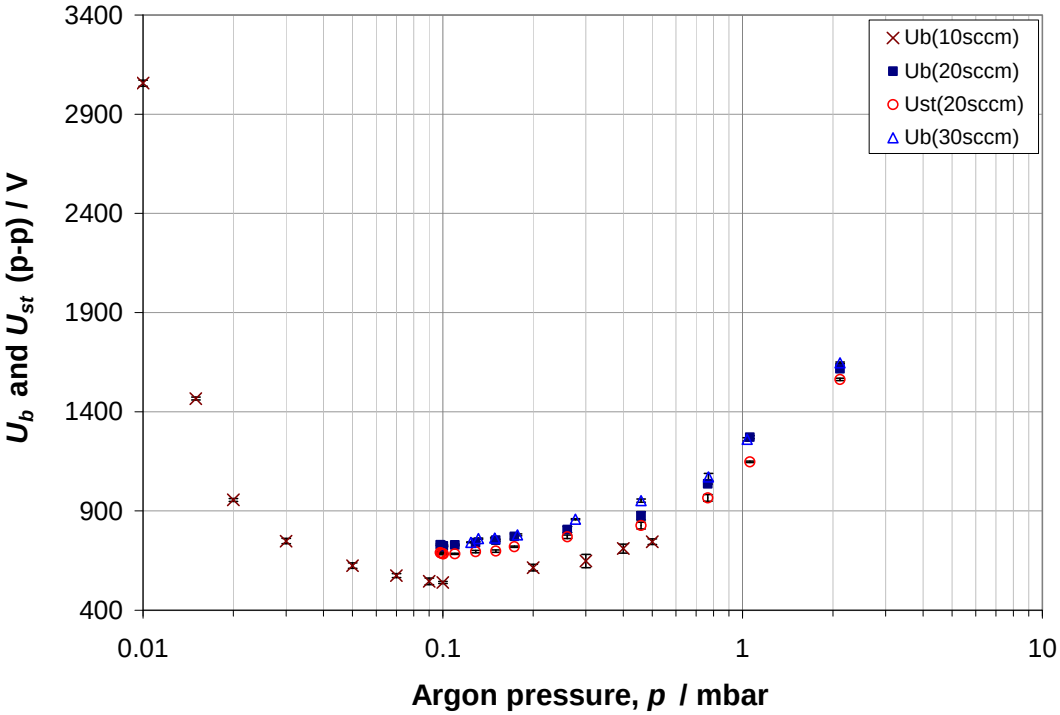

Figure 4.1: Graph of RF breakdown voltage, U_b against argon pressure, p at flowrates 10, 20, and 30 sccm as indicated. The discharge sustaining voltage U_{st} is plotted for 20 sccm for comparison.

In the present inductive discharge setup, the inductive coil is outside the chamber, hence, there is no contribution of electron emission from the electrode surface. Electron multiplication depends on volume ionization. At low RF power, it is commonly believed that the breakdown is initiated by the capacitive coupling due to the electric field across the coil turns caused by large potential drop across them [19]. The

measured breakdown potential U_b is the voltage drop across the powered end (centre) and the grounded end (outermost turn). Assuming the potential to be distributed linearly along the turns of the coil, it is estimated from the geometry of the planar coil that the potential drop across the outmost and its immediate inner adjacent turn is the largest at approximately 30 % of the full U_b. This means the corrected minimum RF breakdown potential is approximately 80 V (peak value) which is close to that reported by *Lisovskiy et al.* [30] when the average gap between adjacent turns is taken to be 0.9 cm. However, the observed minimum pressure is about 10 times lower.

In considering small contribution of the induced electric field from the oscillating magnetic field that penetrates into the chamber, *Burm* [33] showed that the minimum occurs at p = 0.05 to 0.1 mbar corresponding to breakdown magnetic field B_{bd} = 0.1 to 1 mT for drive frequency 10 MHz and coil radius between 2 and 5 cm. The shape of the $B_b - p$ is similar to the $U_b - pd$ curve. Approximating the radius of the planar coil to 2.3 cm (average value of the 6-turn spiral coil), the minimum p is close to that in Figure 4.1 and the estimated induced field is approximated as:

$$E_{ind} = 2\pi fBR$$

$$= 2\pi(13.56\times10^{6}\,\text{Hz})(0.1\times10^{-3}\,\text{T})(0.023\text{m}) \cong 196\,\text{V/m}\,,$$

equivalent to reduced induced field of $E_{ind}/p \cong$ 26 V/cm·torr that can contribute to ionization corresponding to the first Townsend ionization coefficient $\alpha/p \cong$ 0.1 ion pairs/cm·torr [48]. The B value is an approximation from

$$B_z = 6\times\frac{\mu_0 i}{2}\frac{R^2}{(R^2+z^2)^{3/2}} \approx 0.1\ \text{mT}$$

where B_z is the axial field at position just above the quartz surface, z = 2 cm from coil and spiral coil considered as a circular coil having 6 turns of average radius R = 2.3 cm. The coil current at minimum is 1.4 A (peak).

For comparison, the discharge sustaining voltage, U_{st} is plotted for 20 sccm in the breakdown graph of Figure 4.1. U_{st} is slightly lower than the breakdown voltage, U_b. Higher voltage is required to ignite the discharge as sufficient ionization has to be built up to the condition for gas breakdown. Upon ignition, the discharge begins to conduct and the voltage required to sustain it becomes lower.

4.2 *E* AND *H* MODE DISCHARGES

4.2.1 VOLTAGE AND CURRENT IN THE INDUCTION COIL

The dependence of induction coil voltage, V_{coil} and coil current, I_{coil} on the incident RF power at argon pressure 0.13 (± 0.01) mbar at argon flowrate of 40 sccm is shown in Figure 4.2. A mode transition is observed in the electrical characteristics of the induction coil. The *E* to *H* mode transition results in a drop in both coil rms current, I_{coil} and coil rms voltage, V_{coil} at the RF power of 80 to 85 W. When *E* to *H* mode transition occurs, higher plasma luminosity with an increase in the reflected RF power is observed. Even after adjusting the tuning capacitor to match the conjugate reactance (the inductance in the planar coil is lower under *H* mode), the reflected power could not be brought down to zero (Figure 4.3) as the fixed turns ratio of the step-down transformer could not be matched to the higher load resistance [49] in the presence of the *H* mode plasma. This increase in antenna or coil resistance R_a evident in Figure 4.4 which shows the dependence of R_a on the net input RF power for *E* and *H* mode discharges as well as when the plasma is not ignited. The average antenna resistance at

E and *H* modes are 1.12±0.01 Ω and 2.00±0.01 Ω respectively. As the RF power is gradually decreased, the inverse *H* to *E* mode transition occurs at 70 to 65 W accompanied by increase in the coil current and coil voltage. Hence, a small hysteresis region with power width of 20 W is observed.

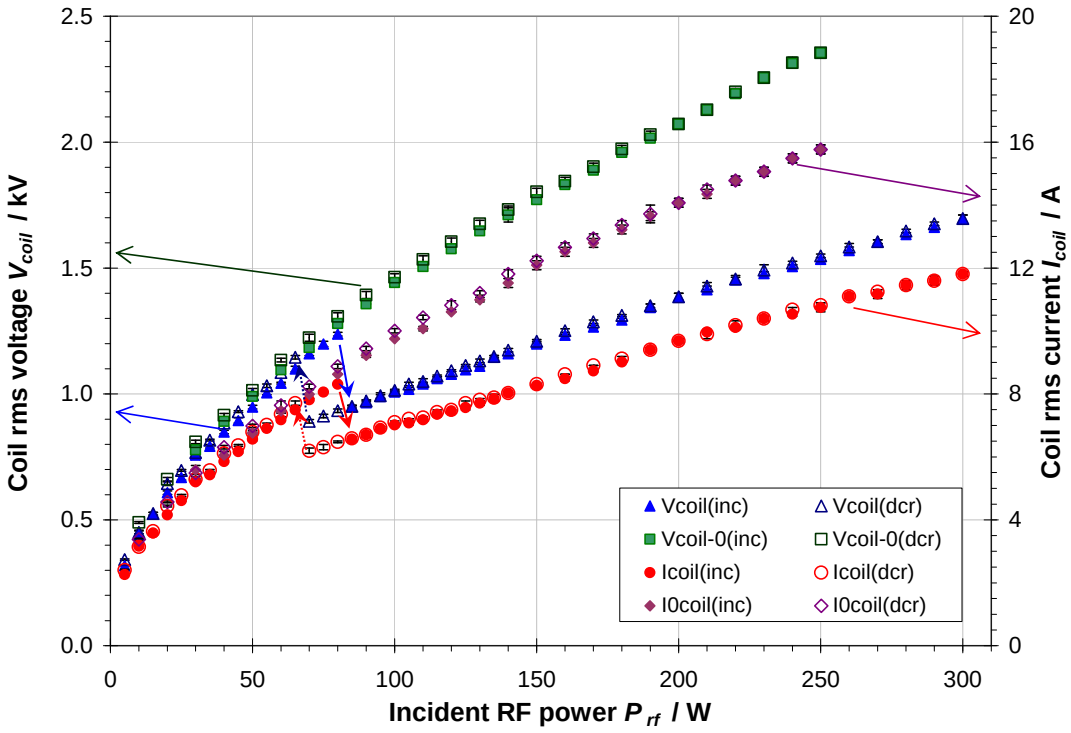

Figure 4.2: Graph of coil rms voltage and coil rms current against incident RF power with Ar plasma at 0.13 mbar, 40 sccm and without the ignition of plasma. (inc) indicates data is measured as RF power is increased slowly and (dcr) curve is obtained when RF power is decreased slowly.

In the absence of plasma at working pressure lower than 10^{-3} mbar in air, no mode transition is observed. The coil rms current and coil rms voltage increases gradually with increasing incident RF power. The antenna resistance R_a is constant at 1.023±0.006 Ω (Figure 4.4). Thus, the reflected power is zero for the whole range of input RF power as the impedance is matched.

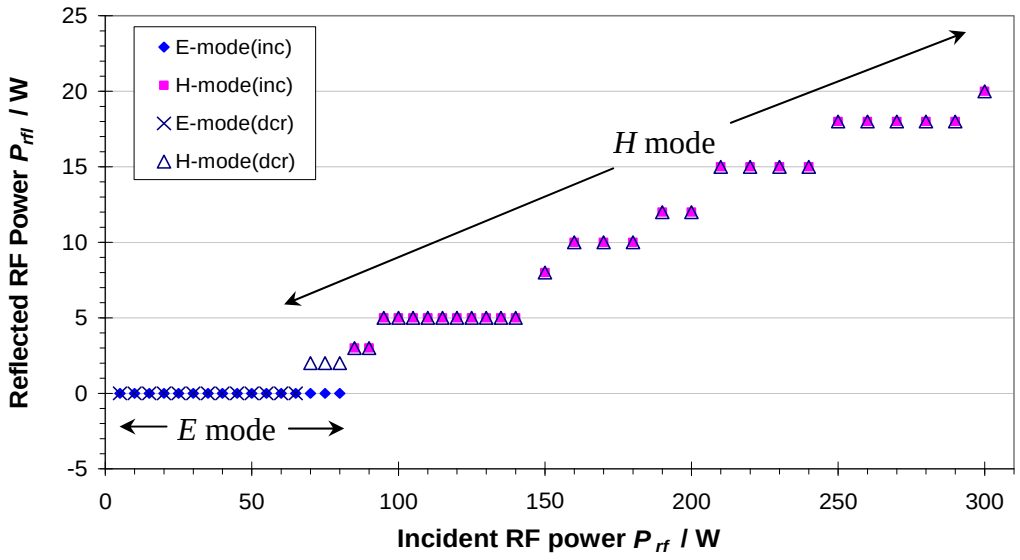

Figure 4.3: Graph of reflected RF power against incident RF power for Ar plasma at 0.13 mbar and 40 sccm. $P_{rfl} = 0$ for E mode and $P_{rfl} > 0$ for H mode.

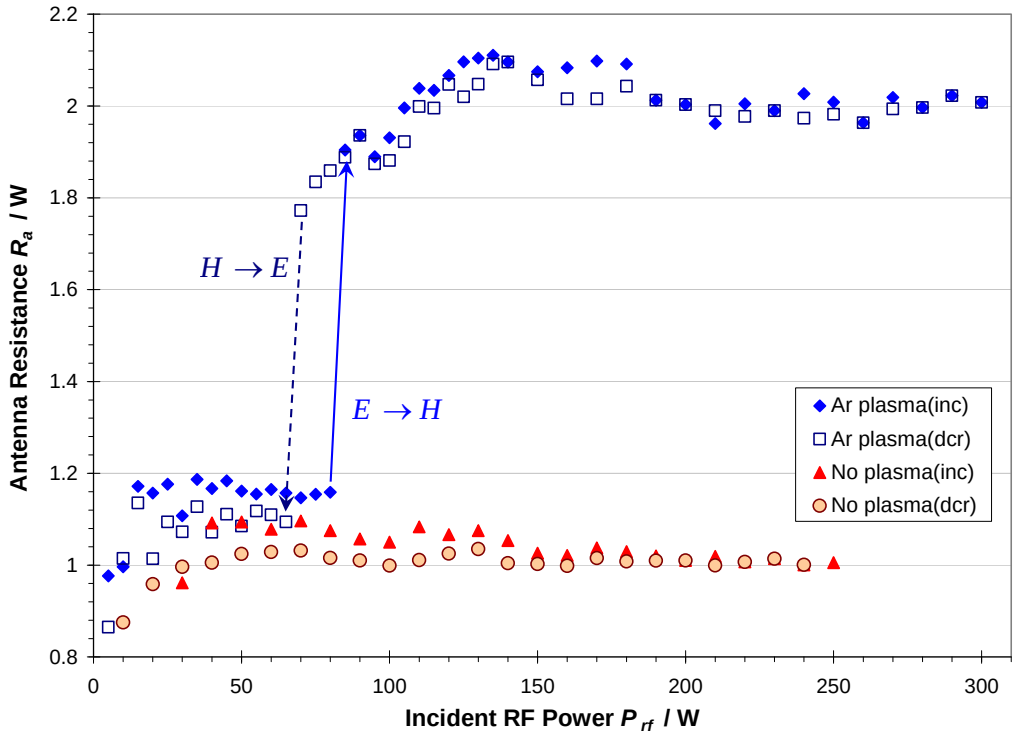

Figure 4.4: Graph of antenna or coil resistance R_a against incident RF power Ar plasma at 0.13 mbar, 40 sccm and without the ignition of plasma. R_a = 1.023±0.006 Ω (no plasma), R_a = 1.12±0.01 Ω (E mode), and R_a = 2.00±0.01 Ω (H mode)

At the best matched condition, the measured capacitance of the tuning capacitor is 77.4-77.8 pF in *E* mode discharge and increases to 79.6-80.1 pF in *H* mode discharge. This indicates a reduction in the inductance of the planar coil for *H* mode discharge as the presence of the large current in the plasma creates a counter effect on the magnetic flux of the planar coil in the transformer model of the RF discharge (the plasma is assumed to be a single turn secondary coil of an air-core transformer whilst the planar coil itself make up the primary) [49].

4.2.2 VOLTAGE AND CURRENT IN THE STEP-DOWN TRANSFORMER OF THE MATCHING NETWORK

Figure 4.5 shows the graph of primary coil rms voltage, V_{pc} and current I_{pc} through the step-down transformer in the impedance matching network against incident RF power, P_{rf}. It is found that both V_{pc} and I_{pc} exhibit hysteresis phenomenon where the mode transitions occur. *E* to *H* mode transition starts at incident RF power, P_{rf} = 70 W, while *H* to *E* mode transition at 55 W. These values differ from those in the earlier section as both were measured in different discharges though operated under the same conditions. The width of hysteresis region is 20 W. A voltage jump of (22-23) V occurs during the *E* to *H* mode transition accompanied by current drop of 0.2 A. The reverse is true for the *H* to *E* mode transition. Within the incident RF power range of 5 to 300 W, the measured V_{pc} ranges from 20 V to 182 V and the current I_{pc} is from 0.3 A to 1.6 A.

The graph of secondary coil rms voltage, V_{sc} and current, I_{sc} at the step-down transformer in impedance matching network against incident RF power is shown in Figure 4.6. The V_{sc} and I_{sc} exhibit the same trend as that of the primary coil except that *E* to *H* transition results in sudden drop in both V_{sc} and I_{sc} similar to that observed in the planar coil. Likewise, *H* to *E* transition is exhibited by sudden jump in both V_{sc} and I_{sc}.

For incident RF power from 5 W to 300 W, V_{sc} and I_{sc} vary from 50 V to 550 V and 1.8 A to 10.2 A respectively.

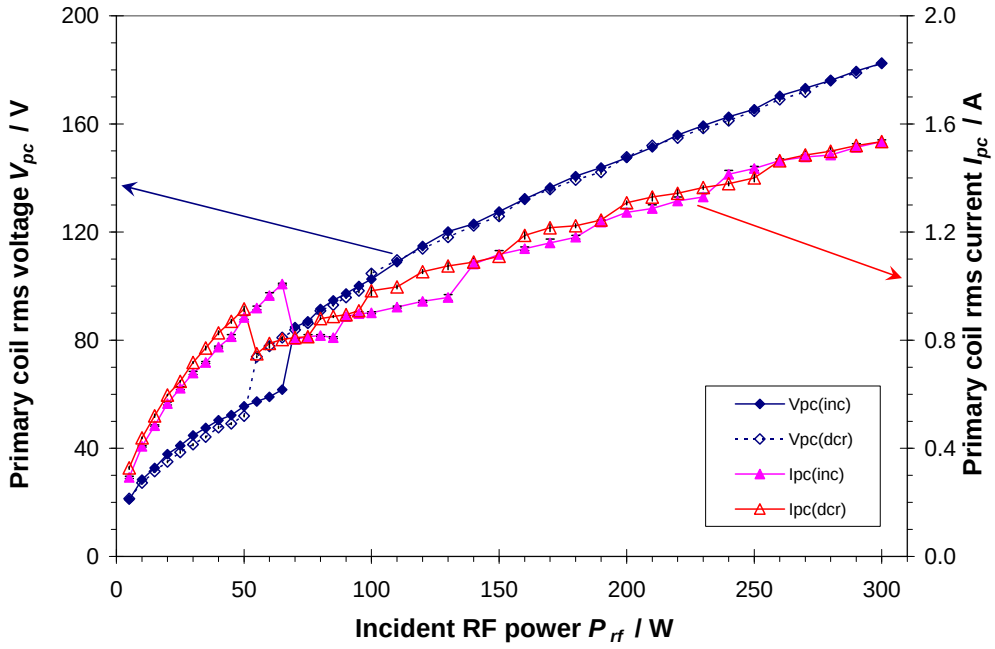

Figure 4.5: Graph of primary coil rms voltage and coil rms current against incident RF power at argon pressure 0.13 mbar and flowrate 40 sccm.

Figure 4.7 shows the resistance at the primary side of the step-down transformer averages to 61 Ω for incident RF power from 5 W to 50 W when the discharge is in *E* mode. This value is close to the output resistance of the RF generator of 50 Ω. At around 60 W onwards for *H* mode, the resistance at the primary side almost doubles (average value = 114 Ω) and generally increases slowly as the power is increased. The matching network can no longer match the increased load resistance (Figure 4.4) to the source resistance and the reflected RF power (though small) increases.

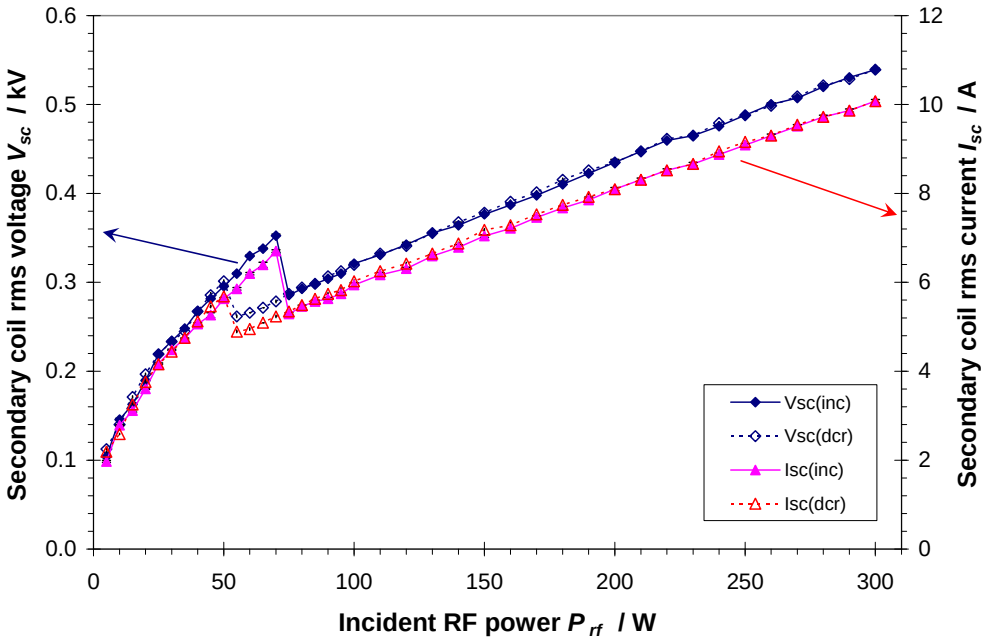

Figure 4.6: Graph of secondary coil rms voltage and coil rms current against incident RF power at argon pressure 0.13 mbar and flowrate 40 sccm.

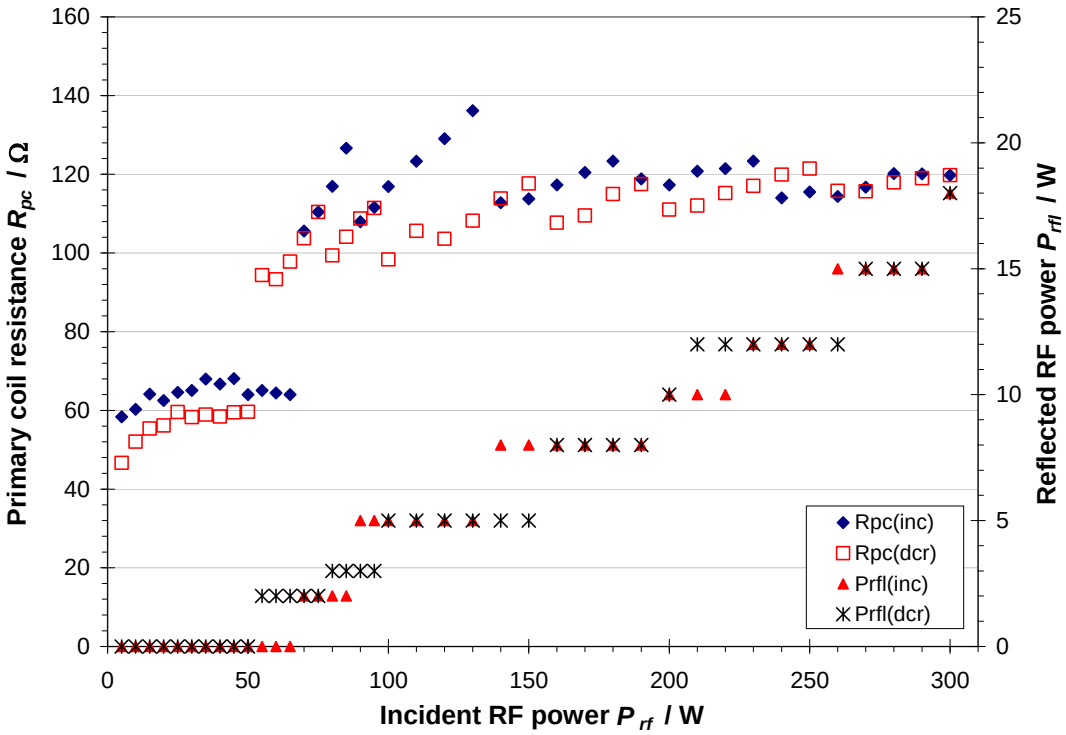

Figure 4.7: Graph of primary coil resistance of the transformer and the reflected RF power against incident RF power at argon pressure of 0.13 mbar and flowrate 40 sccm. R_{pc} = 61±1 Ω (*E* mode), and R_{pc} = 114±1 Ω (*H* mode).

Similar dependence on the discharge mode is observed in the resistance at the secondary side of the transformer shown in Figure 4.8. However, the resistance in the secondary coil is approximately 41 times smaller than that of the primary side and about 1.3 times larger than that of the antenna coil. It is deduced that the effective turns ratio of the transformer a is $\sqrt{41} \cong 6.4$.

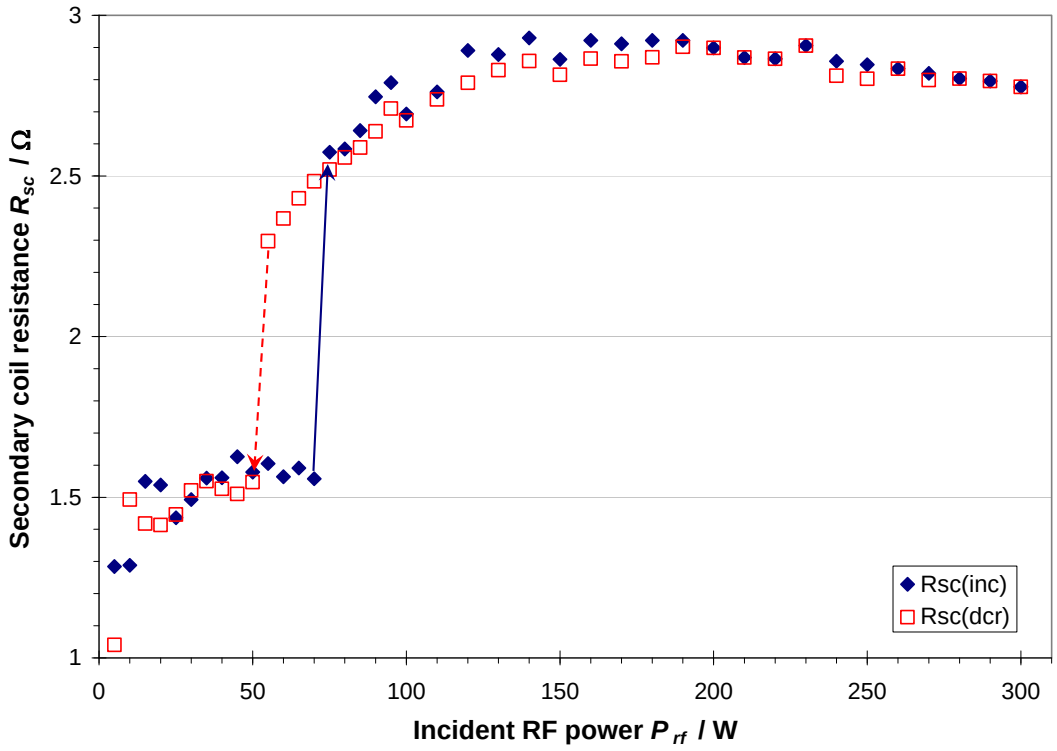

Figure 4.8: Graph of secondary coil resistance of the transformer against incident RF power at argon pressure of 0.13 mbar and flowrate 40 sccm. R_{sc} = 1.49±0.03 Ω (*E* mode), and R_{sc} = 2.77±0.02 Ω (*H* mode).

4.3 POWER TRANSFER EFFICIENCY

The power transfer efficiency, ξ plotted against the incident RF power is shown in Figure 4.9. The *H* mode discharge is supported by ξ of two orders of magnitude larger when compared to that of the *E* mode discharge. This agrees with the trend of the power transfer efficiency against electron density plot in Figure 4.10. The power transfer efficiency, ξ at *E* mode incurs large errors due to the limited resolution of the analog scale for the input and reflected RF power display. Hence, no conclusive deduction can be made in the low electron density region though *Suzuki et al* [34] showed ξ to be inversely proportional to n_e. At the high density region (*H* mode), ξ increases slowly with n_e similar to the trend reported by *Suzuki et al*. In the mid-range of n_e of about 0.2×10^{17} to 2×10^{17} m^{-3}, there are no experimental data points due to the mode transition.

The mode transition analysis is carried out based on the consideration of the power balance and electron density dependent power transfer efficiency $\xi(n_e)$, as outlined in Reference [34]. The power balance requires the RF power transferred to the plasma, P_{tr} given by following equation (see Equation 2.4a):

$$P_{tr} = \xi(n_e)\, P_{net}. \tag{4.1}$$

It is equated to the power dissipated in the plasma, P_{dis} which is expressed as follows:

$$P_{dis} = \eta n_e. \tag{4.2}$$

The constant of proportionality is given as:

$$\eta = e u_B \varepsilon_T A_s, \tag{4.3}$$

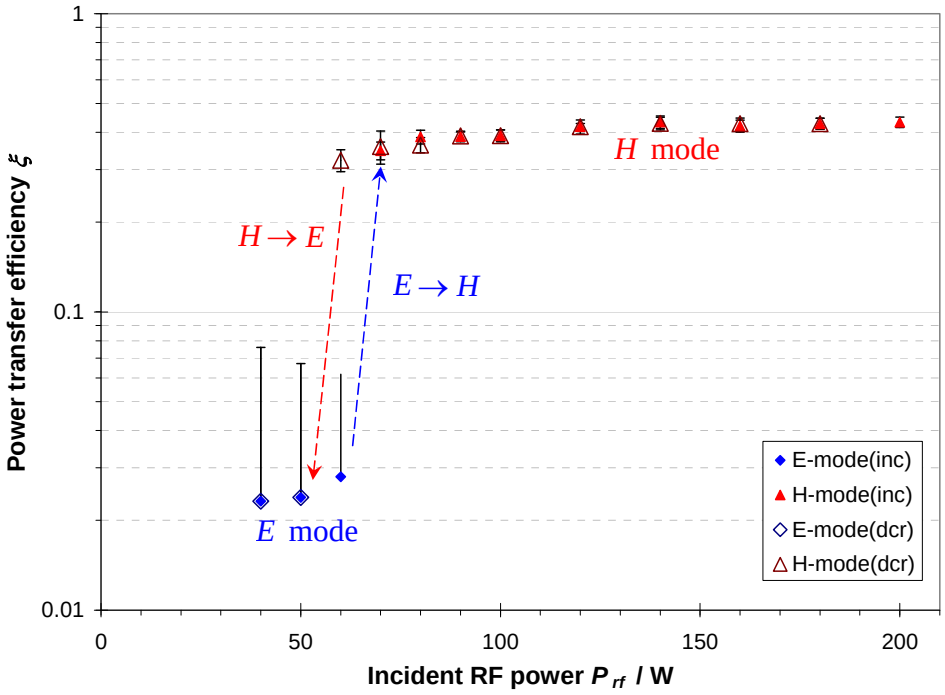

Figure 4.9: Graph of power transfer efficiency ξ against incident RF power in a 13.56 MHz RF argon discharge at 0.1 mbar and flowrate 30 sccm.

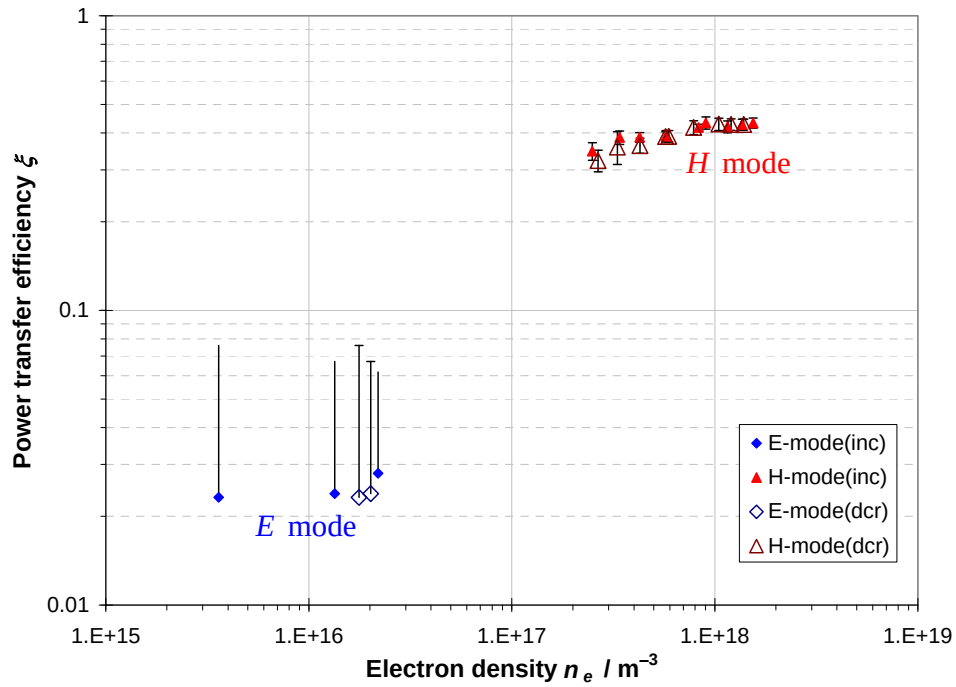

Figure 4.10: Graph of power transfer efficiency ξ against electron density n_e in a 13.56 MHz RF argon discharge at 0.1 mbar and flowrate 30 sccm.

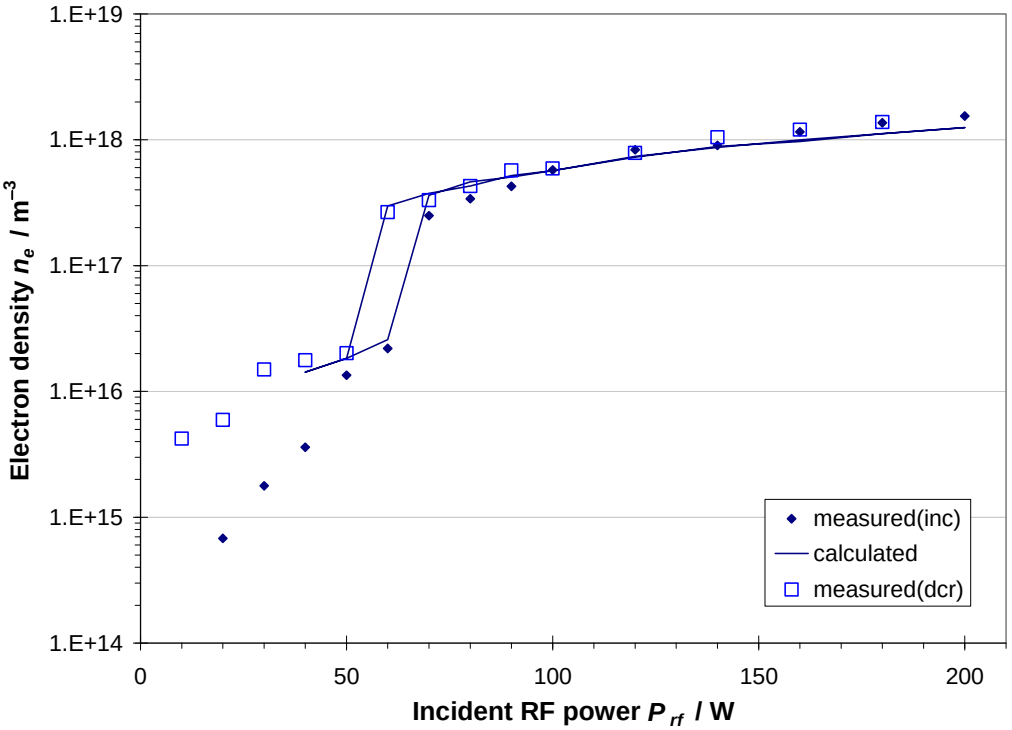

Figure 4.11: Graph of electron density n_e against incident RF power in a 13.56 MHz RF argon discharge at 0.1 mbar and flowrate 30 sccm.

where u_B is the Bohm velocity, ε_T is the total energy lost per ion lost from the system and A_S is the surface area. Equating equations (4.1) and (4.2), the constant of proportionality is estimated as $(6.5\pm0.3)\times10^{-17}$ W/m^{-3}. This value is about one order of magnitude lower than that reported by *Suzuki et al.* [34] though the power transfer efficiency is of comparable magnitude. This implies that the present system has less loss of power transferred to the plasma, hence resulting in higher plasma density (about one order of magnitude higher). This is likely due to the 6 turns spiral antenna coil and the absence of a Faraday shield as compared to the single turn and presence of Faraday shield setup in Reference [34]. In fact, *Suzuki et al.* have also shown that a 3-turn spiral antenna and absence of Faraday shield between the antenna and the reactor chamber produces higher electron density. Using the measured power transfer efficiency, this

constant is used to fit n_e to the measured values and is shown in the $n_e - P_{rf}$ plot of Figure 4.11. The solid line shows reasonable fit.

4.4 MODE TRANSITION

The switchover power for the mode transition is presented in Figure 4.12. The switchover power for *E* to *H* mode transition is higher compared to that of the reverse *H* to *E* mode transition, and hysteresis phenomenon is observed. Thus, there exists a range of incident RF power which may support both modes of operation depending on the previous history of the system [50]. The switchover power for *E* to *H* mode transition drops a little at low pressure and starts to increase with pressure from 0.14 mbar to 1.05 mbar. On the other hand, the switchover power for *H* to *E* mode transition decreases rapidly at low pressure up to about 0.14 mbar and as pressure increases further, it is almost constant. Correspondingly, the power range where hysteresis occurs is small showing a minimum at 0.1 mbar at the low pressure end, growing linearly as the pressure increases beyond 0.1 mbar.

In Figure 4.13, the dependence of switchover coil rms voltage, V_{rms} for *E* to *H* and *H* to *E* mode transitions on pressure is similar to that of the switchover power. Again, hysteresis is manifested in the difference of V_{rms} for the two types of transition, and this hysteresis range gets larger as the pressure increases. Similar observations are obtained for the coil rms current, I_{rms}, as shown in Figure 4.14. It is clear that there is a minimum current to start the inductive mode (initiating current), and a minimum current to sustain the inductive mode (sustaining current).

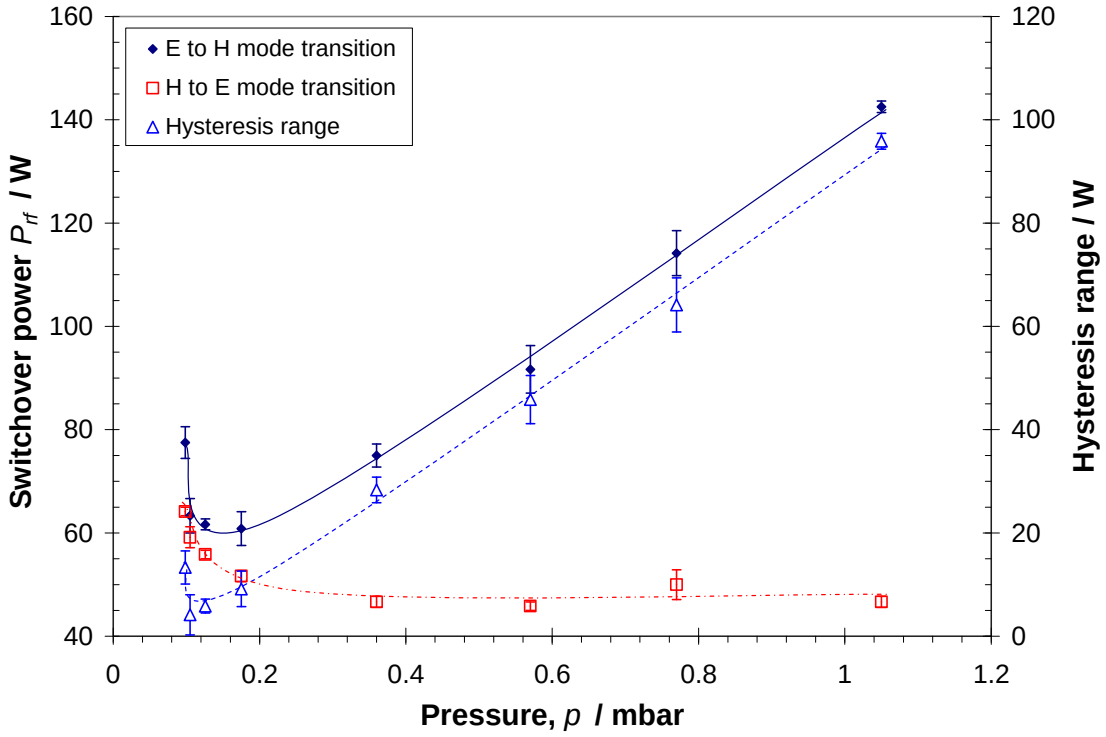

Figure 4.12: Graph of switchover power against pressure for *E* to *H* and *H* to *E* mode transitions. Argon flowrate = 30±5 sccm.

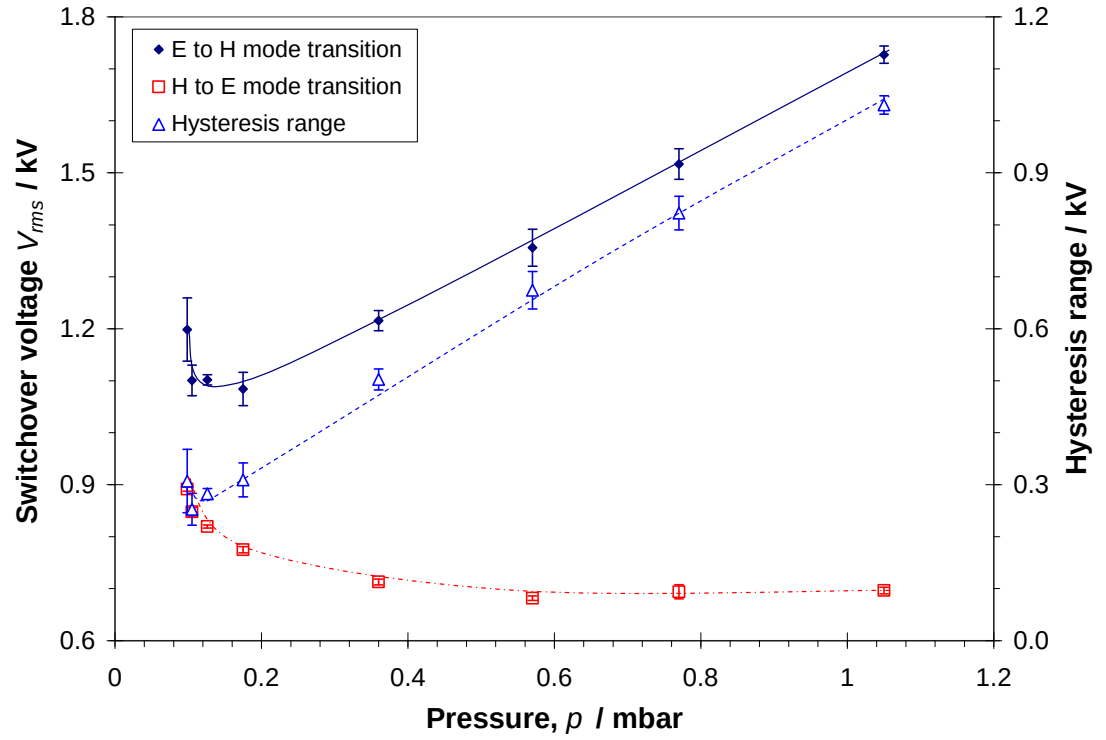

Figure 4.13: Graph of switchover planar coil rms voltage V_{rms} against pressure for *E* to *H* and *H* to *E* mode transitions. Argon flowrate = 30±5 sccm.

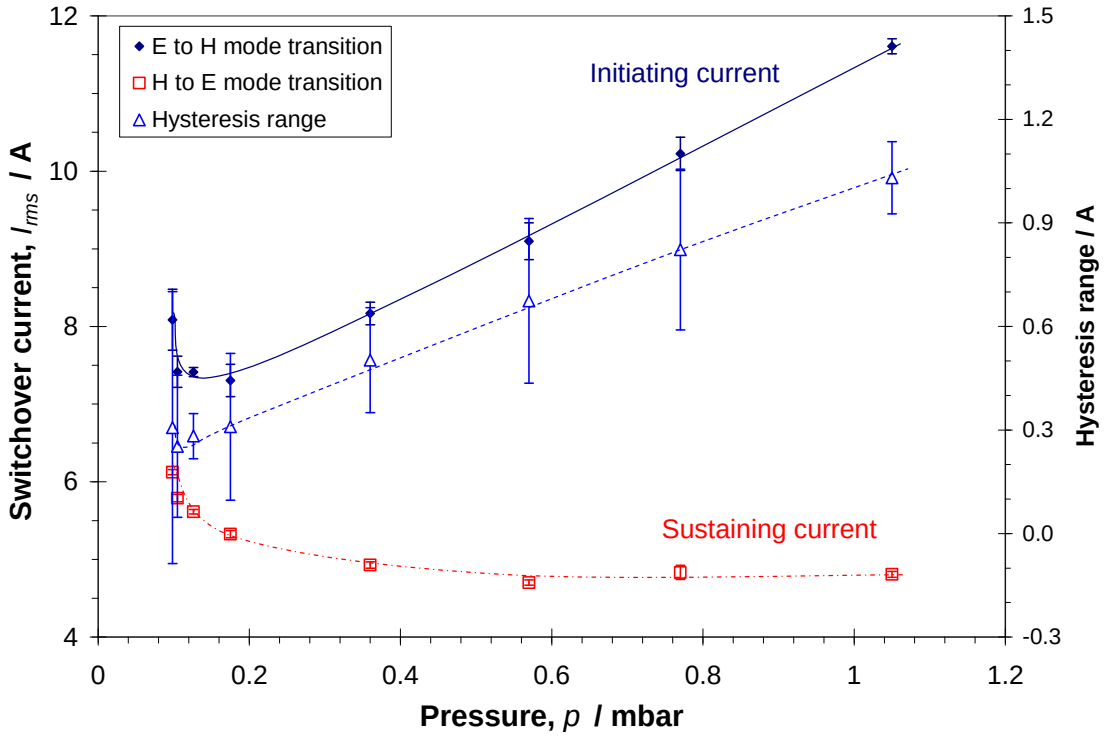

Figure 4.14: Graph of switchover planar coil rms current I_{rms} against pressure for E to H and H to E mode transitions. Argon flowrate = 30±5 sccm.

Hysteresis in the mode transition gives the implication of the existence of more than one stable equilibrium point in the electron power balance equation describing the RF discharge at a particular antenna coil current. This is related to non-linearities in the electron power balance equation that requires the power absorbed by the electrons from the driven antenna coil (P_{tr}) to be balanced with the power dissipated (P_{dis}) in the plasma through collisions of electrons with other species. The non-linearities would include circuit related non-linearities that affects P_{tr} and non-linearities in the plasma itself which affects P_{dis} [50]. In a real inductive discharge, some of the RF power is always deposited capacitively resulting in a voltage across the induction coil that will drive a capacitive current in the plasma. This inductive discharge can then be represented by a lumped element model, in which an inductive current branch flowing

through the antenna and a capacitive current branch (inclusive of coil-to-dielectric window and sheath capacitances, resistances representing ohmic heating and heating of ions as they fall through a dc sheath potential) exist in parallel. The division of current between the inductive and capacitive branches can give rise to the circuit related non-linearities as the values of the lumped circuit elements are nonlinear functions of plasma density as well as sheath voltage [51].

Non-linearities in the plasma itself can be contributed by presence of Coulomb collisions between electrons and multi-step ionization via intermediate excited states of argon. These processes were not taken into account in the consideration of volume ionization source for the power balance equation [51], and the electron energy required to sustain an electron-ion pair during its lifetime was assumed to be independent of the plasma density. However, the presence of the two additional collisional processes leads to dependence of total energy required for an electron-ion pair production on electron density and, hence, can increase the proportion of power absorbed by the electrons for ionization. Thus, this non-linear behaviour can contribute significantly to hysteresis.

CHAPTER 5 PLASMA CHARACTERISTICS

Plasma characteristics measured using the Langmuir probe at various RF power is presented in this chapter. The plasma characteristics include the electron temperature T_e, electron density n_e, plasma potential V_s, and electron energy distribution function *EEDF*. Measurements made using Langmuir probes of different tip diameters are also carried and compared. Radial distribution of the plasma parameters is also measured.

5.1 MEASUREMENT AT VARIOUS INCIDENT RF POWER

The dependence of plasma characteristics on RF power input has been studied. The probe measurement was carried out at a constant argon flowrate and pressure of 20 sccm and 0.10 (± 0.01) mbar. The RF power input was gradually increased from 0 W to 200 W in steps of 10 W for the range of (0 – 100) W and 20 W in the range of (100 – 200) W, after which, it was slowly decreased until the plasma extinguishes. As the power increases from 0 W, the plasma is ignited at about 10 W. The glow stays close to the dielectric window and it is not bright. Its luminosity or brightness increases gradually with power until approximately 80 W. In this range of incident RF power, the plasma is said to be at *E* mode regime. A sudden rise in the luminosity occurs when the RF power increases from 80 W to 85 W indicating a mode transition from *E* mode to *H* mode. This brightness grows as the power is further increased up to 200 W. On decreasing the power, the reverse *H* to *E* mode jump occurs at 75 W to 70 W, resulting

in a hysteresis region of 15 W. The mode transition is exhibited in the plasma characteristics as shown in Figures 5.1, 5.3, and 5.6.

5.1.1 ELECTRON TEMPERATURE

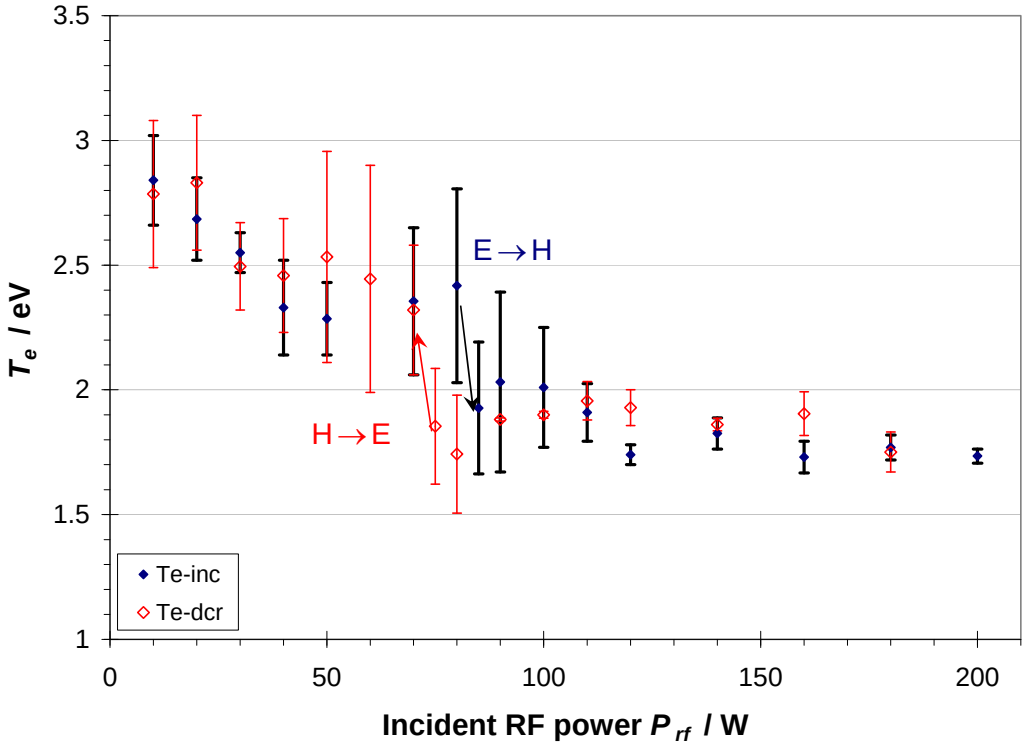

Figure 5.1: Electron temperature against incident RF power at argon pressure of 0.10±0.01 mbar and flowrate of 20 sccm.

It can be seen from Figure 5.1 that the value of electron temperature T_e generally falls with increasing incident RF power P_{rf}, registering steeper fall at *E* mode. The value of T_e varies within the range of 2.3 eV to 2.8 eV for the *E* mode discharge and in the *H* mode, it varies from 1.7 eV to 2.0 eV. Clearly *E* mode discharge is sustained at higher T_e compared to the *H* mode. This is due to the much larger electron density (Figure 5.3) in *H* mode discharge, thus, 'thermalizing' the plasma. The range and trend are consistent with those reported in similar planar ICP discharge by *Mahoney et al.* [36]

and *Godyak et al.* [44]. The fall of T_e with increasing power is a result of two-step ionization via atomic excited states in plasma which is collision dominated (high pressure) and controlled by ambipolar diffusion [44].

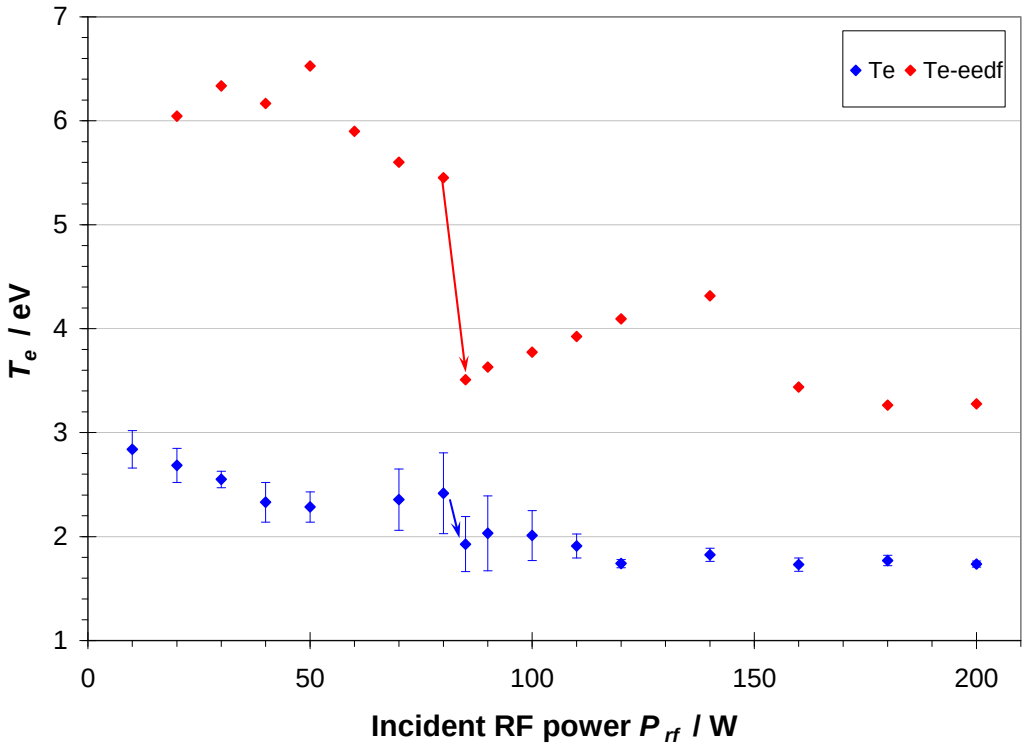

Figure 5.2: Comparing the electron temperatures deduced through (i) gradient of ln(I_e)-V_p plot and (ii) *EEDF*.

The effective electron temperature T_{eff} deduced though integration of the *EEDF* through Eq.(2.19) is shown in Figure 5.2 and is compared to those in Figure 5.1. These T_{eff} are two times higher than T_e deduced from slope of ln(I_e)-V_p curves. Deduction of T_{eff} incurred error as the shape of the *EEDF* is flattened and the peak pushed to high energy due to the large probe circuit resistance R_C. This will be discussed in Sections 5.2.2 and 5.2.5.

5.1.2 ELECTRON DENSITY

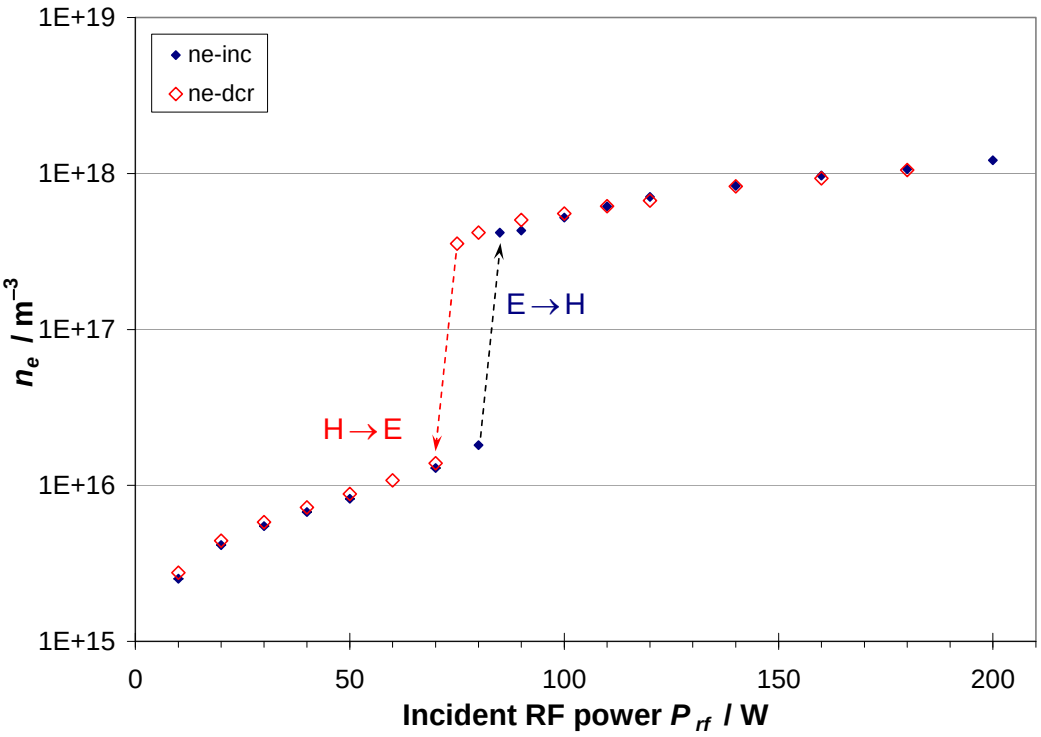

Figure 5.3: Semi-logarithmic plot of the electron density n_e against incident RF power at argon pressure of 0.10±0.01 mbar and flowrate of 20 sccm.

The variation of electron density with RF power is shown in Figures 5.3 and 5.4. As the power is increased, the electron density (n_e) increases. Especially at the mode transition (more obvious in Figure 5.3), it increases by more than one order of magnitude. The *E* mode discharge is characterized at lower n_e ranging from (2.5 – 18.1) $\times 10^{15}$ m^{-3} while the *H* mode discharge at higher n_e ranging from (3.6 – 12.2) $\times 10^{17}$ m^{-3}. Low RF power leads to lower degree of ionization, resulting in a lower overall density. The increase of n_e is considerably steeper by at least one order of magnitude for the *H* mode discharge compared to that for the *E* mode discharge (Figure 5.4).

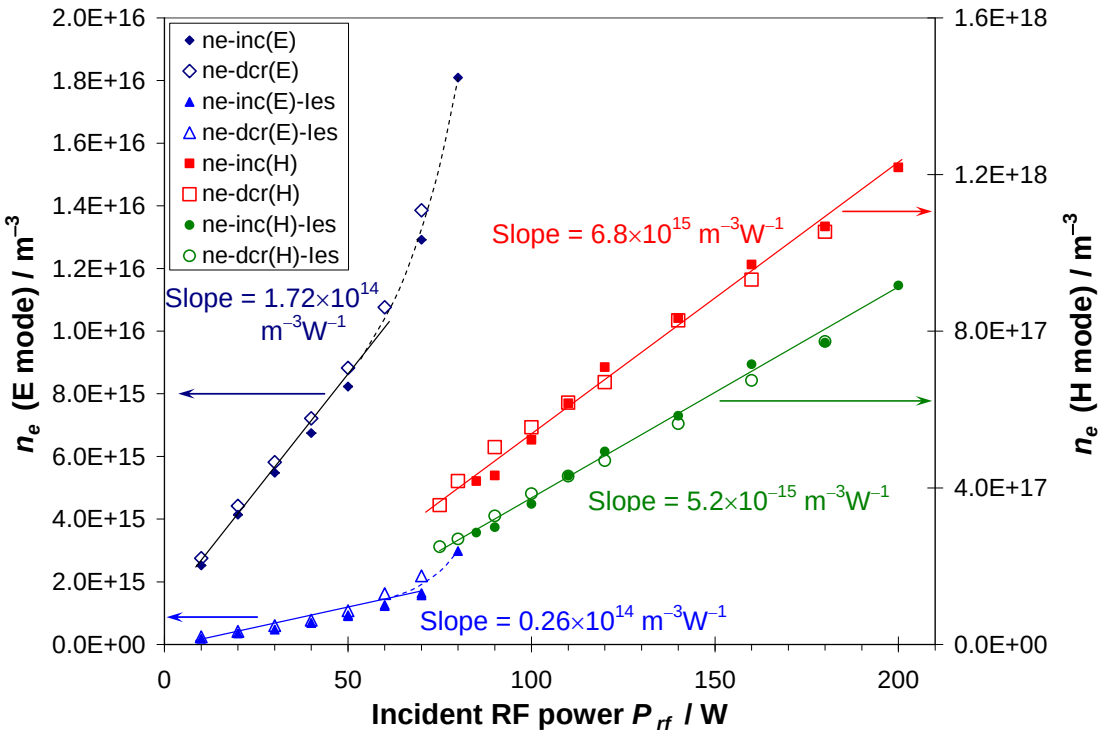

Figure 5.4: Linear plot of the electron density n_e against incident RF power at argon pressure of 0.10±0.01 mbar and flowrate of 20 sccm. 'inc' denotes data obtained when P_{rf} was increasing, and 'dcr' when P_{rf} was decreasing. 'Ies' denotes n_e calculated using the electron saturation current I_{es} through Eq.(2.5). Otherwise, n_e is deduced from the extrapolated ion saturation current I_{is} at floating potential V_f through Eq.(2.11).

Figure 5.4 shows discrepancy in the electron density n_e deduced from electron and ion saturation parts of the probe characteristic. The discrepancy is larger for *E* mode, where n_e deduced from electron saturation current (I_{es}) is 9 times smaller that n_e deduced from ion saturation current (I_{is}). In the *H* mode, the discrepancy is less with n_e deduced from I_{es} being 1.4 times smaller than n_e from I_{is}. This discrepancy may be due to the presence of capacitive coupling that arises from the large potential drop between adjacent turns of the coil which was not shielded. This capacitive coupling can cause ions to attain high energy distorting the *I-V* curve near the region of electron saturation current, results in lowering I_{es}.

Godyak et al. [44] pointed out that probe circuit resistance R_c can also distort the shape of the *I-V* curve near the plasma potential, where I_{es} is deduced. This probe circuit resistance R_c includes the probe driver resistance, resistance of the probe wire, contact resistance, current sensing resistance, resistance of the RF filter, sheath resistance near the chamber wall, and surface resistance of the chamber; of which the last two are unknown and non-linear at times. The authors suggested making R_c to be in the range of few mΩ to fractions of an ohm. However, especially at *E* mode the probe current is very low and a 1 kΩ current sensing resistor has been used in order to obtain readable voltage drop. Thus, the electron density n_e deduced from the ion saturation current I_{is} would be more suitable or accurate as advocated by *Chen* [39].

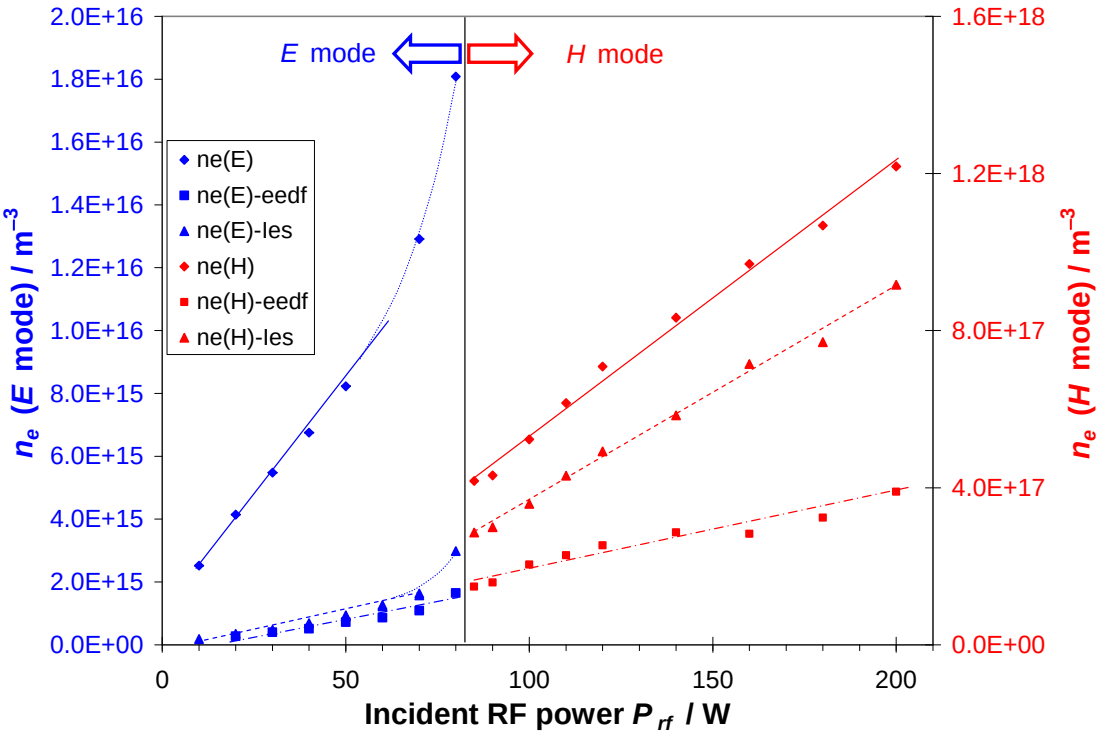

Figure 5.5: Comparing the electron densities deduced from (i) I_{is}, (ii) I_{es}, and (iii) *EEDF*.

The distortion is also evident when the electron density n_e deduced from I_{is} is compared to that estimated by integrating the *EEDF* curve. n_e deduced from *EEDF* shown in Figure 5.5 is approximately one order of magnitude lower in both *E* and *H* modes.

5.1.3 PLASMA POTENTIAL

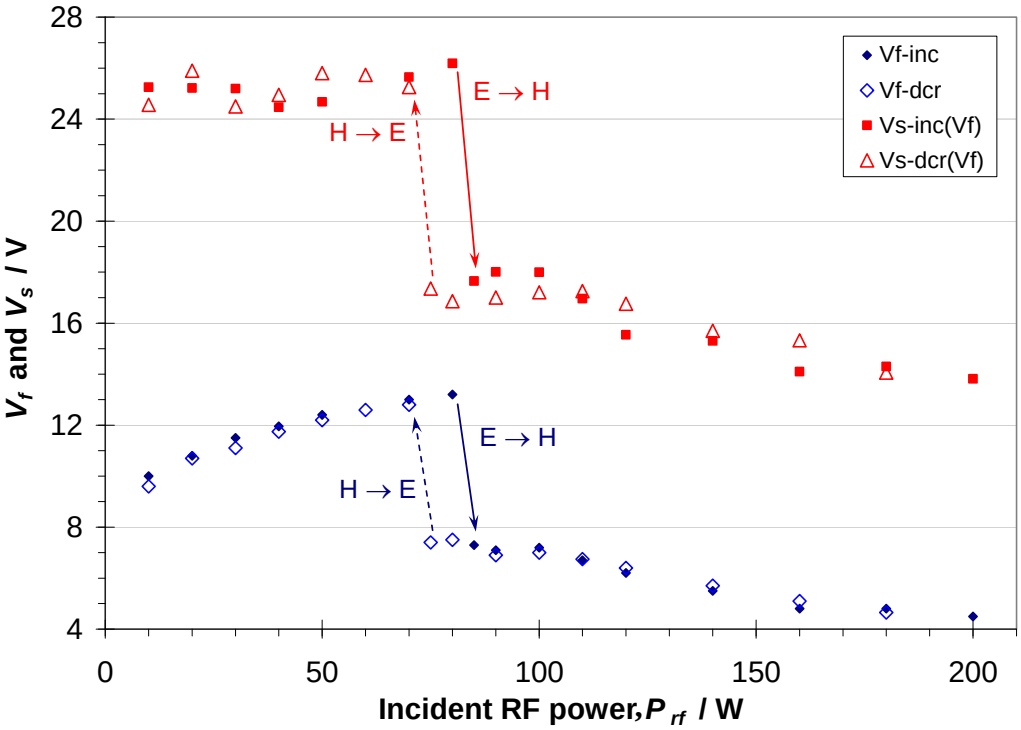

Figure 5.6: Plot of the plasma potential V_s and floating potential V_f against incident RF power at argon pressure of 0.10±0.01 mbar and flowrate of 20 sccm. 'V_f' denotes V_s is deduced from V_f through equation (2.16).

For the *E* mode discharge shown in Figure 5.6, the plasma potential (V_s) is large at approximately 25 V – 26 V and increases very little as the incident RF power (P_{rf}) is increased. On the other hand, the *H* mode discharge exhibited lower V_s of about 18 V near mode transition and then decreases with the increasing of P_{rf} to 14 V at 200 W. The $E \rightarrow H$ mode transition is characterized by a drop in V_s, whereas $H \rightarrow E$ mode transition

by a rise in V_s. In the *E* mode, the dominant heating mechanism is stochastic heating by the capacitive power coupling between electrostatic field and electrons. This heating produces fast energetic electrons and these electrons increase the plasma potential V_s. The sudden change in n_e during mode transition implies an entire change in the power coupling [19].

The probe tip is about 4.2 cm from the quartz window and it is completely immersed in the plasma during the *H* mode discharge which extends well into the space of the chamber. However, the probe is at the edge of the plasma during the *E* mode discharge which forms a disc-like glow close to the quartz window. The field at the edge is higher, thus V_s is expected to be higher.

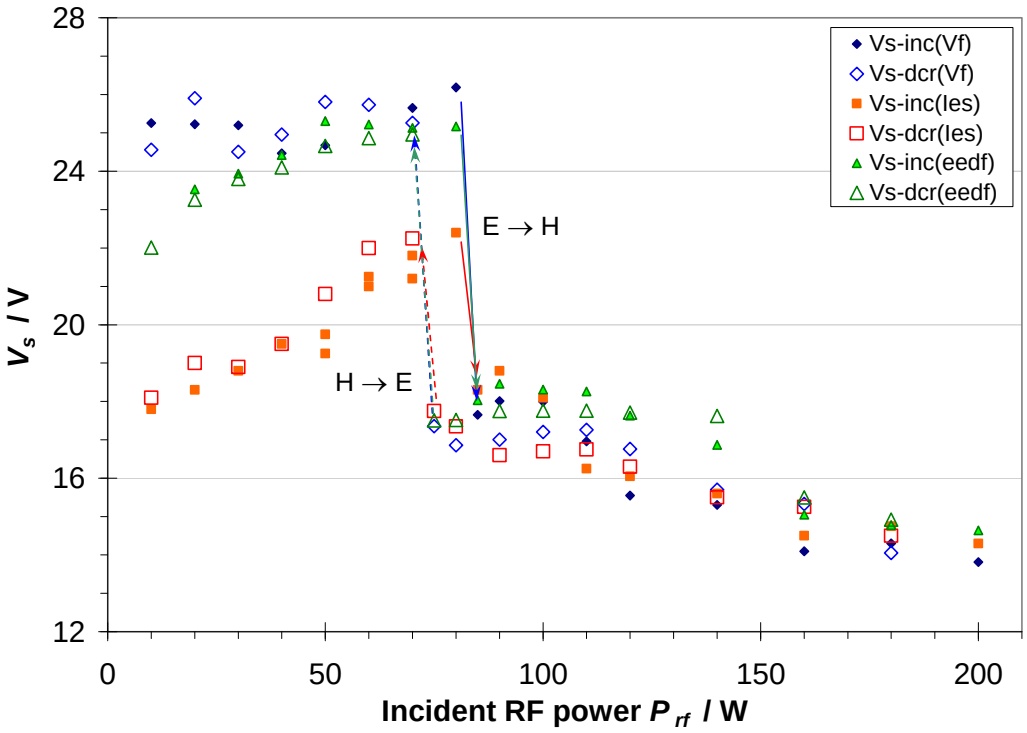

Figure 5.7: Plot of the plasma potential V_s against incident RF power at argon pressure of 0.10±0.01 mbar and flowrate of 20 sccm. 'Vf' denotes V_s deduced from V_f through Eq.(2.16), 'Ies' denotes V_s deduced from point of intersection between the extrapolated linear lines of the electron retardation and saturation regions in the ln(I_e)-V_p plot, and 'eedf' denotes V_s deduced from zero crossing in the second derivative d^2I_e/dV_p^2-V_p curve.

As the curvature between the electron retardation and saturation regions is not obvious in the *I-V* curve for *E* mode, the value of V_s deduced from the point of intersection between the extrapolated linear lines of the electron retardation and saturation regions in the $\ln(I_e)$-V_p plot (Method I) is inaccurate and is shown in Figure 5.7 to be much lower by 30 % to 12 % compared to those deduced from floating potential V_f (Method II). Plasma potentials deduced from zero crossing in the second derivative plot (Method III) is closer to those deduced from V_f, except at low RF power. As discussed in Section 5.2.2, the large circuit resistance R_c used in *E* mode introduces distortion in the probe characteristic curve especially near the plasma potential. Thus, deduction methods I and III would incur large errors.

For the *H* mode, the values of V_s deduced through the three methods are quite close. Here the circuit resistance R_c is at least 100 times smaller and the 'knee' at the plasma potential is distinctive.

5.1.4 FLOATING POTENTIAL

Figure 5.6 also shows the variation of the floating potential V_f with RF power. During the *E* mode discharge, the floating potential V_f shows larger value, increasing from 9.6 V to 13.2 V as P_{rf} increases. Conversely, the *H* mode discharge exhibits lower V_f and decreases from 7.5 V to 4.5 V with increasing P_{rf}. The mode transitions are similarly characterized by a drop in V_f for $E \rightarrow H$ transition and a rise in V_f for $H \rightarrow E$ transition.

5.1.5 ELECTRON ENERGY PROBABILITY FUNCTION (*EEPF*)

The constant terms in Eq. (2.17) can be represented by *C'* and the equation is rewritten as:

$$\left[Fe(\varepsilon)\right]_{\varepsilon=eV} = C'\sqrt{V}\frac{d^2 I_e}{dV_p^2} = C'(EEPF), \qquad (5.1)$$

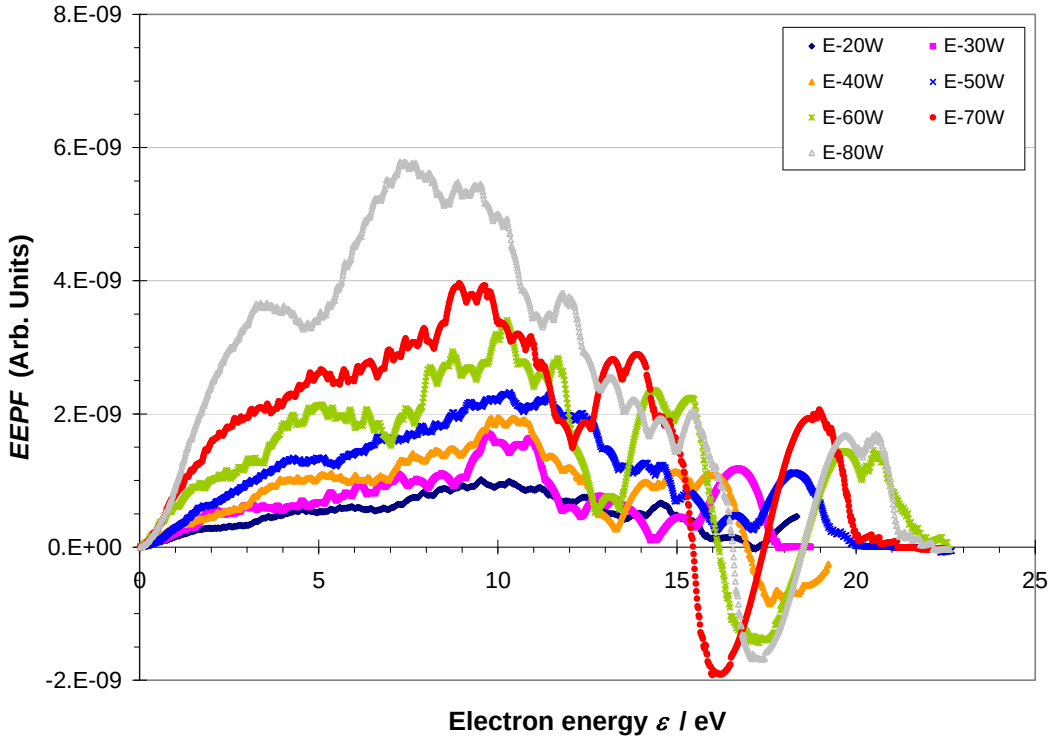

Figure 5.8(a): *EEPF* against electron energy ε at various RF powers in *E* mode for fixed argon pressure of 0.10±0.01 mbar and flowrate 20 sccm.

where *EEPF* is the Electron Energy Probability Function and can represent the energy distribution function of the electrons. The *EEPF* plotted against the electron energy $\varepsilon = V_s - V_p$ [in eV] for the same conditions as those in Sections 5.2.1 to 5.2.3 are shown in Figures 5.8(a) and 5.9 for the *E* and *H* modes respectively. As similar trends are

observed for both situations where RF power P_{rf} is increasing and decreasing, only the those for increasing P_{rf} are shown.

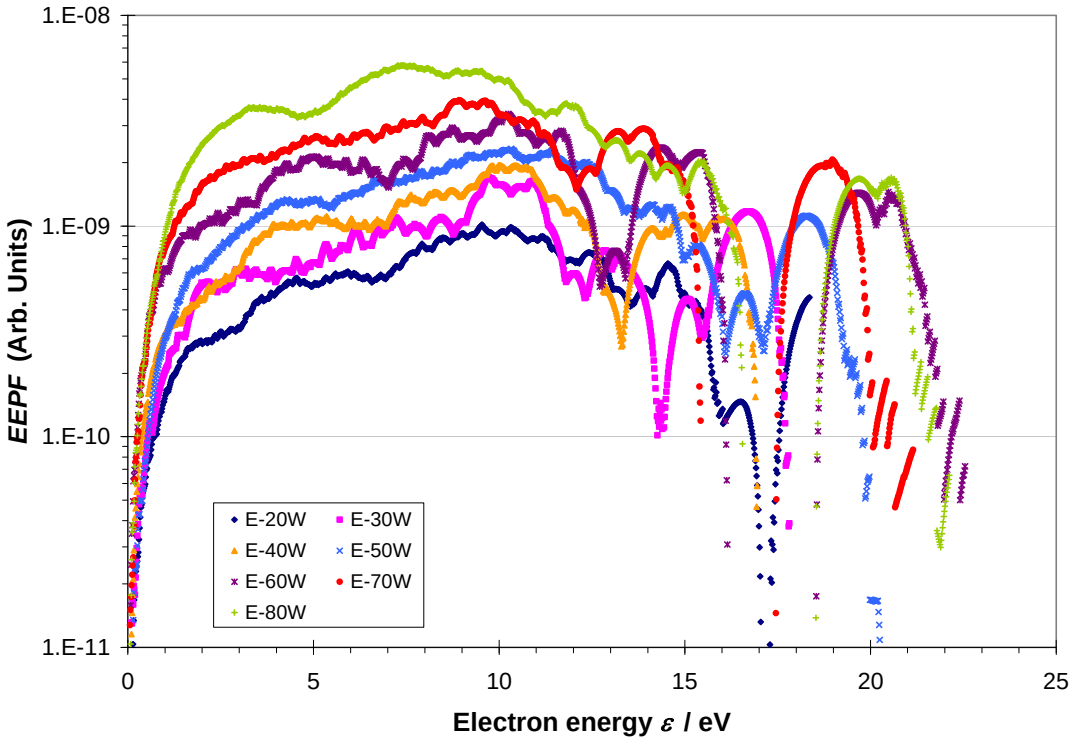

Figure 5.8(b): Semi-logarithmic version of *EEPF* against electron energy ε plot in Figure 5.8(a).

The *EEPF* for *E* mode in Figure 5.8(a) has quite a flat shape especially at lower RF power or convex shape as shown in Figure 5.8(b). The energy gap between the zero crossing point and peak *EEPF* is quite large (approximately 10 eV). This is largely due to the distortion in the *I-V* curve of the probe resulting from the presence of large circuit resistance R_c [44]. However, argon gas is known to exhibit the Ramsauer effect where the collision probability increases with electron energy within the range of 1 – 10 eV [52]. This could contribute to the depletion of the low energy electrons as they could be effectively accelerated by the RF electric field and escape from the low energy region of

the *EEPF*. As RF power is increased, the increase in electron density is reflected in the increase in the *EEPF*. The energy gap (between 0 and the peak of *EEPF*) narrows at higher RF power. Multiple peaks are observed in the *EEPF* and are more likely to be artifacts brought on by the poor resolution of the acquired *I-V* data from the 8-bit oscilloscope. This can lead to heavy distortion especially in the second derivative of the electron current.

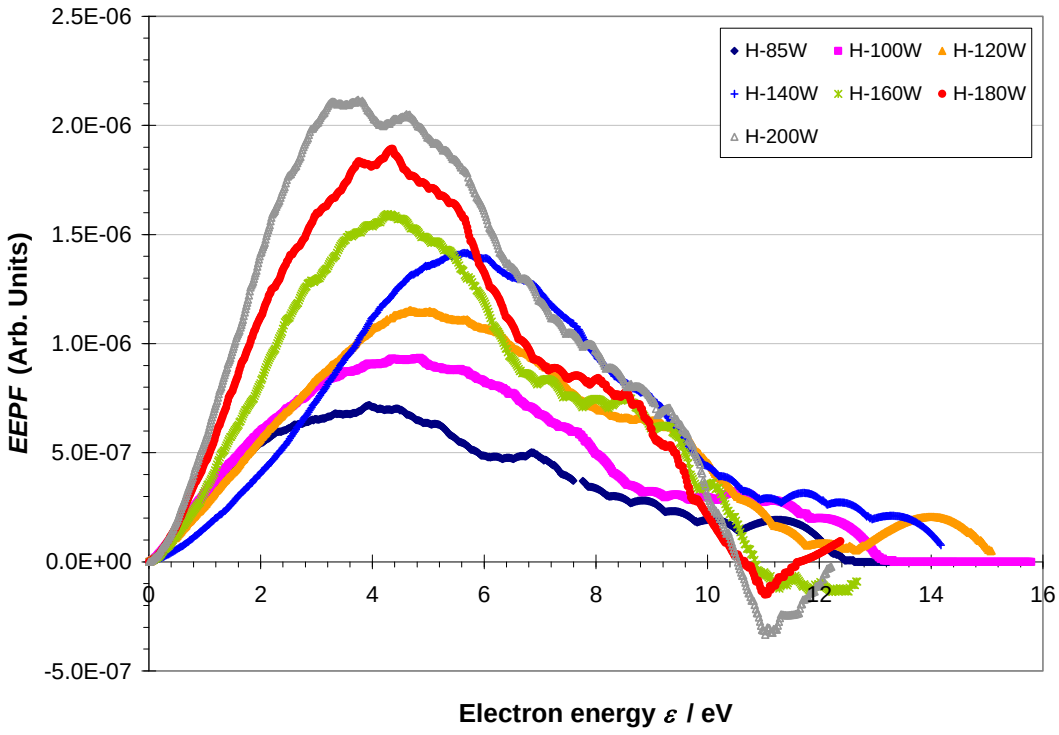

Figure 5.9: *EEPF* against electron energy ε at various RF powers in *H* mode for fixed argon pressure of 0.10±0.01 mbar and flowrate 20 sccm. (m = 140)

In the case of *H* mode shown in Figure 5.9, it is again observed that the *EEPF* increases with RF power. From 85 W to 120 W, the *EEPF* peak gradually shifts to higher electron energy when RF power is increased. At 140 W, *EEPF* is comparatively most depleted at the low electron energy end, pushing the *EEPF* peak to appear at

higher electron energy ε. The trend reverses for P_{rf} > 140 W with the *EEPF* peak occurring at decreasing ε as P_{rf} is increased. The *EEPF* curves also exhibit another slight 'bump' hinting the presence of another group of electrons at higher energy.

Though the energy gap between the zero crossing and the *EEPF* peak is narrower by half compared to *E* mode, it is still wide. For the *H* mode, the current sensing resistor of 10 Ω is still too large. However, too small a resistance will not yield a significantly measurable voltage drop for sensing the probe current.

The semi-logarithmic plots of the second derivative d^2I_e/dV_p^2 against electron energy ε and against the electron energy squared ε^2 are shown in Figures 5.10 and 5.11 respectively. All the curves show convex shape in Figures 5.10. The curves at extreme powers (85 W and 200 W) are compared and it may be deduced that the second derivative at 85 W is comparatively more linear in Figure 5.11 (inclining towards Druyvesteyn-like). At higher RF power 200 W, the difference is not so clear for this set of data. However, with reference to Figures 3.16(a) and (b) under the same conditions, it may be concluded that it shows more inclination towards Maxwellian-like distribution. *Godyak et al.* [44] also showed Maxwellian *EEPF* at high pressure ICP (above 0.133 mbar) but at 50 W and 6.78 MHz. At higher RF power where the electron density is higher, the electron-electron collisions frequency is high, hence, the distribution of the electron energy will become nearly Maxwellian [37,53]. The second derivative curves for the in-between powers exhibit at least two linear regions, indicating two temperature regions. These energy distributions are more Druyvesteyn-like up to 140 W. For the 160 W and 180 W, it could not be concluded decisively its distribution type.

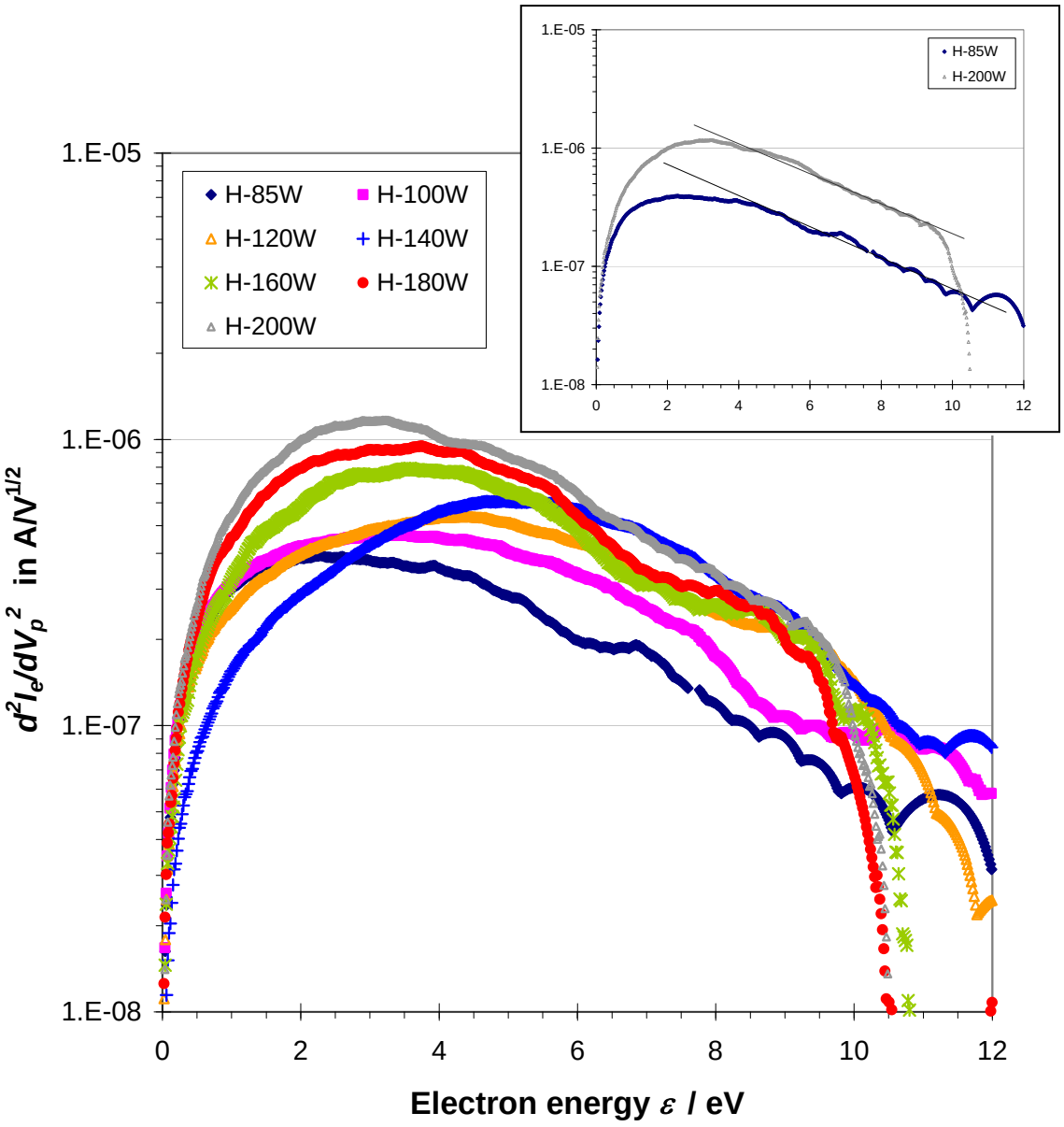

Figure 5.10: Semi-log plot of the second derivative of the electron current against electron energy ε. Inset shows curves for the extreme RF powers as indicated.

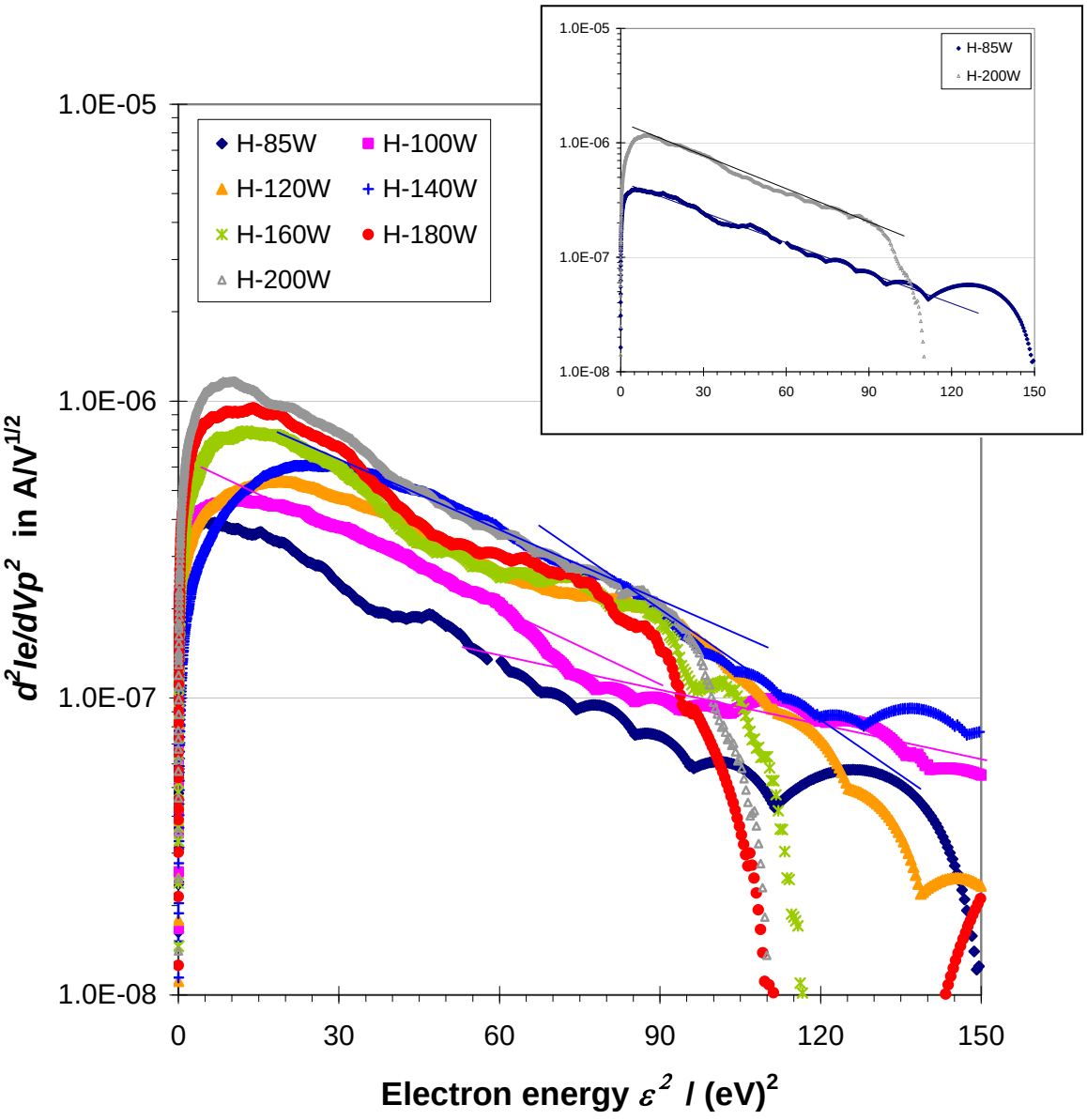

Figure 5.11: Semi-log plot of the second derivative of the electron current against the electron energy squared ε^2. Inset shows curves for the extreme RF powers as indicated.

5.2 MEASUREMENT USING PROBES OF DIFFERENT DIAMETERS

It has been shown in Section 5.2 that the plasma characteristics are consistent, independent of whether it was measured while RF power is increasing or decreasing. Thus, in the following comparison, only parameters measured while RF power is increasing are displayed.

5.2.1 ELECTRON TEMPERATURE

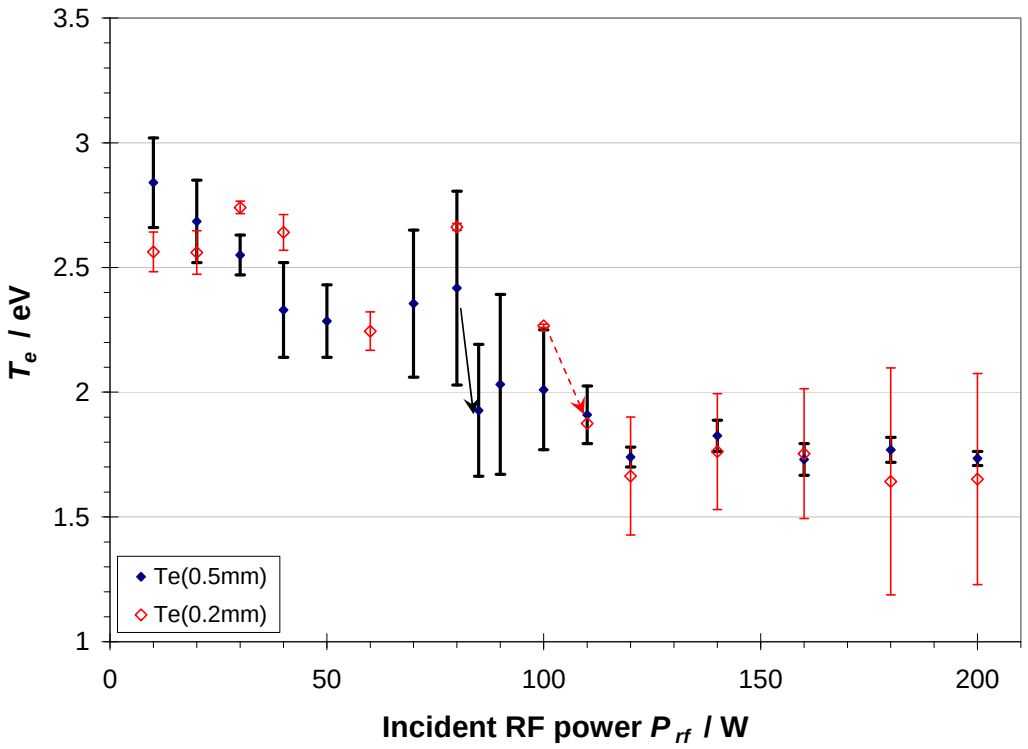

Figure 5.12: Electron temperature against RF power at argon pressure of (0.10±0.01) mbar and flowrate of 20 sccm for probe tips of diameter of 0.2 mm and 0.5 mm.

Figure 5.12 shows the graph of electron temperature against RF power for two different probe tip diameters. It can be seen that the electron temperature T_e deduced

using the two probe tips are similar. The trend of variation with RF power is consistent. Only difference is in the power at which mode transition occurs, whereby, the onset is at 80 W for the 0.5 mm diameter probe tip and 100 W for the smaller one. This difference is within the variation of the onset power for $E \rightarrow H$ mode transition and not likely to be due to the probe tip size.

5.2.2 ELECTRON DENSITY

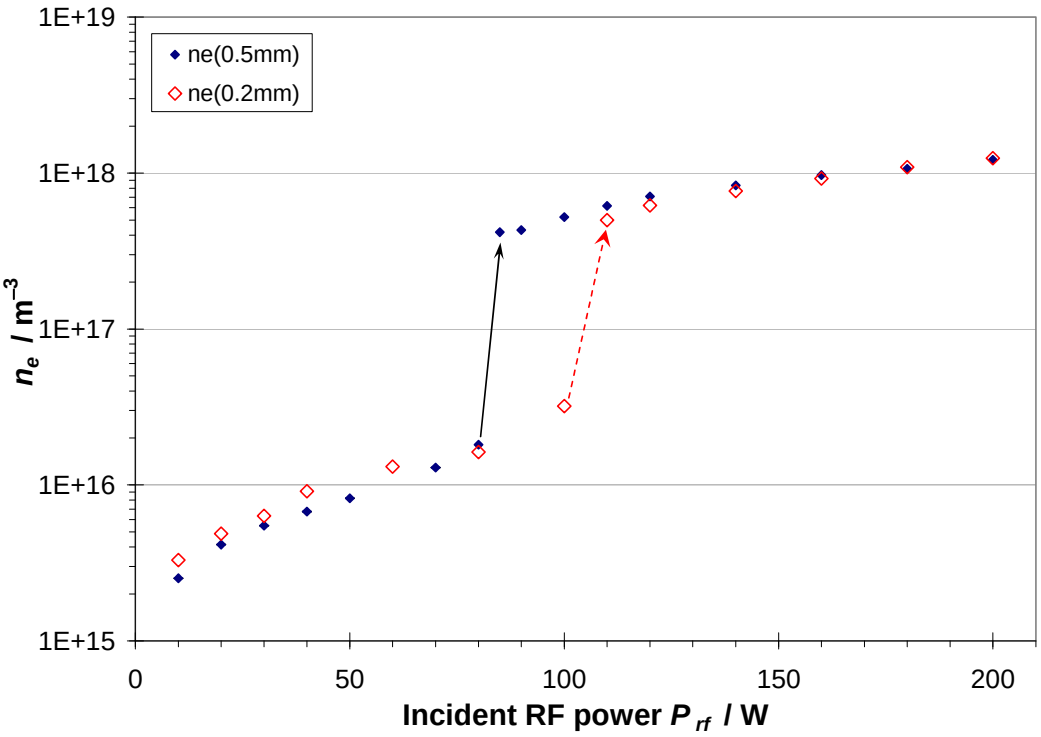

Figure 5.13: Semi-logarithmic plot of electron density n_e against RF power at argon pressure of (0.10±0.01) mbar and flowrate of 20 sccm for probe tips of diameter of 0.2 mm and 0.5 mm. n_e is calculated from the ion current part of the probe characteristic.

The magnitude of n_e shown in Figure 5.13 for both the probe sizes differs very little (except at the mode transition region similar to the case of electron temperature in the preceding section) in both *E* and *H* modes. However, larger difference is observed in

n_e deduced from the electron saturation current (Figure 5.14). Smaller probe diameter means lesser disturbance to the plasma, but the probe wire resistance is increased, thereby, increasing the probe circuit resistance R_c. As discussed in Section 5.2.2, it will distort the region near the plasma potential (and the electron saturation current), hence, the larger difference (averaging at 25 %) observed.

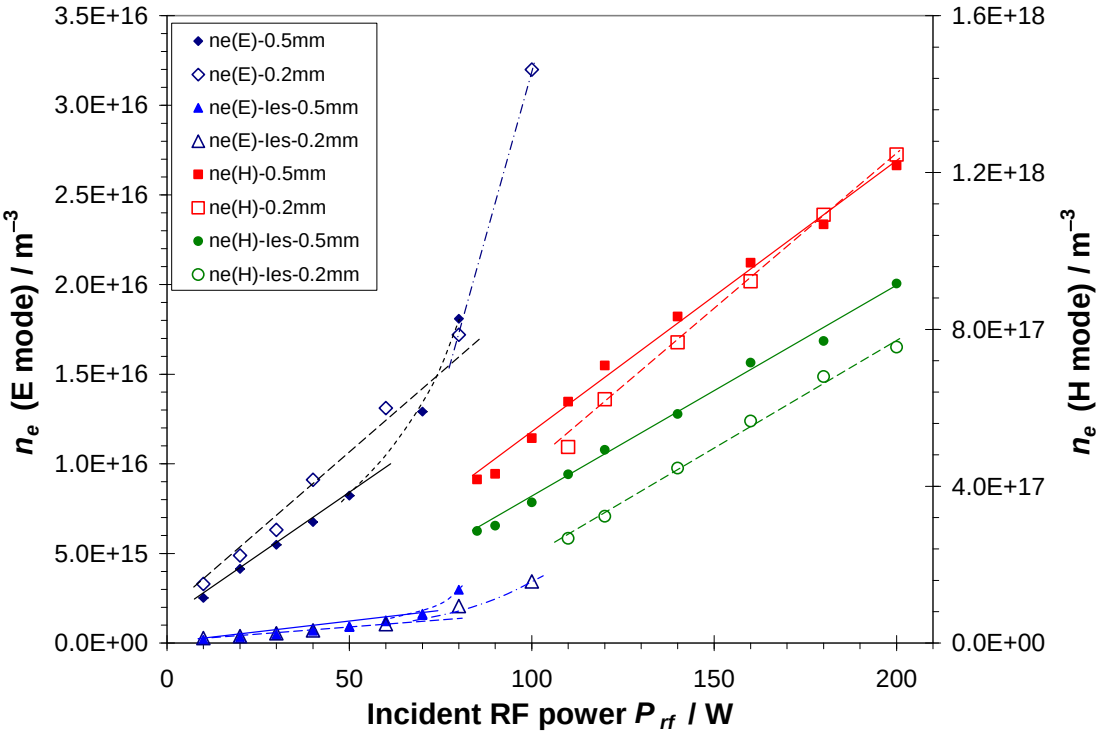

Figure 5.14: Linear plot of electron density n_e against RF power for the same conditions as in Figure 5.13.

5.3.3 PLASMA POTENTIAL AND FLOATING POTENTIAL

It is can be seen from Figure 5.15 that the magnitude of the plasma potential V_s and floating potential V_f are similar for both the probe sizes. Their variations with RF power have the same trend (except at the mode transition region as has been discussed in Section 5.3.1).

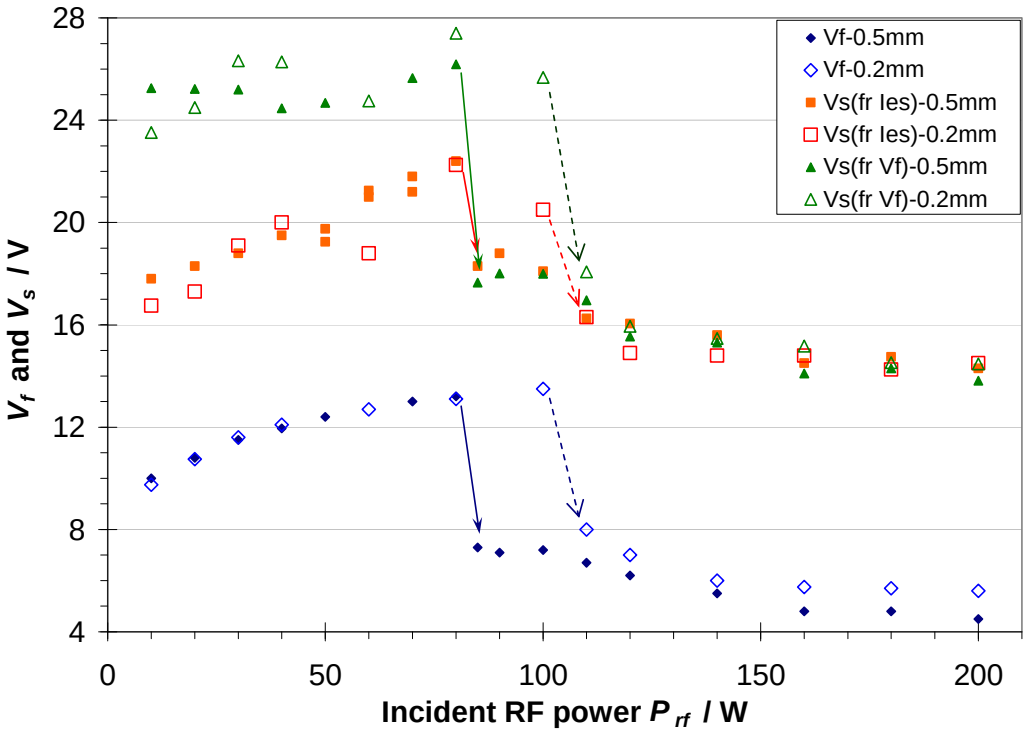

Figure 5.15: Plasma potential V_s and floating potential V_f against RF power at argon pressure of (0.10±0.01) mbar and flowrate of 20 sccm for probe tips of diameter of 0.2 mm and 0.5 mm.

5.3 RADIAL MEASUREMENT

The dependence of plasma characteristics on the radial position at fixed axial distance of 4.2 cm from the quartz plate has been investigated. The probe measurement has been carried out at argon flowrate of 20 sccm and pressure of 0.10 (± 0.01) mbar. For *E* mode regime, the RF power was set at 50 W whereas in *H* mode regime, RF power of 200 W was used.

5.3.1 ELECTRON TEMPERATURE

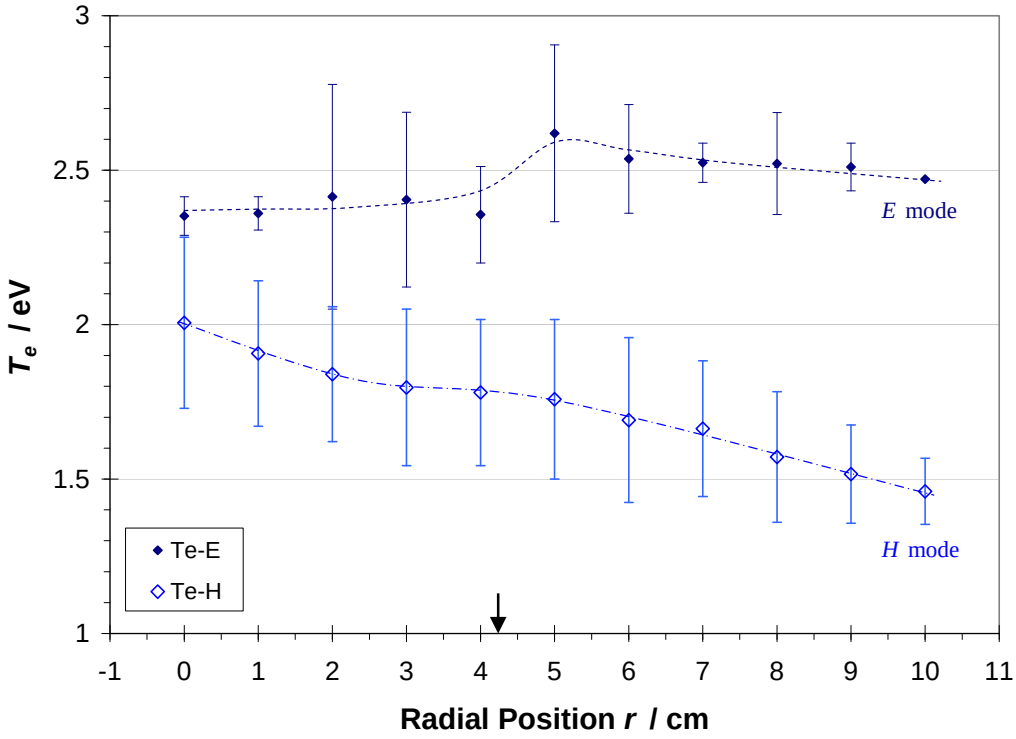

Figure 5.16: Electron temperature against radial distance for the *E* mode (50 W) and *H* mode (200 W) in argon pressure of (0.10±0.01) mbar at flowrate 20 sccm. The arrow indicates the edge of the induction coil.

Figure 5.16 shows the graph of electron temperature against probe radial distance. It can be seen that the radial distribution of the electron temperature T_e for the *E* and *H* modes differs. *E* mode is sustained at higher T_e (2.4 – 2.6 eV) when compared to *H* mode (T_e = 2.0 – 1.5 eV). In the *H* mode, T_e decreases gradually as the radial distance increases except at region r = 2.5 to 4.5 cm where it is rather constant. However for the *E* mode, it is quite constant over the expanse of the induction coil up to r = 4 cm, before increasing suddenly, and at $r \geq 6$ cm, it is quite flat. This trend is similar to that reported by *Mahoney et al.*[36] but at 0.013 mbar and 200 W argon ICP.

5.3.2 ELECTRON DENSITY

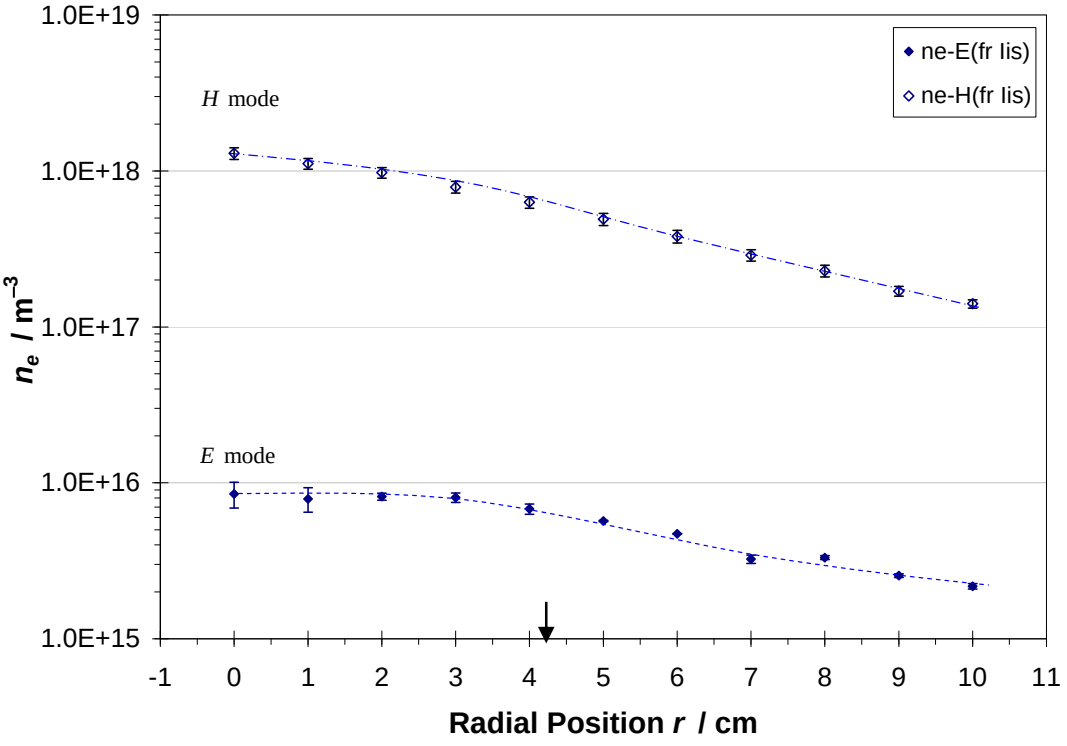

Figure 5.17: Radial profile of the electron density n_e for the *E* mode (50 W) and *H* mode (200 W) in argon pressure of (0.10±0.01) mbar at flowrate 20 sccm. The arrow indicates the edge of the induction coil.

The electron density n_e shown in Figure 5.17 is found to decrease gradually when the probe is placed farther from the centre of the plasma chamber for both the *E* and *H* modes. n_e drops by 50 % at the radial position corresponding to the edge of the planar coil for the *H* mode, and by 25 % for the *E* mode. At r = 10 cm (≈ double the radius of the planar coil), n_e in the *H* mode drops by one order of magnitude (90 %) while for the *E* mode, its decrease is less at 75 %. It can be said that the *E* mode discharge is radially more diffuse and uniform. The radial profile for the inductive mode is similar to those reported by *Schwabedissen et al.* [54] in an argon ICP at low pressure of 0.005 mbar with net RF power 60 W and by *Mahoney et al.* [36] in a 0.013 mbar, 200 W argon discharge having lower peak n_e value of 1.9×10^{17} cm^{-3}.

5.3.3 PLASMA POTENTIAL AND FLOATING POTENTIAL

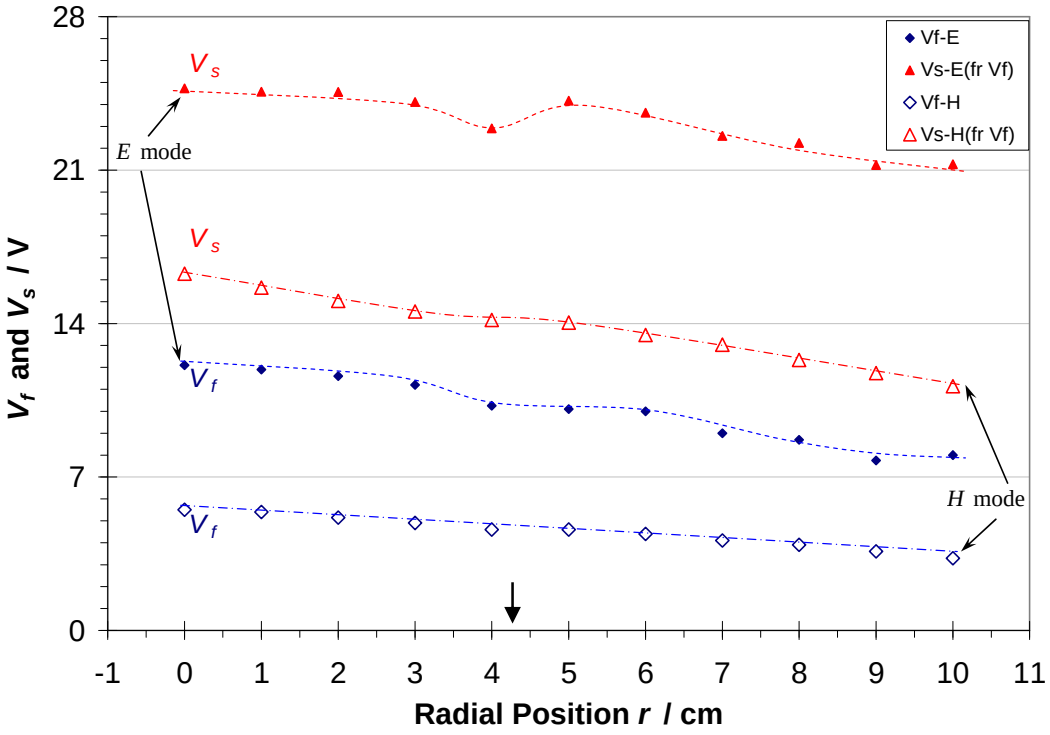

Figure 5.18: Radial profiles of the floating potential V_f and plasma potential V_s for the *E* mode (50 W) and *H* mode (200 W) in argon pressure of (0.10±0.01) mbar at flowrate 20 sccm. The arrow indicates the edge of the induction coil.

The plasma potential V_s shown in Figure 5.18 for the *E* mode is quite uniform over the expanse of the induction coil. At the edge (r ~ 4 cm) there is a slight dip before rising again and then decreases slowly as the radial distance r increases. Again it is shown that *H* mode has lower V_s, and it is found to decrease slowly with increasing r. This spatial profile of V_s is consistent with those of *Mahoney et al.* [36]. The floating potential V_f for both modes decreases slowly with increasing r though V_f for *E* mode is higher than those for *H* mode.

5.3.4 ELECTRON ENERGY PROBABILITY FUNCTION (*EEPF*)

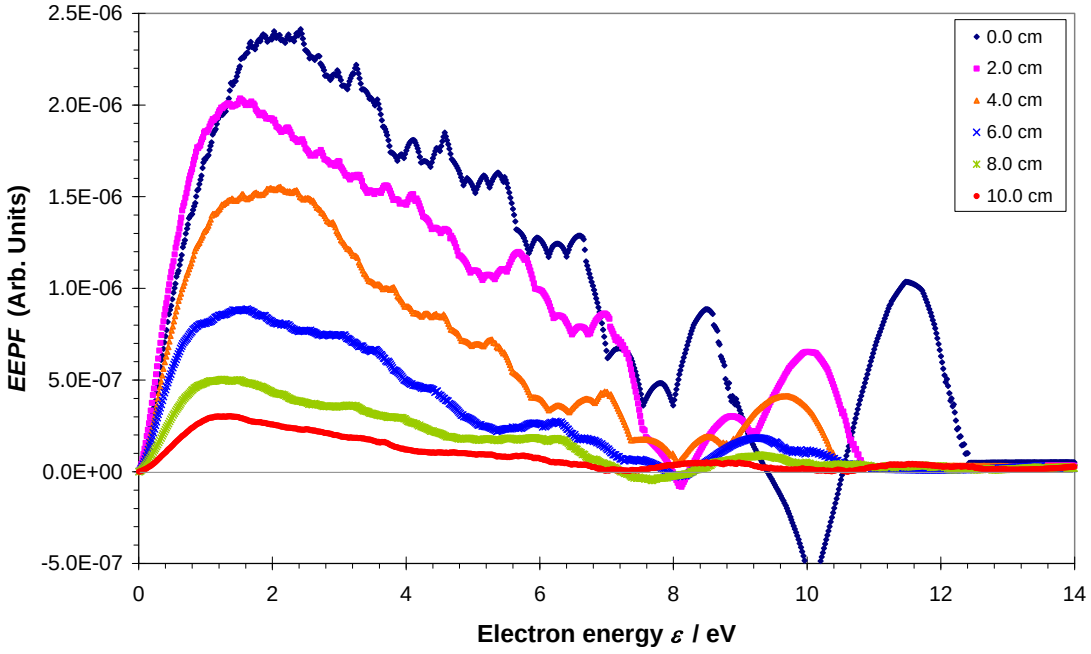

Figure 5.19: The *EEPF* at various radial distances from the axis of the induction coil for the *H* mode (200 W) argon discharge at (0.10±0.01) mbar 20 sccm flowrate.

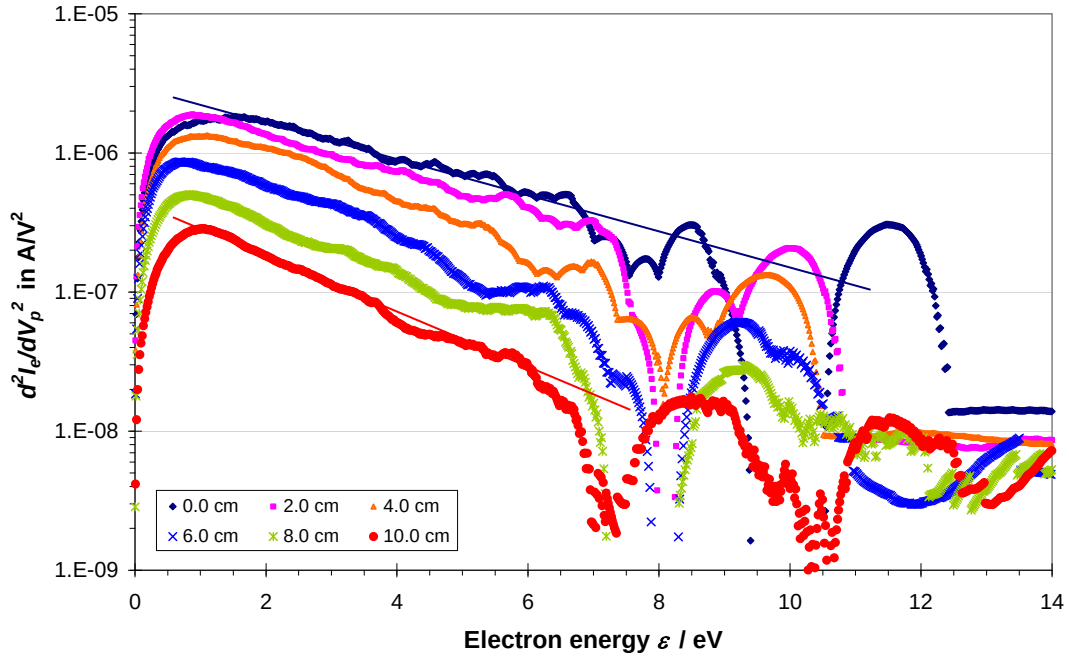

Figure 5.20: The semi-logarithmic plot of the *EEPF* of Figure 5.19.

Figure 5.19 shows the *EEPF* measured at various radial distances *r* and Figure 5.20 gives the semi-logarithmic plot of the same. The *EEPF* decreases as *r* increases in line with the trend of radial profile of n_e. It can be concluded that all the *EEPFs* exhibit Maxwellian-like distribution.

CHAPTER 6 CONCLUSIONS AND SUGGESTIONS FOR FURTHER WORK

6.1 CONCLUSIONS

In this project, the study of the electrical characteristics of 13.56 MHz radio frequency inductively coupled plasma (RF ICP) in argon has been focused on RF breakdown, voltage and current trends in the RF impedance matching circuit, power coupling efficiency, and *E-H* mode transition. The second part investigates the plasma characteristics such as electron temperature, electron density, plasma and floating potentials, and electron energy distribution function. These were deduced from the Langmuir probe measurement. Radial distribution of the plasma parameters was also studied.

In the investigation of the RF breakdown characteristic, it is found that breakdown potential versus pressure ($U_b - p$) plot has shape similar to that of Paschen curve for DC breakdown even though the electrode is not in direct contact with the discharge. The minimum occurs at p = 0.1 mbar which is close to that calculated by *Burm* [33] in which the induced electric field from the applied oscillating magnetic field was considered. Minimum peak breakdown potential, U_b = 270 V (peak value) corresponds to potential difference of 80 V between the two outermost adjacent turns of the coil and this is close to that reported by *Lisovskiy et al.* [30] in a capacitive discharge. It is concluded that the RF breakdown in this external electrode configuration

is initiated by both the capacitively coupled electric field that results from large potential drop across adjacent turns of the induction coil as well as the electric field induced by the oscillating magnetic field. The discharge sustaining voltage U_{st} is found to be slightly lower than the breakdown voltage U_b as the discharge has begun conducting upon ignition and requires lower voltage level to sustain it. The breakdown potential has little dependence on argon gas flowrate as the differences observed among the investigated flowrates are small.

The two modes of discharge (*E* and *H*) are identified from the current and voltage measured in the RF circuit when the incident RF power was varied at fixed argon pressure of 0.13 mbar. *E* mode occurs at low RF power whilst *H* mode at high power. On increasing the RF power, *E* to *H* transition occurs and is accompanied by both current and voltage drops measured in the induction coil antenna (henceforth referred to as *antenna*) and secondary coil of the step-down transformer (henceforth referred to as *secondary* coil). The trend is different in the primary coil of the step-down transformer (henceforth referred to as *primary* coil) which records a drop in current and rise in voltage as there is no abrupt change in the input RF power. When the RF power is progressively decreased, the trend is reversed for the *H* to *E* transition and it occurs at lower RF powers resulting in a hysteresis of width 20 W. From these current and voltage measurement, resistances of the induction coil *antenna*, *primary* and *secondary* coils were computed for *E* and *H* mode discharges and these are tabulated in Table 6.1.

Table 6.1: Computed resistances for the *antenna*, *primary* and *secondary* coils.

	***E* mode**	***H* mode**	**No plasma**
Antenna resistance R_a / Ω	1.12 ± 0.01	2.00 ± 0.01	1.023 ± 0.006
Primary coil resistance R_{pc} / Ω	61 ± 1	114 ± 1	-
Secondary coil resistance R_{sc} / Ω	1.49 ± 0.03	2.77 ± 0.02	-

It is deduced that the additional resistance R_p (in Eq.(3.3)) reflected into the circuit when the plasma is present is larger for the *H* mode (0.98±0.01 Ω) than *E* mode (0.10±0.01 Ω). The almost zero reflected RF power in *E* mode and higher level (up to 18 W at 300 W) at *H* mode indicates the present configuration of the impedance matching network is more efficient in matching the impedances at *E* mode. From the *primary* and *secondary* resistances, the effective turns ratio of the step-down transformer is estimated to be 6.4.

The power transfer efficiency ξ for argon ICP (0.1 mbar, 30 sccm flowrate) is better in *H* mode with value of 0.34 – 0.45 and it is one order of magnitude larger than that in *E* mode and is comparable to those reported by *Suzuki et al.* [34]. The constant of proportionality relating the power dissipated in the plasma to the electron density is $(6.5\pm0.3)\times10^{-17}$ W/m^{-3} indicating lesser loss of power transfer compared to the same reported work of *Suzuki et al*.

On the mode transition trends, the switchover power, voltage and current for *E* to *H* mode transition is higher compared to that of the reverse *H* to *E* mode transition. For the *E* to *H* mode transition, they initially decrease with pressure up to 0.1 mbar before increasing with increasing pressure. On the other hand, the switchover power, voltage and current for *H* to *E* mode transition initially decrease with increasing pressure up to ~ 0.4 mbar, after which they hardly change. The resulting hysteresis range displays a minimum at 0.1 mbar. Hysteresis is attributed to the presence of non-linearities in the circuit and plasma which results in existence of more than one stable equilibrium of the electron power balance equation. These non-linearities [51] resulted possibly from the presence of capacitive sheaths in a real inductive discharge (unshielded) as well as Coulomb collisions and multi-step ionization.

The investigation of dependence of plasma characteristics on incident RF power showed different properties of *E* and *H* mode ICPs. The results are tabulated in Table 6.2.

Table 6.2: Summary of characteristics of argon RF ICP at (0.10±0.01) mbar and flowrate of 20 sccm.

Plasma Properties	***E* mode**		***H* mode**	
	Magnitude	**Trend of variation with increasing RF power**	**Magnitude**	**Trend of variation with increasing RF power**
Electron temperature T_e in eV	2.8 – 2.3	Decreases (steeper)	2.0 – 1.7	Decreases
Electron density n_e in m^{-3}	2.5×10^{15} – 1.81×10^{16}	Increases	3.6×10^{17} – 1.22×10^{18}	Increases (steeper)
Plasma potential V_s in V	25 – 26	Increases (very little)	18 – 14	Decreases
Floating potential V_f in V	9.6 – 13.2	Increases	7.5 – 4.5	Decreases
Plasma Properties	***E* mode**		***H* mode**	
EEPF	• Profile is distorted with peak at high electron energy (~10 eV); highly depleted at low energy end • Distribution profile increases in magnitude as RF power increases reflecting increasing electron density • Peak shifts to lower electron energy as RF power increases • Distribution type could not be deduced due to high distortion		• Profile slightly distorted with depletion at low energy • Distribution profile increases in magnitude as RF power increases reflecting increasing electron density • Peak occurs at increasing electron energy as RF power increases up to 140 W before shifting to decreasing energy • Inclined to Druyvesteyn-like at 85 – 140 W changing to Maxwellian-like at 200 W	

The *H* mode ICP has higher electron density resulting in more electron-electron collisions, hence, sustained at lower electron temperature. The electron density increases by more than one order of magnitude with increasing of power. Low RF power leads to lower degree of ionization, resulting in a lower overall density. The plasma potential and floating potential increase very little with the increasing of RF power under *E* mode. The increase is steeper under *H* mode.

On the electron energy distribution, *EEPF* is heavily distorted under *E* mode especially near the electron saturation current part and it is deduced that the large current sensing resistor has contributed to this. The distortion is much reduced under *H* mode where the circuit resistance is approximately lower by two orders of magnitude and the electron energy distribution could be deduced. The high electron density at high RF power (200 W) makes possible much more electron-electron collisions, hence, resulting in a Maxwellian-type *EEDF*.

From the measurement using probes with different tip diameters (0.2 mm and 0.5 mm), it was found that there is little difference between the plasma characteristics deduced. Hence, both sizes are appropriate to be used in the present operating conditions of the argon RF ICP.

In the measurement of the radial distribution of plasma properties, it was found that most of the plasma properties (n_e, V_s and V_f) generally decline with increasing radial distance r at fixed axial height of 4.2 cm from the quartz window, the decline being steeper for *H* mode discharge. The trends are consistent with those reported by *Schwabedissen et al.* [54] and *Mahoney et al.* [36] in ICP. In the case of electron temperature T_e, it showed decrease with increasing r only in the *H* mode, whilst the *E* mode exhibited almost no variation over the area of the coil. Near the coil edge, T_e jumps to higher value before decreasing slowly as r increases further. This is consistent

with those shown by *Mahoney et al.* [36]. It was concluded that *E* mode is more diffuse and uniform. The distribution of electron energy is found to be Maxwellian-like over the entire radial distances studied in the *H* mode discharge at 200 W, though the *EEPF* magnitude decreases with increasing *r* consistent with the radial variation of n_e.

6.2 SUGGESTIONS FOR FURTHER WORK

The following are suggested as further work to improve on the present results:

(a) To design an impedance matching network capable matching over wider range of resistance to include accommodating the higher reflected resistance in the circuit during the *H* mode plasma;

(b) To reduce the Langmuir probe circuit resistance R_c, particularly, the current sensing resistor so that the distortion to the *I-V* characteristic near the plasma potential region may be eliminated;

(c) To use a higher resolution data acquisition device (12-bit or 16-bit) so that the second derivative of the electron current may be extracted with less distortion;

(d) To measure the plasma characteristics using other techniques such as microwave interferometer or optical emission spectroscopy in order to verify the data obtained through the Langmuir probe technique.

(e) To investigate dependence of RF ICP characteristics on pressure (extend the present study to lower and higher pressures).

APPENDIX A

Circuit Diagram of the 12 V d.c. Power Supply

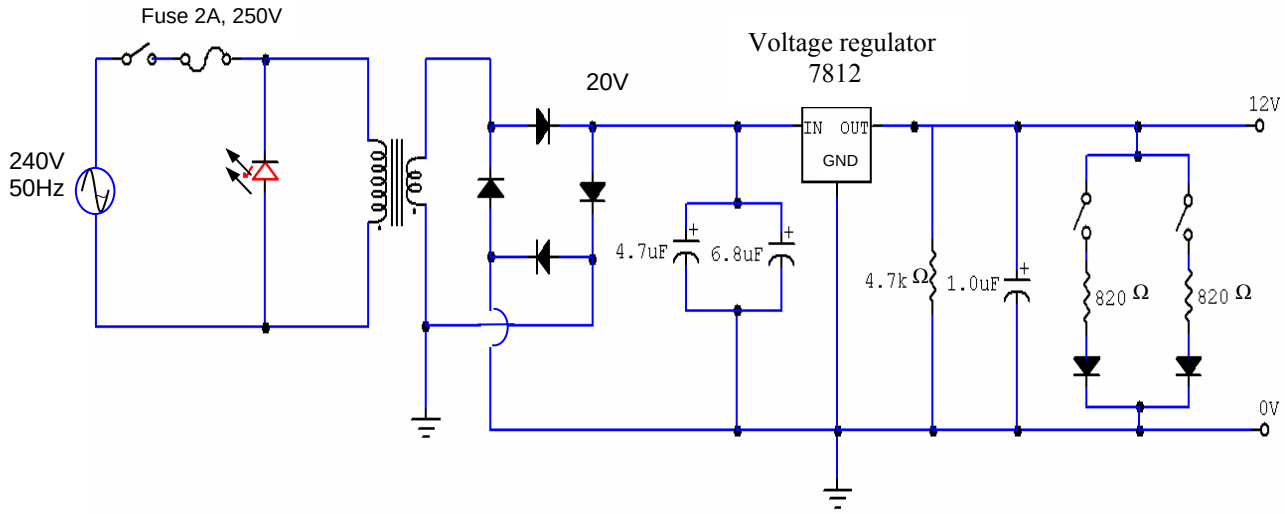

APPENDIX B

Circuit Diagram of the AD215 Isolation Amplifier configured for Unity Gain

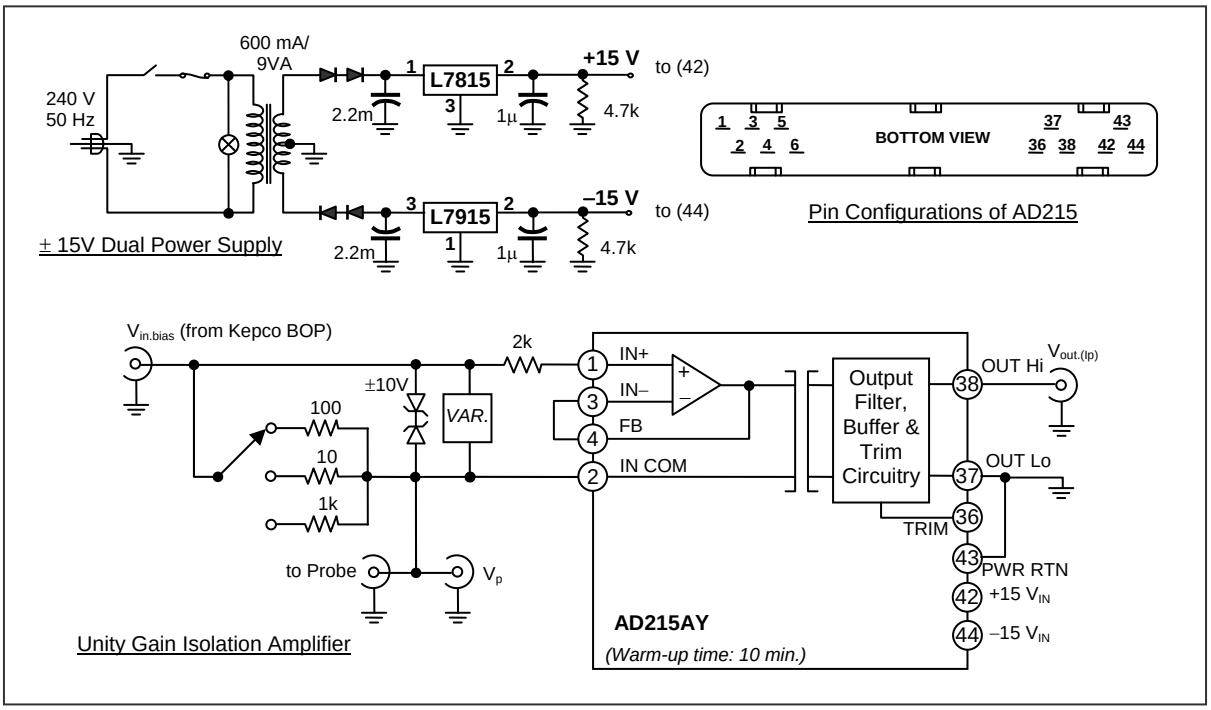

APPENDIX C

Listing of C++ Program written for the smoothing technique

```
#include <cmath>
#include <cstdlib>
#include <iomanip>
#include <iostream>
#include <fstream>

using namespace std;

int main()
{
  int i,j,k,M=100,N=2300;
  double TIME[2300],VOLT[2300],CURR[2300];
  double ECUR[2300],D1CR[2300],D2CR[2300];
  double EVLT[2300],D1VT[2300],EEDF[2300];
  double MM,NUM0,NUM2,DEN0,DEN1,DEN2;
  double WC0,WC1,WC2,WV0,WV1;

/*********************************************************************/
  ofstream od1,od2;
  ifstream id1;
/*********************************************************************/
  od1.open("output.dat",ios::out);
  if(od1.fail())
  { cout << "Error in opening output.dat" << endl;
    return 1;
  }

  od2.open("check.dat",ios::out);
  if(od2.fail())
  { cout << "Error in opening check.dat" << endl;
    return 1;
  }

  id1.open("input.dat",ios::in);
  if(id1.fail())
  { cout << "Error in opening input.dat" << endl;
    return 1;
  }
/*********************************************************************/
```

```
for(i=0;i<N;++i){  //initialization
   TIME[i]=0.0;
   VOLT[i]=0.0;
   CURR[i]=0.0;
}

for(i=0;i<N;++i) // read in the data
   id1 >> TIME[i] >> VOLT[i] >> CURR[i];

//for(i=0;i<N;++i) // read in the data
  // od2 << TIME[i] << "\t" << VOLT[i] << "\t" << CURR[i] << endl;

MM=(double) M;

for(i=M;i<N-M;++i){
   WC0=0.0;
   WC1=0.0;
   WC2=0.0;
   WV0=0.0;
   WV1=0.0;
   for(j=-M;j<M;++j){
      NUM0=3.0*MM*(MM+1.0)-1.0-5.0*(double)(j*j);
      NUM2=3.0*(double)(j*j)-MM*(MM+1.0);
      WC0=WC0+NUM0*CURR[i+j];
      WC1=WC1+(double)j*CURR[i+j];
      WC2=WC2+NUM2*CURR[i+j];
      WV0=WV0+NUM0*VOLT[i+j];
      WV1=WV1+(double)j*VOLT[i+j];
   }

   DEN0 = (4.0*MM*MM-1.0)*(2.0*MM+3.0)/3.0;
   DEN1 = MM*(MM+1.0)*(2.0*MM+1.0)/3.0;
   DEN2 = MM*(MM+1.0)*(2.0*MM+3.0)*(4.0*MM*MM-1.0)/30.0;

   EVLT[i]=WV0/DEN0;
   D1VT[i]=WV1/DEN1;
   ECUR[i]=WC0/DEN0;
   D1CR[i]=WC1/DEN1;
   D2CR[i]=WC2/DEN2;
   EEDF[i]=D2CR[i]/(D1VT[i]*D1VT[i]); // in units of A/V2

  od1 << scientific << TIME[i] << "\t" << EVLT[i] << "\t"
      << ECUR[i] << "\t" << EEDF[i] << "\t"
      << D1CR[i] << "\t" << D2CR[i] << "\t" << D1VT[i] <<endl;
}
```

```
    id1.close();
    od1.close();
    od2.close();

    system("PAUSE");
    return EXIT_SUCCESS;
}
```

REFERENCES

[1] National Research Council on the National Academies, *Plasma Science: Advancing Knowledge in the National Interest*, Washington, D.C.: The National Academies Press (2007).

[2] J.L. Shohet, "Plasma-aided manufacturing", IEEE Trans. Plasma Sci. **19** (1991), 725-733.

[3] N. Hershkowitz, "Role of plasma-aided manufacturing in semiconductor fabrication", IEEE Trans. Plasma Sci. **26** (1998), 1610-1620.

[4] M.A. Lieberman and Allan J. Lichtenberg, *Principles of Plasma Discharges and Materials Processing*, New York: John Wiley & Sons (1994).

[5] J.H. Keller, "Inductive plasmas for plasma processing", Plasma Sources Sci. Technol. **5** (1995), 166-172.

[6] J. Hopwood, "Review of inductively coupled plasmas for plasma processing", Plasma Sources Sci. Technol. **1** (1992), 109-116.

[7] R.W. Boswell and F.F. Chen, "Helicons – The early years", IEEE Trans. Plasma Sci. **25** (1997), 1229-1244.

[8] F.F. Chen and R.W. Boswell, "Helicons – The past decade", IEEE Trans. Plasma Sci. **25** (1997), 1245-1257.

[9] J. Asmussen, T.A. Grotjohn, P. Mak, and M.A. Perrin, "The design and application of electron cyclotron resonance discharges", IEEE Trans. Plasma Sci. **25** (1997), 1196-1221.

[10] H. Tsuboi, M. Itoh, M. Tanabe, T. Hayashi, T. Uchida, "Usefulness of magnetic neutral loop discharge plasma in plasma processing", Jpn. J. Appl. Phys. **34** (1995), 2476-2481.

[11] P. Scheubert, U. Fantz, P. Awakowicz, and H. Paulin, "Experimental and theoretical characterization of an inductively coupled plasma source", J. Appl. Phys. **90** (2001), 587-598.

[12] U. Kortshagen, I. Pukropski, and M. Zethoff, "Spatial variation of the electron distribution function in a rf inductively coupled plasma: Experimental and theoretical study", J. Appl. Phys. **76** (1994), 2048-2058.

[13] F.F. Chen, "Chapter 4: Electric Probes" in *Plasma Diagnostic Techniques*, ed. R.H. Huddlestone and L.S. Lovberg, Academic Press: New York (1965).

[14] A. Boschi and F. Magistrelli, "Effect of a R.F. Signal on the Characteristic of a Langmuir Probe", Il Nuovo Cimento **XXIX** (1963), 3597-3609.

[14a] Abdul Hakim Hashim, *Nitriding of titanium by inductively coupled plasma*, M.Sc. dissertation, University of Malaya (2002).

[15] J.W. Denneman, "Determination of electromagnetic properties of low-pressure electrodeless inductive discharges", J. Phys. D: Appl. Phys. **23** (1990), 293-298.

[16] H. Kawata, T. Kubo, and K. Murata, "Electrical properties of planar RF discharges including the second harmonic frequency", Jpn. J. Appl. Phys. **33** (1994), 4365-4368.

[17] V.A. Godyak, R.B. Piejak, and B.M. Alexandrovich, "Electrical characteristics and electron heating mechanism of an inductively coupled argon discharge", Plasma Sources Sci. Technol. **3** (1994), 169-176.

[18] I.M. El-Fayoumi and I.R. Jones, "Measurement of the induced plasma current in a planar coil, low frequency, RF induction plasma source", Plasma Sources Sci. Technol. **6** (1997), 201-211.

[19] U. Kortshagen, N.D. Gibson, and J.E. Lawler, "On the E-H mode transition in RF inductive discharges", J. Phys. D: Appl. Phys. **29** (1996), 1224-1236.

[20] I.M. El-Fayoumi, I.R. Jones, and M.M. Turner, "Hysteresis in the E- to H-mode transition in a planar coil, inductively coupled rf argon discharge", J. Phys. D: Appl. Phys. **31** (1998), 3082-3094.

[21] K. Ostrikov, E. Tsakadze, J. Ning, Z. Tsakadze, L. Jidong, R. Storer, and S. Xu, "Dynamics of mode transitions in inductively-coupled plasmas", IEEE Trans. Plasma Science **30** (2002), 128-129.

[22] M.A. Razzak, S. Takamura, and Y. Uesugi, "Effects of radio-frequency driving power, gas pressure, and nitrogen seeding on the transition dynamics in argon inductively coupled plasmas", J. Appl. Phys. **96** (2004), 4771-4776.

[23] J. Hopwood, C.R. Guarnieri, S.J. Whitehair, and J.J. Cuomo, "Langmuir probe measurements of a radio frequency induction plasma", J. Vac. Sci. Technol. **A11** (1993), 152-156.

[24] S. Xu, K.N. Ostrikov, Y. Li, E.L. Tsakadze, and I.R. Jones, "Low-frequency, high-density, inductively coupled plasma sources: Operation and applications", Phys. Plasmas **8** (2001), 2549-2555.

[25] U. Kortshagen, I. Pupkropski, and L.D. Tsendin, "Experimental investigation and fast two-dimensional self-consistent kinetic modelling of a low-pressure inductively coupled rf discharge", Phys. Rev. E **51** (1995), 6063-6077.

[26] S. Rauf, and M.J. Kushner, "Model for noncollisional heating in inductively coupled plasma processing sources", J. Appl. Phys. **81** (1997), 5966-5974.

[27] V.I. Demidov, C.A. DeJoseph Jr, and A.A. Kudryavtsev, "Ionization kinetics and E-H mode transition in a noble gas, low-pressure pulsed ICP discharge", Plasma Sources Sci. Technol. **13** (2004), 600-603.

[28] E. Nasser, *Fundamentals of Gaseous Ionization and Plasma Electronics*, Wiley-Interscience: New York (1971).

[29] Y.R. Raizer, *Gas Discharge Physics*, Springer-Verlag: Berlin Heidelberg (1991).

[30] V.A. Lisovskiy, and V.D. Yegorenkov, "RF breakdown of low-pressure gas and a novel method for determination of electron drift velocities in gases", J. Phys. D: Appl. Phys. **31** (1998), 3349-3357.

[31] V.A. Lisovskiy, and V.D. Yegorenkov, "Low-pressure gas breakdown in combined fields", J. Phys. D: Appl. Phys. **27** (1994), 2340-2348.

[32] T. Kihara, "The mathematical theory of electrical discharges in gases", Rev. Mod. Phys. **24** (1952), 45-61.

[33] K. Burm, "Breakdown magnetic field in an inductively coupled plasma", Phys. Lett. A **372** (2008), 6280-6283

[34] K. Suzuki, K. Nakamura, H. Ohkubo and H. Sugai, "Power transfer efficiency and mode jump in an inductively RF discharge", Plasma Sources Sci. Technol. **7** (1998), 13-20.

[35] A. M. Daltrini, S. A. Moshkalev, T. J. Morgan, R. B. Piejak and W. G. Graham, "Plasma power measurement and hysteresis in the E-H Transition of a RF inductively coupled plasma system", Appl. Phys. Lett. **92** (2008), 061504.

[36] L.J. Mahoney, A.E. Wendt, E. Barrios, C.J. Richards, and J.L. Shohet, "Electron-density and energy distributions in a planar inductively coupled discharge", J. Appl. Phys. **76** (1994), 2041-2047.

[37] V.A. Godyak, R.B. Piejak, and B.M. Alexandrovich, "Measurements of electron energy distribution in low-pressure RF discharges", Plasma Sources Sci. Technol. **1** (1992), 36-58.

[38] L. Schott, "Electrical Probes" in Chapter 11, Plasma Diagnostics, ed. W. Lochte-Holtgreven, North-Holland Publ. Co., Amsterdam (1968).

[39] F.F. Chen, "Langmuir probe diagnostics", Lecture Notes from Mini-course on Plasma Diagnostics, IEEE-ICOPS meeting, Jeju, Korea, June 5, 2003.

[40] F.F. Chen, Introduction to Plasma Physics and Controlled FusionVol.1, 2nd ed., Plenum Press, New York, (1984), p.295.

[41] M.J. Druyvesteyn, "Der niedervoltbogen", Z. Phys., **64** (1930), 781-798.

[42] F. Magnus, and J.T. Gudmundsson, "Digital smoothing of the Langmuir probe I-V characteristic", Rev. Sci. Instrum. **79** (2008), 073503.

[43] R.L. Boylestad, *Introductory Circuit Analysis*, New Jersey: Prentice Hall (2003), pp.942-948.

[44] V.A. Godyak, R.B. Piejak, and B.M. Alexandrovich, “Electron energy distribution function measurements and plasma parameters in inductively coupled argon plasma”, Plasma Sources Sci. Technol. **11** (2002), 525-543.

[45] R.R.J. Gagné, and A. Cantin, “Investigation of an rf plasma with symmetrical and assymetrical electrostatic probes”, J. Appl. Phys., **43** (1972), 2639-2647; R.R.J. Gagne, and A. Cantin, “Pressure dependence of electron temperature using RF-floated electrostatic probes in RF plasmas”, Appl. Phys. Lett. **30** (1977), 316-319.

[46] F. Fujita, and H. Yamzaki, “Determination of electron energy distribution function of plasmas by digital processing from Langmuir probe characteristic”, Jpn. J. Appl. Phys., **29** (1990), 2139-2144.

[47] A. Savitzky, and M.J.E. Golay, “Smoothing and differentiation of data by simplified least squares procedures”, Analyt. Chem., **36** (1964), 1627-1639.

[48] S.C. Brown, *Basic Data of Plasma Physics*, MIT (1959), p.125

[49] R.B. Piejak, V.A. Godyak, and B.M. Alexandrovich, “A simple analysis of an inductive RF discharge”, Plasma Sources Sci. Technol. **1** (1992), 179-186.

[50] A. McCarter, R.N. Faulkner, A.R. Ellingboe, and M.M. Turner, “E to H transition in inductively coupled plasmas”, Contributed paper at the *XXVI International Conference on Phenomena in Ionized Gases* (ICPIG 2003), Greifswald, Germany, July 15-20, 2003.

[51] M.M. Turner, and M.A. Lieberman, “Hysteresis and the E-to-H transition in radiofrequency inductive discharges”, Plasma Sources Sci. Technol. **8** (1999), 313-324.

[52] R.B. Brode, “The quantitative study of the collisions of electrons with atoms”, Rev. Mod. Phys. **5** (1933), 257-279.

[53] C.M. Tsai, A.P. Lee, and C.S. Kou, “Characteristics of heating mode transitions in a radio-frequency inductively coupled plasma”, J. Phys. D: Appl. Phys. **39** (2006), 3821-3825

[54] A. Schwabedissen, E.C. Benck, and J.R. Roberts, “Comparison of electron density measurements in planar inductively coupled plasma by means of the plasma oscillation method and Langmuir probes”, Plasma Sources Sci. Technol. **7** (1998), 119-129.